# Preliminary Design Methods for the Thermal Management of Fuel Cell Powered Aeroengines

Master Thesis

Antonio Scoccimarro

Technische Universiteit Delft


TU Delft Delft University of Technology

Challenge the future

# Preliminary Design Methods for the Thermal Management of Fuel Cell Powered Aeroengines

Master Thesis

by

**Antonio Scoccimarro**

in partial fulfillment of the requirements for the degree of

**Master of Science**

in Aerospace Engineering

at the Delft University of Technology,

to be defended publicly on Monday April 17th 2023.

| | | |
|---|---|---|
| Student number: | 4538366 | |
| Supervisors: | Prof. dr. ir. P. Colonna | |
| | Dr. ir. C.M. de Servi | |
| Thesis committee: | Prof. dr. ir. P. Colonna, | TU Delft |
| | Prof. dr. ir. K. Hooman, | TU Delft |
| | Dr. ir. C.M. de Servi, | TU Delft |
| | Dr. ir. C. Falsetti, | TU Delft |

Cover Image Credits: De Havilland Aircraft of Canada Limited

An electronic version of this thesis is available at http://repository.tudelft.nl/.

TU Delft Delft University of Technology

# ACKNOWLEDGEMENTS

This thesis would have not been possible without the guidance of my supervisors, Piero and Carlo. With them I was able to explore what for me was a new discipline, thermal management, which I am sure will be a strong foundation for my future engineering career.

Secondly, I am grateful to the research group as a whole and the PhD candidates who dedicated their time in helping me out and supporting me.

The motivation to work on sustainable propulsion and my passion for fuel cell systems come from the Forze Hydrogen Racing Team, a team of wonderful students to which I owe most of my practical engineering experience. I wish them good luck for all future endeavours.

Also, I would like to thank my family. My parents, Elena and Carlo have always supported me and followed me closely in my endeavours and I am grateful for the opportunity they gave me to study in Delft. Then, my brother Enrico, who always knew how to support me through stressful times and to whom I look up as a role model for my future personal life and career.

Furthermore, I am grateful for the many friends I made during the last six years at TU Delft. I never would have imagined to find such a diverse and fun group of people with whom I share so much.

Finally, a special thanks goes to two special people, Sara and Levin, who were able to support me with affection and kindness. You bring joy and excitement into my life and I am glad to have you by my side.

*Antonio Scoccimarro*
*Delft, April 2023*

# SUMMARY

Hydrogen has been identified as an alternative to jet fuel to decarbonize the aviation sector. It can either be used as fuel for conventional gas turbine engines or converted into electric power by a fuel cell. Hydrogen turbines have been researched in the past with some demonstrators successfully completing flights but major European aircraft manufacturers do not expect them to enter into service before 2035. Proton exchange membrane fuel cells have benefited from the development carried on by the automotive industry and are already commercially available. Additionally, they have no harmful emissions by design, while hydrogen turbines suffer from NOx emissions. Being characterized by better energy and power densities than currently available batteries, they are now a research focus of new aircraft development.

Fuel cells operate at higher efficiencies with respect to turbine engines, but, especially in aviation, their thermal management is challenging and needs to be designed integrally to the propulsion system. PEM fuel cells need to operate at low temperatures, typically around 70 to 80°C, and the rejection of MW level low-grade heat has a significant impact on aircraft drag, weight and power requirements. Thus, methods to design efficient and low-drag thermal management systems are critical. Although simplified approaches for thermal management design of hybrid or electric aircraft have been already proposed, all are based on conventional single-phase liquid cooling while an extension to novel cooling concepts is missing.

Cooling fuel cells with phase-change techniques have attracted research efforts in recent years. One of the methods, flow boiling, has the potential of increasing thermal management system performance. It can be implemented in pumped multi-phase and vapour compression cycle architectures and it benefits from increased heat transfer coefficients in evaporation and condensation phases. Preliminary studies show that weight savings and increased heat rejection capacities are achievable with this novel technique, but detailed design methods for aircraft applications are lacking in the literature.

This research aims at developing preliminary design methods for thermal management systems of aviation-grade hydrogen fuel cell propulsion systems. Both conventional liquid cooling and novel cooling techniques using flow boiling are investigated.

The first method presented in this thesis is a preliminary system analysis procedure to aid the selection of cooling fluid . Furthermore, architectures of liquid and two-phase cooling systems are presented. The main components common to all architectures, like the fuel cell and main heat exchanger are modelled in detail using the 0D lumped parameter approach. As the intended application is aircraft propulsion systems, the methods to model cooling ducts, air inlets and outlets are included, as their impact on the drag characteristics of the aircraft is relevant.

A test case was devised to test the method , evaluate its validity and identify points of improvement. The De Havilland Dash-8 Q300 aircraft was selected as reference aircraft to ensure that realistic and relevant design constraints, like power requirements and installation space, are used.

A detailed analysis of the fuel cell cooling channels shows that flow boiling of methanol and R1233ZDE is a viable cooling solution. The former fluid presents higher heat transfer coefficients but suffers from a larger pressure drop. The latter has a lower heat transfer coefficient, and its prediction is more uncertain, highlighting the need for further experimental research in this area. Among the systems architectures tested, the pumped multi-phase architecture shows the most promising results with both weight and drag savings with respect to the conventional single-phase liquid cooling system. Vapour compression systems are less attractive as the high power demand of the compressor offsets the gains in drag reduction.

# Contents

# List of Figures

# List of Tables

# NOMENCLATURE

**Physical Constants**

| | | |
|---|---|---|
| $F$ | Faraday Constant | $96485.3321\,\mathrm{s\,A\,mol^{-1}}$ |
| $g$ | Gravitational Acceleration | $9.81\,\mathrm{m\,s^{-2}}$ |

**Symbols**

| | |
|---|---|
| $\bar{q}$ | Average Dynamic Pressure |
| $\beta$ | Wall Axial Conductivity Parameter |
| $\chi$ | Molar Ratio |
| $\Delta T_{\mathrm{Sat}}$ | Wall Superheat |
| $\Delta T_{\mathrm{Sub}}$ | Degree of Sub-cooling |
| $\delta^*$ | Boundary Layer Height |
| $\dot{m}$ | Mass Flow Rate |
| $\dot{Q}$ | Heat Transfer Rate |
| $\dot{V}$ | Volumetric Flow Rate |
| $\epsilon$ | Heat Exchanger Effectiveness |
| $\eta$ | Efficiency |
| $\gamma$ | Ratio of Specific Heats |
| $\Lambda$ | Aspect Ratio |
| $\lambda$ | Stoichiometry |
| $p$ | Partial Pressure |
| $\mu$ | Dynamic Viscosity |
| $\phi^2_{LO}$ | Two-Phase Multiplier |
| $\rho$ | Density |
| $\sigma$ | Surface Tension |
| $\varepsilon_0$ | Diffuser Effectiveness |
| $\varphi$ | Relative Humidity |
| $A$ | Area |
| $AR$ | Area Ratio of 2D Diffuser |
| $B$ | Blocked Area Fraction |
| $Bo$ | Boiling Number |
| $C$ | Heat Capacity Rate |
| $c$ | Specific Heat Capacity of Incompressible Liquid |
| $C_{\mathrm{D}}$ | Drag Coefficient |
| $C_{\mathrm{P}}$ | Pressure Recovery Coefficient |
| $c_p$ | Specific Heat Capacity at Constant Pressure |
| $C_r$ | Heat Capacity Rate Ratio |
| $Ca$ | Capillary Number |
| $Co$ | Convective Number |
| $D$ | Drag |
| $D_h$ | Hydraulic Diameter |
| $E$ | Effective Area Fraction |
| $E$ | Electromotive Force |
| $F$ | Force |
| $f$ | Fanning Friction Factor |
| $f_D$ | Darcy Friction Factor |
| $Fr$ | Froude Number |
| $G$ | Gibbs Free Energy |
| $G$ | Mass Flux |
| $g$ | Specific Gibbs Free Energy |
| $H$ | Enthalpy |
| $h$ | Fin Height |
| $h$ | Specific Enthalpy |
| $h_{\mathrm{c}}$ | Convective Heat Transfer Coefficient |
| $h_{\mathrm{TP}}$ | Two-Phase Boiling Heat Transfer Coefficient |
| $I$ | Current |
| $i$ | Current Density per Unit Area |
| $j$ | Colburn Factor |
| $K$ | Momentum Loss Factor |
| $k$ | Thermal Conductivity |
| $L/D$ | Lift to Drag Ratio |
| $L$ | Length |
| $l$ | Fin Length |
| $M$ | Figure of Merit for Fluid Selection |
| $M$ | Mach Number |
| $m$ | Mass |

| | |
|---|---|
| $N$ | Number of (Amount) |
| $Nu$ | Nusselt Number |
| $P''$ | Specific Power per Unit Area |
| $P$ | Power |
| $p$ | Pressure |
| $p_R$ | Reduced Pressure |
| $p_t$ | Total Pressure |
| $Pr$ | Prandtl Number |
| $Q$ | Thermal Energy |
| $q$ | Heat flux |
| $R$ | Specific Gas Constant |
| $r$ | Resistance per Unit Area |
| $r_{O2}$ | Molar Ratio of Oxygen in Air |
| $r_{s/c}$ | Storage to Converter Ratio |
| $Re$ | Reynolds Number |
| $S$ | Entropy |
| $s$ | Fin Pitch |
| $T$ | Temperature |
| $t$ | Thickness |
| $U$ | Maximum Air Velocity |
| $u$ | Local Air Velocity |
| $UA$ | Overall Heat Transfer Capacity |
| $V$ | Velocity |
| $V$ | Voltage |
| $W$ | Width |
| $W$ | Work |
| $We$ | Weber Number |
| $x_{vq}$ | Vapour Quality |
| $Z$ | Heat Exchanger Air Path Length / Core Thickness |

**Subscripts**

| | |
|---|---|
| act | Activation |
| cell | Single Cell |
| comp | Compressor |
| conc | Concentration |
| cond | Condenser |
| cool | Cooling |
| crit | Critical Point |
| e | Electrical |
| evap | Evaporator |
| f | Formation |
| fc | Fuel Cell |
| H2Oevap | Produced Liquid Water Evaporation |
| l | Liquid |
| lam | Laminar |
| lv | Latent (Liquid - Vapour) |
| ohm | Ohmic |
| op | Operational Single Cell Conditions |
| react | Reaction |
| ref | Reference |
| rq | Required |
| sat | Saturation Conditions |
| sys | System |
| tk | Tank |
| tot | Total |
| turb | Turbulent |
| v | Vapour |
| vs | Vapour Saturation Conditions |
| wall/s | Cooling Channel Wall/s |

**Abbreviations**

| | |
|---|---|
| APU | Auxiliary Power Unit |
| BOP | Balance of Plant |
| CHF | Critical Heat Flux |
| COP | Coefficient of Performance |
| DI | Dry-out Incipience |
| EGW | Ethyl-Glycol Water |
| EMF | Electromotive Force |
| FC | Fuel Cell |
| GDL | Gas Diffusion Layer |
| GWP | Global Warming Potential |
| HHV | Higher Heating Value |
| HX | Heat Exchanger |
| LH2 | Liquid Hydrogen |
| LHV | Lower Heating Value |
| LO | Liquid Only |
| LT | Low Temperature |

| | |
|---|---|
| MEA | Membrane Electrode Assembly |
| NTU | Number of Transfer Units |
| OCV | Open Circuit Voltage |
| ODP | Ozone Depletion Potential |
| ONB | Onset of Nucleate Boiling |
| PEM | Proton Exchange Membrane / Polymer Electrolyte Membrane |
| PMP | Pumped Multi Phase |
| PSP | Pumped Single-Phase |
| QBC | Thermal Boundary Condition |
| TP | Two-Phase |
| TRL | Technology Readiness Level |
| VCS | Vapour Compression System |

# 1

# INTRODUCTION

In recent years much research has been dedicated to reducing the climate impact of aviation. The main environmental impact of aviation is caused by the emissions of conventional kerosene-powered propulsion systems, be them turbines or piston engines. Already in 2011, the European Commission outlined the path of European aviation [1] and set a targeted reduction of 75% in $CO_2$ emissions and 90% $NO_x$ emissions. Reducing emissions is necessary to tackle the short-term impact of aviation but eliminating harmful emissions altogether can lead to a fully sustainable aviation sector that can continue its operation in the long term without burdening society.

For this reason, alternatives to kerosene propulsion systems have been researched throughout the years. Electric batteries and hydrogen have been identified as green and sustainable alternative energy carriers [2]. While batteries provide only electricity, to be used for example with electric motors and propellers or fans to produce propulsive power [3], hydrogen can both provide thermal energy, when burned in a turbine engine, as well as electricity if oxidized in a fuel cell[4]. Hydrogen has a higher mass-energy density compared to kerosene and batteries but suffers from a lower volumetric energy density than fossil fuels [5].

Hydrogen turbines have been researched in the past with some demonstrators successfully completing flights. Major European aircraft manufacturers expect them to enter into service later than 2035 [6]. Fuel cells have benefited from the development carried on by the automotive industry and are already commercially available. Additionally, they have no harmful emissions by design, while hydrogen turbines suffer from NOx emissions. Presenting better energy and power densities than currently available batteries they are now a research focus of new aircraft development.

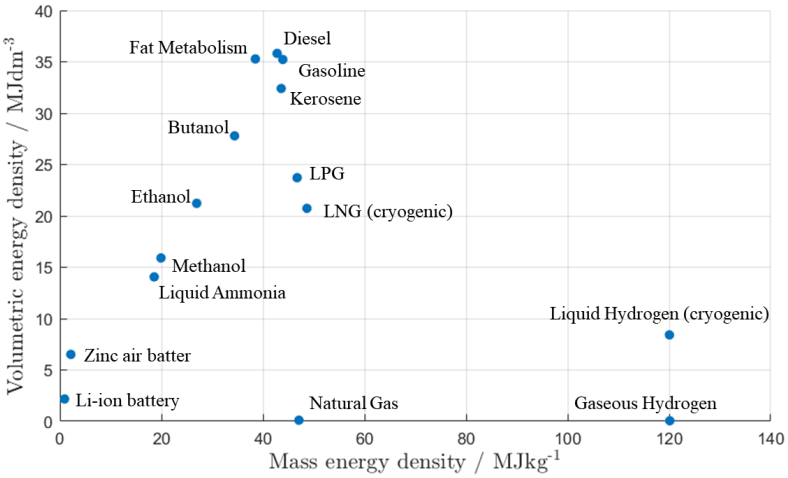


Figure 1.1: Hydrogen mass and volumetric energy density compare to other energy storage technologies and fuels. Reproduced from Ref. [5].

Fuel cells have been used and studied for many years with NASA being the first to pioneer fuel cells in the aerospace sector when they were used as an electrical power source in the space shuttle[1]. Of the many types of fuel cells that exist, low temperature proton exchanged membranes are most used in the automotive sector to power cars and trucks [7]. They are, at the moment, the most researched type for aircraft applications. Other fuel cell types, like solid oxide FCs and alkaline FCs, have a lower technology readiness level as they are less attractive for mobile applications and did not benefit from extensive funding. SOFCs have been studied for aerospace applications as well [8, 9], and provide some advantages in contamination resistance and fuel flexibility. However, the high operating temperatures and structural limitations have attracted less interest from the aerospace industry. A fuel cell system for vehicle application is shown in Figure 1.2 while a PEM fuel cell stack from ElringKlinger[2] for automotive application is shown in Figure 1.3. A prototype PEM fuel cell powered aeroengine flown in 2023 by Universal Hydrogen[3] is portrayed in Figure 1.4. The most distinguishable feature with respect to conventional turbine-powered aeroengines is the ram air cooling duct mounted on the side of the nacelle.

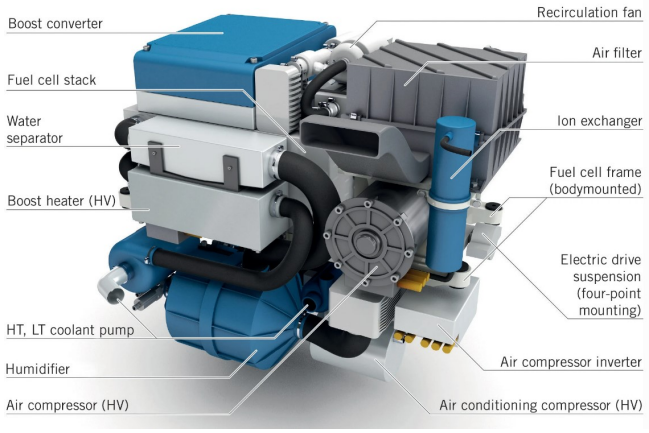


Figure 1.2: Integrated fuel cell system for vehicle application. Reproduced from Ref. [10].

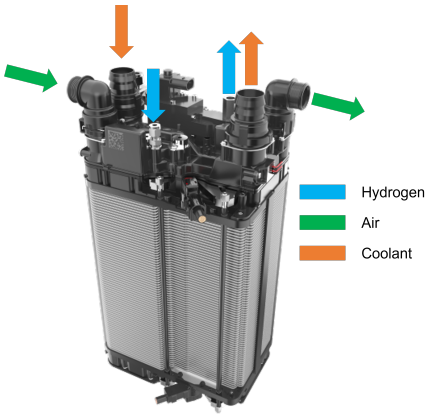


Figure 1.3: PEM Fuel Cell Stack with media interface. Credit: ElringKlinger

Fuel cells operating with pure hydrogen are mostly used in applications where harmful emissions are to be avoided while other fuels like methanol,natural gas and other hydrocarbons, can also be used with a reformer process. Oxygen is used as an oxidizer in the electrochemical reaction, either directly or carried by ambient air. The second option is preferred in most applications as the oxidizer storage and supply system is eliminated. Fuel cells operate at efficiencies that are normally around 50% and their characteristic is that the efficiency decreases with output power, resulting in the characteristic efficiency and power curves shown in Figure 1.5. For a given fuel cell size, increasing the current delivered reduces the voltage up to a point where the output power does not increase anymore. The operating range between the point of maximum power and the point of maximum efficiency has a linear efficiency profile. Successful sizing of fuel cell propulsion systems for aircraft application lies in finding a trade-off between power density, to minimize propulsion system weight, and efficiency, to minimize fuel burn and storage system weight [11, 12]. The optimal design point for fuel cell systems lies in the linear part of the efficiency curve, not at the peak power point. Oversizing the fuel cell is often advantageous to minimize fuel burn[13].

Despite the higher efficiency with respect to turbine or internal combustion engines, the thermal management of fuel cells, especially in aviation, is challenging and needs to be designed integrally to the propulsion system [15, 16]. PEM fuel cells need to operate at low temperatures, typically around 70 to 80°C [17], and the rejection of low-grade heat can add drag to the aircraft up to 27% [15]. Thus, methods to design efficient and low-drag thermal management systems are critical. Although simplified approaches for thermal management design of hybrid or electric aircraft have been already proposed [15, 16, 18, 19], all are based on conventional single-phase liquid cooling and an extension to novel cooling concepts is missing.

Various cooling strategies for fuel cells exist and are discussed extensively in literature [20, 21]. An overview

[1] https://www.nasa.gov/topics/technology/hydrogen/fc_shuttle.html
[2] https://www.elringklinger.de/en
[3] https://hydrogen.aero/


Figure 1.4: Prototype of fuel cell powered aeroengine. Cooling ram air ducts clearly visible. Credit: Universal Hydrogen.

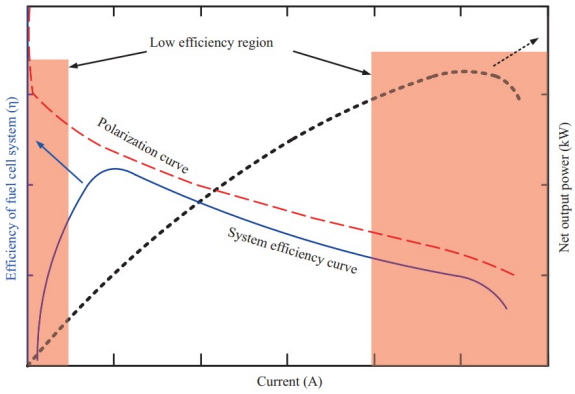


Figure 1.5: Typical Fuel Cell System Efficiency and Power Output. Reproduced from Ref. [14].

of the cooling options with their respective application to systems based on power level can be seen in Figure 1.6. Air and passive cooling are suitable for applications that require little power while liquid and phase change cooling is identified as the only solution for power levels above 10 kW. While liquid cooling is already being used extensively in all commercial applications, like in the automotive industry [7, 22, 23], phase-change cooling is still in development. Research on evaporative [24] and flow boiling [25] systems has shown promising benefits in both weight and heat rejection capacity. Numerical [26] and experimental [27–29] studies of flow boiling applied to fuel cell cooling highlight the potential of using this technique and a link to system-level design methods is needed.

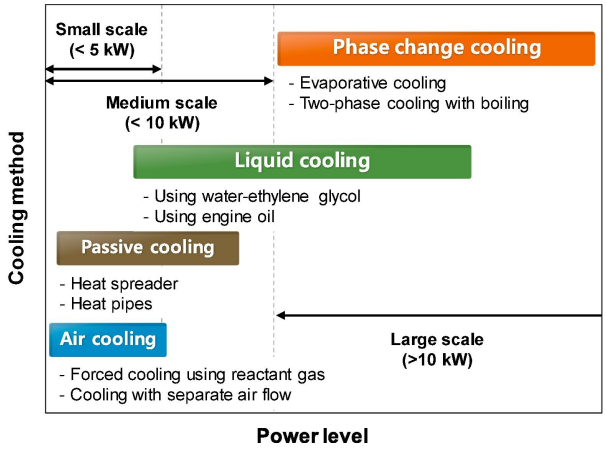


Figure 1.6: Caption [29]

## 1.1. RESEARCH QUESTIONS AND OBJECTIVES

This research aims at developing preliminary design methods for thermal management systems of aviation-grade hydrogen fuel cells. The impact of thermal management systems of fuel cells on the overall aircraft performance in terms of power, weight, and drag is significant and a detailed approach to the design of such systems is lacking in the literature. The focus of the present work is on both conventional liquid cooling and novel cooling techniques using flow boiling. The application of the design methods developed in this work is the aircraft propulsion system. Thus, integration aspects in aeroplanes are included. The high-level research questions are:

What methods can be used to design and simulate the thermal management system of hydrogen fuel cell propulsion systems for aircraft applications?

Which parameters are driving the design of thermal management systems using both single and two-phase cooling solutions?

Additional sub-questions shall be answered as well:

- "Can a fuel cell be cooled effectively with the flow boiling technique?"
- "Can flow boiling be modelled accurately enough for system-level design purposes?"
- "What fluids are suitable to cool a fuel cell using flow boiling techniques?"
- "Which novel thermal management system architectures can be employed and how does their performance compare to the liquid cooling benchmark?"
- "How can ram air be used effectively as the heat sink of a fuel cell thermal management systems?"
- "Which parameters drive the design of a ram air cooling duct?"

Given these research questions, the following methods were developed. First, a method to evaluate and select potential fluids for fuel cell cooling applications was devised. The method includes preliminary system analysis to evaluate the fluid-system matching in terms of relevant performance parameters. Furthermore, architectures of liquid and two-phase cooling systems were researched and promising ones were selected to be further studied. The main components common to all architectures, like the fuel cell and main heat exchanger were then modelled in detail to the extent that is needed to include all physical phenomena relevant to the design of the thermal management system. As the intended application is aircraft propulsion systems, the methods to model cooling ducts, air inlets and outlets are included, as their impact on the drag characteristics of the aircraft is relevant. The performance indicators that can be used to evaluate and compare different solutions were also defined.

Furthermore, a test case was devised to test the method, evaluate its validity and identify points of improvement. The De Havilland Dash-8 Q300 aircraft was selected to ensure that realistic and relevant design constraints, like power requirements and installation space, can be defined. This aircraft is currently subject to multiple research[4] and prototyping[5] efforts as this older variant is cheap, has a large nacelle in which to integrate systems, and has a lower power requirement than other regional turboprop aircraft making it a more attractive stepping stone for fuel cell powered aero-engines. Take-off conditions, which represent the most limiting operating point for fuel cell cooling in terms of thermal energy rejection requirements and limited available ram air speed, were used to design and simulate various cooling configurations. For each configuration, a range of design variables was used to span a potential design space. This allowed identifying the driving parameters for an effective thermal management system. Finally, the shortcomings of the methods presented, including the critical areas in which more research is needed, were identified.

[4] https://www.zeroavia.com/de-havilland
[5] https://www.businesswire.com/news/home/20230302005768/en/

# 2

# LITERATURE STUDY

## 2.1. RECENT HYDROGEN FUEL CELL POWERED AIRCRAFT PROJECTS

Many companies and research centres are currently looking at developing hydrogen fuel cell propulsion systems for short-haul aircraft and many plan to experiment with demonstrators in the next 5 years. The Politecnico of Turin University was the first to demonstrate a flying prototype of a small ultralight aircraft powered by fuel cells [30]. Airbus has plans to develop hydrogen-powered aircraft by 2035 and their collaboration with German fuel cell manufacturer ElringKlinger [31] on fuel cell research points to the fact that they are also considering this technology for either propulsion or onboard power production for auxiliary systems. MTU Aero Engines and DLR (German Aerospace Center) have entered a partnership to develop a small regional plane demonstrator powered by fuel cells by 2025[32]. Finally, H2Fly has already developed a small 4-seater fuel cell-powered aircraft that has successfully flown many test campaigns and is currently developing a 40 seats regional aircraft [33].


Figure 2.1: HY4 test airplane during testing in Stuttgart (Sourece: H2Fly) [33].

The fuel cell-powered aircraft presented all share similar characteristics. Mainly low temperature proton exchange membrane (LT-PEM) fuel cells are considered and many opt for a liquid hydrogen storage tank as it provides better gravimetric energy density than gaseous hydrogen storage [2]. The electric power generated by the oxidation of hydrogen in the fuel cell is used to power electric motors which turn propellers and generate thrust. The liquid hydrogen fuel tanks are pressurized and cannot be shaped freely (like a conventional kerosene tank which resides within the wing) without significant weight penalties and are thus positioned in the fuselage or externally attached to the wings [34]. The fuel cell and its auxiliary components, also called the balance of plant (BOP), are positioned in the nacelles, in the fuselage or split between both. The power

density of fuel cell systems is also lower than turbine engines, typically in the order of $1\,\mathrm{kW\,kg^{-1}}$ vs $10\,\mathrm{kW\,kg^{-1}}$ respectively [13] which implies a higher installation mass and volume. To understand the challenges that fuel cell systems bring to the integration in regional planes a more thorough understanding of their operation is needed and is addressed in the next section.

## 2.2. PEM FUEL CELLS: HOW DO THEY WORK?

The fundamentals of hydrogen fuel cells and their operation are extensively explained in many books and articles. In this section, the most important aspects of their workings are presented. Most of the information shown is from two books: "Fuel Cell Systems Explained" by Larminie and Dicks [23] and "Pem Fuel Cells: Theory and Practice" by Barbir [22]; covering all the aspects of fuel cells, and in particular LT-PEM fuel cells, needed to lay the foundation for researching the application of this technology in the aviation sector.

### 2.2.1. ELECTROCHEMICAL REACTION AND THEORETICAL EFFICIENCY

The power generated by a fuel cell comes from the electrochemical reaction that happens when hydrogen is oxidized. The overall reaction can simply be described by Equation 2.1 where 2 hydrogen molecules get oxidized by an oxygen molecule to form water, as in

$$2H_2 + O_2 \rightarrow 2H_2O. \tag{2.1}$$

More in detail this reaction happens in two steps. The first one, the anodic reaction, happens when the hydrogen molecules are split into hydrogen ions, effectively protons, and electrons as in

$$2H_2 \rightarrow 4H^+ + 4e^-. \tag{2.2}$$

The second part of the reaction is the cathodic reaction,

$$O_2 + 4e^- + 4H^+ \rightarrow 2H_2O, \tag{2.3}$$

involves the recombination of the protons with the electrons and oxygen molecule to form water.

In order to convert useful electrical power and not just thermal power the two reaction steps are kept separate by an electrolytic membrane that only lets protons through. The electrons, in order to participate in the whole reaction, are collected by a conductive medium at the anode and passed through an electrical circuit where they can do useful electrical work and rejoin at the cathode to complete the reaction.

As entropy is always generated in energy conversion steps, not all the energy released by the formation of water can be converted into electrical energy. The theoretical maximum efficiency of a hydrogen fuel cell is limited by the Gibbs free energy

$$\Delta G = \Delta H - T\Delta S, \tag{2.4}$$

which is the difference between the enthalpy of formation and the entropy generated by the reaction. The Gibbs free energy difference is equivalent to the maximum electrical work done by the reaction and is defined, on the basis of a mole of hydrogen, as

$$\Delta \bar{g}_f = \left(\bar{g}_f\right)_{H_2O} - \left(\bar{g}_f\right)_{H_2} - \frac{1}{2}\left(\bar{g}_f\right)_{O_2}. \tag{2.5}$$

As the Gibbs free energy of formation of water changes at different temperatures, the maximum electrical work possible varies according to Table 2.1.

The enthalpy of formation of liquid water is always $\Delta \bar{h}_f = -285.84\,\mathrm{kJ\,mol^{-1}}$, also known as the higher heating value (HHV) of hydrogen, and the ratio of Gibbs free energy to enthalpy of formation can be used to define the theoretical thermodynamic efficiency of the fuel cell. In combustion engines, the lower heating value is

| Form of water product | Reaction Temperature [°C] | $\Delta\bar{g}_f$ [kJ mol$^{-1}$] | Max EMF [V] | Max Efficiency [%] |
|---|---|---|---|---|
| Liquid | 25 | -237.2 | 1.23 | 83 |
| Liquid | 80 | -228.2 | 1.18 | 80 |
| Gas | 80 | -226.1 | 1.17 | 79 |
| Gas | 100 | -225.2 | 1.17 | 79 |
| Gas | 200 | -220.4 | 1.14 | 77 |
| Gas | 400 | -210.3 | 1.09 | 74 |
| Gas | 600 | -199.6 | 1.04 | 70 |
| Gas | 800 | -188.6 | 0.98 | 66 |
| Gas | 1000 | -177.4 | 0.92 | 62 |

Table 2.1: Gibbs free energy of formation for the reaction of hydrogen with oxygen [23] at different reaction temperatures and relative maximum obtainable electromotive force and reaction efficiency.

often used, as it is assumed that all the water formed is in the gaseous state. As LT-PEM often operate below 100°C this assumption can lead to energy accounting mistakes and the higher heating value is preferred.

Related to efficiency is also the concept of open-circuit voltage (OCV). This is a measure of the electromotive force that a fuel cell would have in ideal conditions and is often used also to define the efficiency of a fuel cell, as it is readily measurable. The electrical work is related to the Gibbs free energy of formation and can thus be expressed as

$$W_e = -2FE \quad [\mathrm{J}], \tag{2.6}$$

where 2 is the number of electrons released by a molecule of hydrogen when reacting and F is the Faraday constant expressing the charge carried by a mole of electrons (96485.3321 C mol$^{-1}$) and E is the electromotive force. Rearranging Equation 2.6 and introducing the Gibbs free energy, one can define the electromotive force as

$$E = \frac{-\Delta\bar{g}_f}{2F}. \tag{2.7}$$

For a 100% efficient fuel cell the Gibbs free energy equals the formation enthalpy of liquid water and the equivalent reference voltage $V_{ref}$ becomes 1.48 V. At standard operating conditions, including conversion losses, the OCV is 1.23 V. The thermodynamic efficiency of a fuel cell under operation can be easily defined as

$$\eta = \frac{V_{cell}}{V_{ref}}, \tag{2.8}$$

where $V_{cell}$ is the operating voltage of a single cell. In standard conditions at an OCV of 1.23V the efficiency would be 83.1%.

Another factor affecting the Gibbs free energy, and thus the OCV, is the pressure and concentration of the reactants. The Nernst equation

$$E = E^0 + \frac{RT}{2F}\ln\left(\frac{p_{H_2}\cdot p_{O_2}^{\frac{1}{2}}}{p_{H_2O}}\right) \tag{2.9}$$

expresses the change in OCV due to changes in partial pressures $p$ of the reactants and products and is valid if the pressure is given in bar and the produced water is gaseous. $E^0$ is the EMF at standard conditions. It is clear that an increase in performance can be achieved when the cell is operated with pressurized reactants.

While in this section an overview of the theoretical fuel cell efficiency and voltages is given the operational voltages can vary significantly from the theoretical ones. This deviation due to irreversibilities is further addressed in subsection 2.2.3.

The importance of efficiency in any energy conversion process is readily apparent when the energy source is finite and needs to be used effectively. Additionally, the amount of energy that cannot be converted to electrical work remains as thermal energy. The thermal energy released in the reaction is often transferred to the sensible enthalpy of the reactants and products, which increase in temperature, and to the latent enthalpy

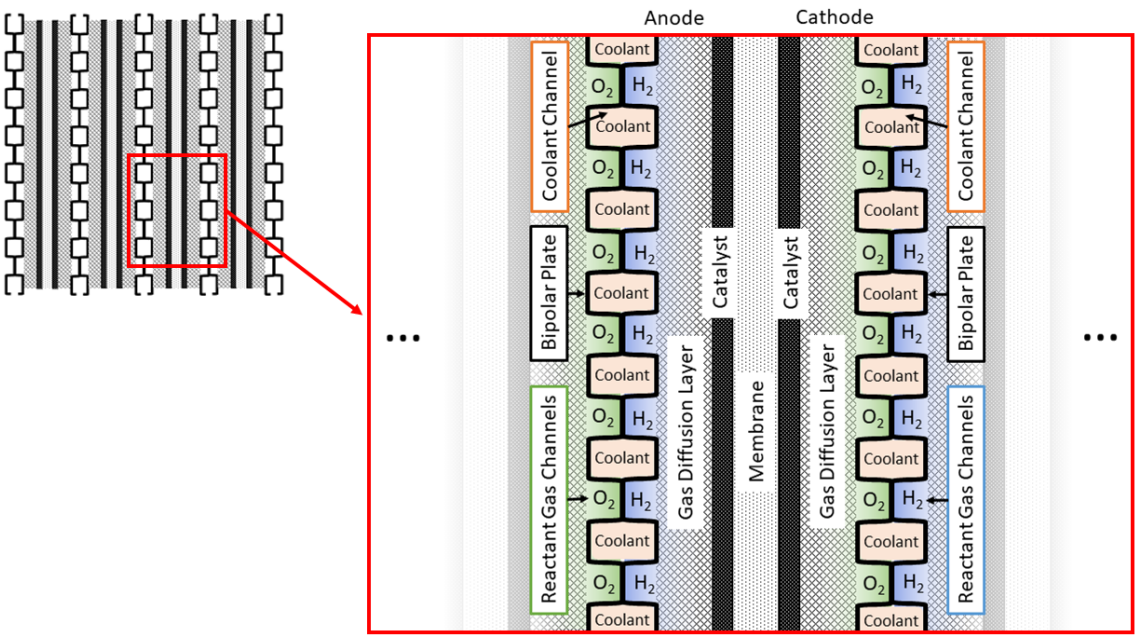


Figure 2.2: Membrane electorde assembly schematic with bipolar plates. (Not to scale)

of the produced water which evaporates. Additionally, the thermal energy is stored in the materials of the cell and transferred to ambient air through convection and radiation. In most modern high-power fuel cell applications the released thermal energy due to inefficiencies can be such that it would quickly lead to high, hazardous operating temperatures and material failure if a strategy to remove the thermal energy effectively is not employed. These strategies will be addressed in section 2.3.

### 2.2.2. MEMBRANE ELECTRODE ASSEMBLY

In order to achieve the functionality needed to separate the anodic and cathodic reactions, a special type of assembly is used called membrane electrode assembly (MEA). This assembly is constructed with multiple layers forming a flat shape that maximizes the surface area available for the reaction to take place. For this reason, the reaction can be described as happening along a specific spatial direction which is normal to the MEA surface. A cross-section of such an MEA is shown in Figure 2.2. In the illustration, two conductive plates are also added, called bipolar plates, to represent the full cell as used in a fuel cell stack. The representation of the stack, where a single MEA with bipolar plates is repeated in series is also schematically represented in the picture. Starting from the anode side the hydrogen gas is guided over the MEA by reactant gas channels machined or stamped in the conductive plate. It is further distributed by a gas diffusion layer (GDL) which is essentially a conductive fine mesh. The hydrogen then encounters a layer of catalyst, most often platinum, that helps the hydrogen molecules to split into protons and electrons. The protons then pass through the membrane which is, in the case of PEM fuel cells the membrane is made of a polymer with an acidic ionomer that gives it the property of attracting protons and repelling electrons.

For this reason, PEM fuel cells are also sometimes called polymer electrolyte membrane fuel cells. While the protons pass the membrane the electrons are conducted back through the GDL into the conductive plate and passed through an electrical circuit and an electrical load. They rejoin the reaction at the cathode passing through the conductive plate at the oxygen side. On this side, the oxygen follows a similar path to the hydrogen where it is guided and distributed over the MEA to react with the protons and electrons in presence of a catalyst to form water. The reactants are mostly fed to the anode and cathode in excess of what the reaction needs to ensure good distribution over the whole membrane. The excess reactants that flow through and leave the cell can then partly evaporate and partly mechanically remove the formed water. The exhaust of the cell is then mostly water vapour.

The achievable current density of a single cell is in the order of $1 A/cm^2$ such that the surface power den-

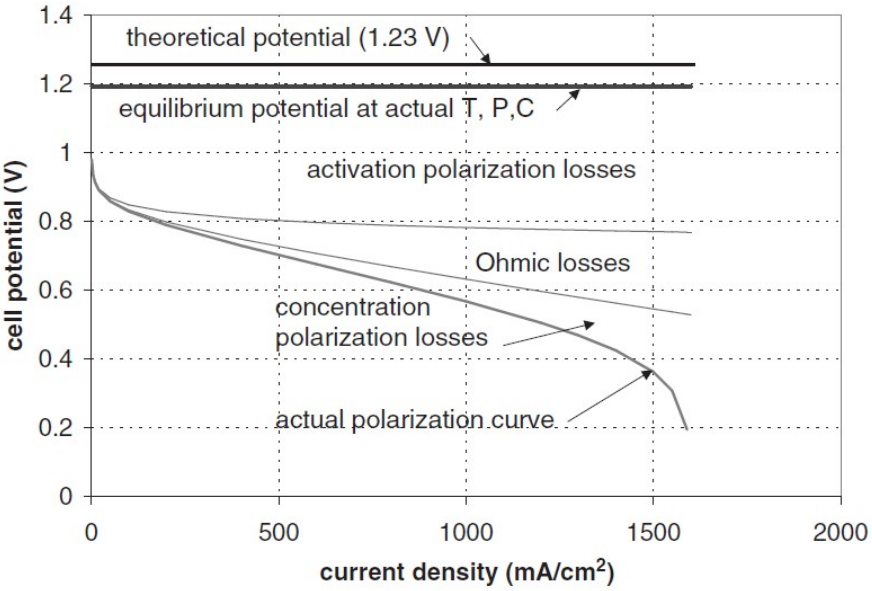


Figure 2.3: Example of voltage losses and resulting polarization curve for a PEM fuel cell. Reproduced from Ref. [22].

sity at an operational voltage of $0.6V$ is in the order of $0.6W/cm^2$. If a system in the order of $1MW$ is targeted an impossibly large surface would be required with a very low voltage and extremely high currents that would generate extreme ohmic losses and would render such an electrical power system useless. To overcome this limit single cells are almost always combined in cell stacks. In such a stack cells are connected in series such that electrons move from the anode of one cell to the cathode of the adjacent cell. In this way, the total voltage of the stack is the sum of the operational voltages of each individual cell, or, if the cell voltages are assumed to be equal in all cells the multiplication of $V_{\text{cell}}$ with the number of cells.

In this way, high voltages of over 500V can be achieved while the current is kept low. High voltages have their own drawbacks when it comes to the safety of implementation but they allow for higher electrical efficiencies in power systems and are thus more attractive in mobile and stationary power applications. The cells are connected in a stack through the conductive plates at the anode and cathode. These plates are often combined in a single plate that has hydrogen and oxygen/air channels on the two faces. It is then called a bipolar plate as it combines the anode of one cell with the cathode of the adjacent cell. Apart from connecting two cells electrically, coolant channels are often machined within the thickness of the plate allowing for dedicated coolant channels. This is especially useful when high power density stacks are considered where other types of cooling are less effective. Often the bipolar plates are composed of two stamped sheet metal plates welded together where the cooling channels are the negative space left by the gas channels on the two faces of the bipolar plate.

### 2.2.3. PERFORMANCE AND OPERATIONAL EFFICIENCY

As mentioned in subsection 2.2.1 the actual operational voltages of a fuel cell differ significantly from the theoretical ones and four main mechanisms exist that cause this difference. The typical relation between current density and voltage is given in Figure 2.3 and is often called the polarization curve.

#### IRREVERSIBILITIES AND VOLTAGE LOSSES

The first form of irreversibility that occurs in a fuel cell is related to the rate of reaction at the electrode surface and is called "activation loss". If a reaction happens at a fast rate, for example, due to high electrode roughness and good catalyst performance, the overvoltage needed to transfer electrons to and from the electrode is small. In this case, the overvoltage is opposing the reaction voltage creating a voltage drop. This type of loss follows the functional form

$$\Delta V_{\text{act}} = A \ln\left(\frac{i}{i_0}\right) \tag{2.10}$$

called Tafel equation. The constant $A$ is large for a slow reaction while the constant $i_0$, the exchange current density, is large for a fast reaction. The Tafel equation only works for $i > i_0$ and influences the polarization curve, especially at low current densities generating the initial rapid voltage loss.

The exchange current density is equivalent to the rate of reaction at equilibrium. Indeed even when no current is effectively flowing through the circuit the reaction is still happening with the reverse reaction occurring at the same rate as the forward reaction. This situation can be expressed with the equilibrium

$$O_2 + 4e^- + 4H^+ \leftrightarrow 2H_2O. \tag{2.11}$$

The parameters influencing $i_0$ are mainly temperature, surface roughness, and catalytic material. It can change by several orders of magnitude in different conditions. In PEM fuel cells the exchange current density is limited by the cathode and is several orders of magnitude smaller than the anode which can be neglected.

The second form of irreversibility is due to fuel leakage and electron conduction through the electrolyte. Although these effects are small, it is always possible that diffusion of hydrogen molecules through the membrane takes place and that some electrons manage to short-circuit the cell (leakage current). The crossing of a hydrogen molecule to the cathode is equivalent to two electrons leaking to the cathode and thus the effect of both modes can be regarded as one. For the sake of simplicity, both are captured in the parameter $i_n$: the internal leakage current. When an internal current is present, which is mostly the case and is usually in the order of a few $mA/cm^2$, then the drop in OCV follows the same form of the activation overvoltage as the current density of the cells is effectively higher than the exchange current density thus the combined effect of the first two irreversibilities can be expressed as

$$V = E - A \ln\left(\frac{i + i_n}{i_0}\right). \tag{2.12}$$

The third irreversibility is the most significant one and is influenced greatly by the operating conditions of the fuel cell rather than design, manufacturing and material choices. It is due to ohmic losses and is the effect of the combined resistance of the electrons passing through the conductive parts of the cell as well as the resistance encountered by the protons when passing through the membrane, also called ionic resistance. This effect is linear with current density and can be easily expressed with Equation 2.13 where $r$ represents the area-specific resistance.

$$\Delta V_{\text{ohm}} = i \cdot r \tag{2.13}$$

The part of area-specific resistance related to the electrical resistance of the electron flow can only be influenced by material choice and bipolar plate design and often it is small compared to the ionic resistance of the membrane. To lower the ionic resistance the membrane needs to be as conductive as possible and as thin as the mechanical and manufacturing limits allow. In the case of PEM fuel cells, the membrane conductivity is heavily influenced by the water content of the membrane. In fact, the membrane is formed by a hydrophobic fluorinated polymer base with (as in the case of Nafion®) sulfonated side chains. These side chains are $SO_3^-$ ions that are highly hydrophilic and create a dilute acid when in contact with water. Protons can then move freely through these hydrated portions of the membrane. The conduction behaves almost linearly with water content.

The fourth form of irreversibility is due to concentration losses. These happen when the current density is high and thus the high rate of reaction effectively depletes the air at the cathode of oxygen reducing its partial pressure locally. Similarly, this can happen at the anode when a high hydrogen mass flow generates a considerable pressure drop through the gas channels. This form of loss can not be described well analytically and an empirical form with constants to be fitted to experiments is proposed (Equation 2.14).

$$\Delta V_{\text{conc}} = m\exp(ni) \tag{2.14}$$

With $m$ and $n$ typically in the range of $3\times10^{-5}V$ and $8\times10^{-3}cm^2/mA$. The combination of all the mentioned losses gives form to Equation 2.15. This equation forms the basis of fuel cell performance modelling and can be complete with models or experimental data for the constants involved.

$$\begin{aligned} V &= E - \Delta V_{\text{ohm}} - \Delta V_{\text{act}} - \Delta V_{\text{trans}} \\ V &= E - ir - A\ln\left(\frac{i+i_n}{i_0}\right) + m\exp(ni) \end{aligned} \tag{2.15}$$

### OPERATIONAL CONDITIONS

The operational conditions of PEM fuel cells have an impact on the different loss terms presented above and a careful evaluation of the operating temperature, pressure and humidity of the reactants needs to be made in order to operate a fuel cell efficiently.

First of all the humidity of the reactants can have a large effect on performance. Higher reactant humidity is beneficial for fuel cell performance as it helps keep the membrane hydrated and thus increases the ionic conductivity of the membrane itself. Cathode humidity has a larger effect than anode humidity[17]. This is reflected in many systems having a cathode air humidifier but not a hydrogen one. Further use of recirculation techniques of unused hydrogen also introduces water in the anode and reduces further the need for hydrogen humidification [35]. The combination of high temperature and high relative humidity of cathode air makes humidification requirements challenging and much research is dedicated to the topic [36].

Secondly, reactant and operational temperatures need to be considered. Higher temperatures increase membrane conductivity, activation losses and increase diffusivity which leads to higher performances. If gasses are fed too cold then condensation of produced water in the catalytic layer might occur and the cell loses performance due to oxygen and hydrogen starvation. If cell operating temperatures are too high then water might evaporate from the membrane at a higher rate than it is produced drying out the membrane and reducing conductivity. Ozen *et al.* [17] found experimentally and by comparing his findings with previous literature, that an optimal range exists between $75°C$ and $85°C$. In general, the effect of operating at higher temperatures to improve membrane conductivity far outweighs the negative effect on OCV due to a decrease in available Gibbs free energy.

Finally, the effect of pressure has been found to improve performance in general with diminishing returns at higher pressures due to the logarithmic nature of the effect [37]. In addition to the increased reactant partial pressure, operating a fuel cell at pressures higher than ambient also improves the humidification requirements as the saturation partial pressure of water vapour in air can be achieved with less water. This can be shown with Equation 2.16 to Equation 2.19 [23, ch. 5]. The relationship between the molar ratio of vapour (v) to gas (g) and the partial pressures is

$$\chi = \frac{p_{\text{v}}}{p_{\text{g}}} = \frac{p_{\text{v}}}{p - p_{\text{v}}}, \tag{2.16}$$

where $p$ is the total pressure of the gas mixture. The relative humidity is defined as the ratio of the vapour partial pressure to the saturation partial pressure of the vapour as in

$$\varphi = \frac{p_{\text{v}}}{p_{\text{vs}}}. \tag{2.17}$$

For water, the saturation pressure is purely a function of temperature

$$p_{\text{vs}} = f(T). \tag{2.18}$$

Combining the above in

$$\chi = \frac{\varphi p_{\text{vs}}}{p - \varphi p_{\text{vs}}} \tag{2.19}$$

gives the expression for the molar ratio of water vapour in air given a specified relative humidity and saturation partial pressure (thus a specified temperature). As can be seen, if the total pressure is higher, the molar ratio becomes smaller thus less water is needed to humidify the same amount of air.

It has also been found by Lu *et al.* [37] that at really low pressures the effect of pressure drop in the cathode channels is more prominent than the water production thus humidity actually decreases giving rise to lower efficiencies. Most importantly when operating air-hydrogen fuel cells the pressurization of the air is done by mechanical means with a blower or compressor and the benefits of a higher pressure need to be balanced with the added power consumption of the compressor which makes the choice of an adequate and optimal working pressure only possible when the whole system is taken into account.

### 2.2.4. SYSTEMS AND AUXILIARY COMPONENTS

In this work, only air-fed systems are considered as they are the industry standard in mobile applications where carrying a separate storage system for oxygen is unfeasible. Such a system can be subdivided into three subsystems: air supply, hydrogen supply and cooling system. Many different strategies can be adopted to meet the requirements of each sub-system but only a selected few will be touched upon here and an example of them combined in a full system is schematically represented in Figure 2.4. For a more thorough presentation of possible strategies, the reader can refer to the book "PEM Fuel Cells: Theory and Practice" by Barbir [22] on which this section is based on.

#### AIR SUPPLY

Supplying air to a fuel cell system can be performed with a fan when operating at ambient pressure. Operating a pressurized system can have positive and to compress the air usually a compressor is used and often a centrifugal compressor is chosen. The compressor is usually driven by an electric motor using the same electric power generated by the fuel cell. This leads to an inherent optimization that needs to be performed on the compression ratio as a balance between fuel cell efficiency and compressor power needs to be found. Above a compression ratio of 1.5 the compressor power might consume a significant amount of generated power and diminishing returns are encountered when increasing the pressure ratio further [22, ch. 9].

The compression process can be considered adiabatic and high temperatures might be reached at the compressor outlet. An intercooler might be introduced in the air supply line to manage the air supply temperature. Before the air can enter the fuel cell stack it needs to be properly humidified. This can be done in different ways but two main strategies exist. The first strategy, which is shown in Figure 2.4, is to employ a passive air-to-air membrane humidifier. This type of humidifier lets the wet stream at the outlet of the fuel cell pass over a membrane that separates it from the dry stream at the inlet. Water exchange between the two streams happens across the membrane and the produced water in the stack can be effectively reused to humidify the incoming air. Another strategy requires separating liquid water from the exhaust of the system after the exhaust gasses have passed a condenser. Liquid water is then introduced again through a spray nozzle in the air stream in front of the fuel cell stack. As the latent heat of evaporation of water is high the temperature of the air stream can drop significantly below its target of $80°C$ and a heat exchanger (instead of an intercooler) heating up the air stream and enhancing water evaporation might be needed.

After the stack outlet, a pressure regulating valve can be employed to control the back pressure of the stack and keep it within operating conditions. Excess water can be then separated from the stream to be used for humidification purposes or to protect a turbine from water erosion. Such a turbine can recuperate part of the stream energy and be coupled to the compressor to increase system performance.

#### HYDROGEN SUPPLY

Hydrogen can be stored and supplied in different ways but most commonly, in the case of mobile power applications, it is stored under pressure in tanks and delivered to the fuel cell with a blow-down system. The pressure in the stack is regulated through a pressure regulator. To decrease mass transport losses in the fuel cell stack usually, a higher amount of hydrogen is fed than what would be needed for stoichiometric conditions. The excess hydrogen is then recirculated to keep fuel utilization high. This recirculation can be achieved through a recirculation blower or an ejector. An ejector utilizes a high-pressure stream of hydrogen from the main tank to entrain the low-pressure exhaust from the stack outlet. Recirculating hydrogen has the added advantage that no humidification of the hydrogen is needed as water vapour present in the anode and exhausted from the stack is recirculated to the inlet. The problem with such a closed-loop system is that impurities in the fuel, liquid water from the reaction and nitrogen that crosses over from cathode to anode accumulate in the anode loop. To remove these impurities regular purging of the anode is needed [22, ch. 9].

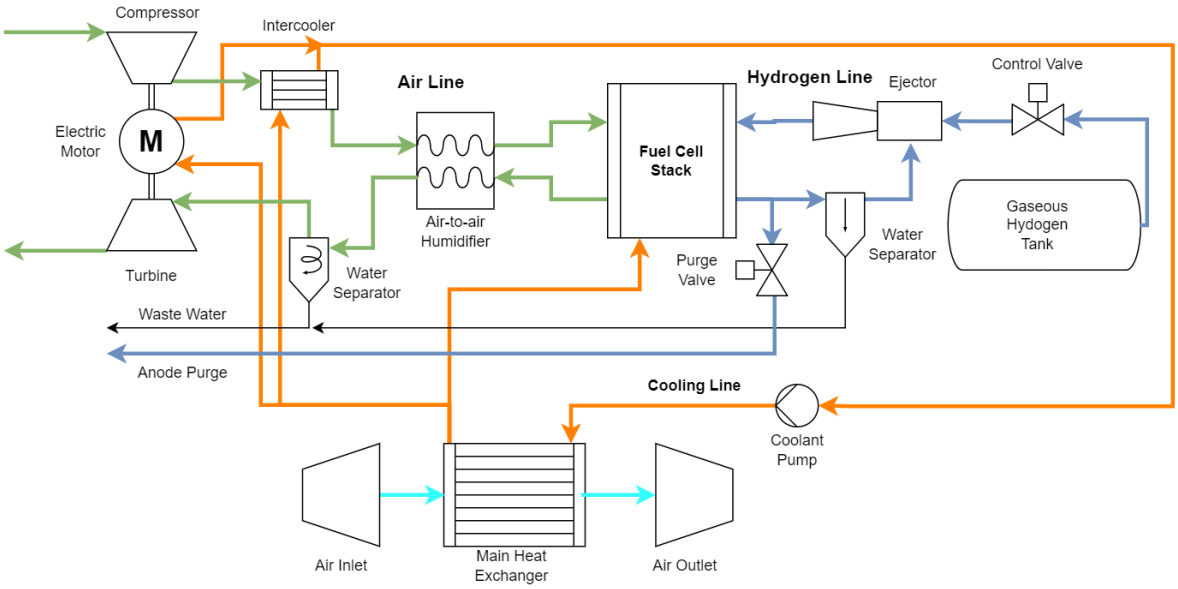


Figure 2.4: Fuel Cell System with different subsystems adapted from Refs. [22, 23].

To improve the weight of compressed storage systems that have a typical gravimetric storage efficiency of just 6.5% for composite tanks, research and development in the aviation industry is focused on liquid hydrogen storage in cryogenic tanks [34]. The gravimetric storage efficiency is defined as the mass fraction of fuel to total storage system mass according to

$$\eta_{storage} = \frac{m_{fuel}}{m_{fuel} + m_{tank}} \tag{2.20}$$

Using such a cryogenic storage system, the pressures of stored hydrogen are an order of magnitude less than compressed storage but might be enough to still employ a blow-down system. The hydrogen is evaporated from the tank and warmed up to operating temperatures, around 70-80°C, before entering the fuel cell stack. An example of hydrogen storage and feed system is presented in Figure 2.5. In this specific configuration, the hot coolant from the fuel cell thermal management system is used as the hot source to evaporate the hydrogen in an external heat exchanger. The gaseous hydrogen then is routed back to the tank where it evaporates more hydrogen inside the tank to maintain the right operating pressure. It is then fed to the fuel cell.

#### COOLING SYSTEM

The most common type of cooling solution for fuel cell systems of high power density applied in the mobility sector is liquid cooling. This cooling strategy consists of feeding a liquid to the fuel cell stack, as well as other components that may require cooling like motors or intercoolers. The liquid heats up absorbing the waste thermal energy and is then fed to a heat exchanger to reject that energy to ambient air. The loop is then closed by pumping the water back to the fuel cell. The cooling liquid is usually deionized water with additives to reduce the conductivity and lower the freezing point. A pump is used to circulate the coolant and the heat exchanger is cooled by ambient air through either the motion of the vehicle itself or fans in semi-stationary applications. In case the ram air concept is used, an appropriately designed inlet and outlet for the air passing through the heat exchanger is needed. An entire later section is dedicated to fuel cell thermal management as it is the focus of the research.

### 2.2.5. AIRCRAFT APPLICATIONS

Research on the application of fuel cells in aviation has been growing in the past 10 years in support of the commercial projects mentioned at the beginning of this chapter. One of these projects, H2Fly, is supported by DLR which has been active in this field of research for more than 10 years. For example, in 2009 [39] an

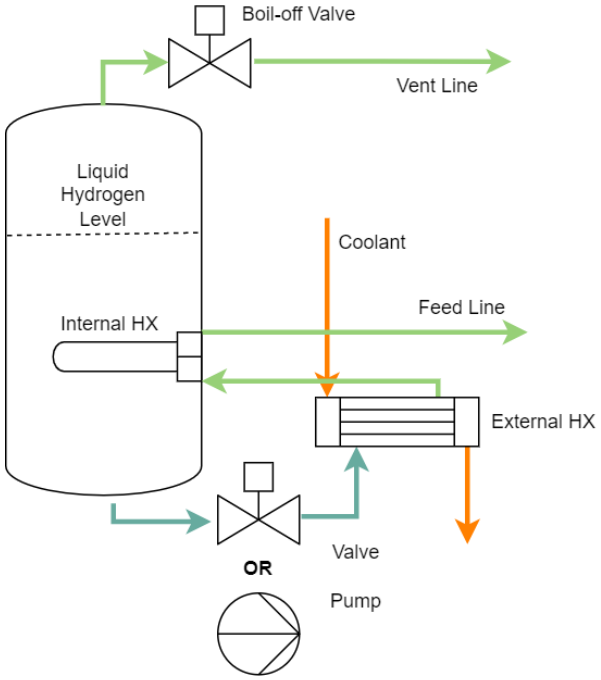


Figure 2.5: Liquid hydrogen supply system adapted from Ref. [22] and Ref. [38].

overview of the research of that time at DLR was published. Their focus was primarily on the use of fuel cells as multi-functional APUs, delivering both electricity to modern more electric aircraft as well as providing heat for on-board use, inert gas (from the oxygen-depleted exhaust) and water to humidify the cabin air. A project conducted with Airbus resulted in flight testing of such a prototype APU system and showed the added benefits of a multi-functional high efficiency (40% compared to 20%-10% of a traditional APU) system. The first test flights of an early prototype of the H2Fly project are also mentioned.

A more recent publication by Kadyk *et al.* [13] (2018) highlights the system-level consideration that needs to be made when designing a fuel cell propulsion system and hydrogen storage tank for aircraft applications. Through the use of an analytical performance model of a fuel cell, it could be shown how the optimal fuel cell size was dependent on many factors. Given the characteristics of a certain MEA, it is possible to estimate the maximum specific power per unit area of that fuel cell. After this point, due to high mass transport losses, an increase in current will result in a decrease in voltage (thus efficiency) that will diminish the actual power output. Operating after this point is thus not useful. It is further found that the change in efficiency with respect to a change in current lies in a very narrow 99% confidence interval for a large set of fuel cell designs and is mostly linear in a central region between the maximum efficiency point and the maximum power point. Given this characteristic two strategies are possible. Either weight is prioritized, to have the most power-dense system, or efficiency, to operate at higher cell voltages, reducing fuel consumption but paying a weight penalty. Designing a fuel cell for maximum efficiency only would result in an impossibly large fuel cell stack as the specific power tends to zero while operating at or close to the maximum power point might result in a very inefficient system as can be inferred from the polarization curve (Figure 2.3). Thus, a system-level approach is needed to determine the optimal size of the fuel cell and its operating point. The degree of oversizing can be represented by the ratio of maximum power to design power. It is thus between infinity (maximum efficiency, zero power) and 1 (maximum power, low efficiency). It is found that an oversizing factor for minimum weight of the fuel cell system (including storage) exists for a given mission. A mission can be characterized by the storage-to-converter ratio

$$r_{s/c} = \frac{E_{rq}}{P_{rq}} \cdot \frac{\rho_{fc}}{e_{tk}} = \frac{m_s}{m_c}. \tag{2.21}$$

Where $E_{rq}$ is the required mission energy, $P_{rq}$ the required mission power, $\rho_{fc}$ the specific power of the fuel cell (or more generally energy converter), and $\rho_{tk}$ specific energy of the hydrogen tank (or more generally the storage system).

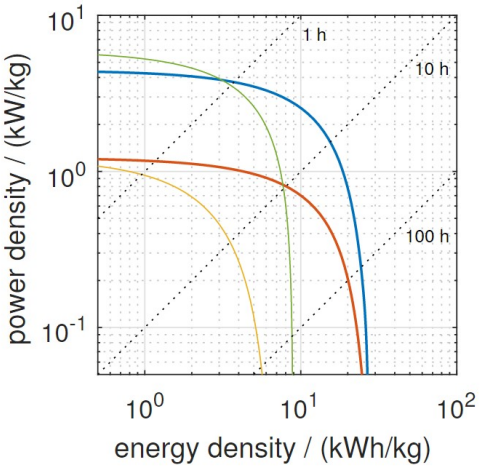


Figure 2.6: Taken from Ref. [13].

Figure 2.6 Also from Ref. [13]: Ragone plot of current and future fuel cell systems for aviation. Yellow: current fuel cells with 1.6 kW/kg incl. periphery, current electric engines with 5.2 kW/kg and simple stationary tanks. Red: current fuel cells+periphery and electric engines with LH2 tanks optimized for medium-haul flight. Blue: future lightweight, high-power fuel cells+periphery with 8 kW/kg, future electric engines with 10 kW/kg and optimized LH2 tanks. Green: current system of jet engine (Airbus A320) and kerosene tanks. Dotted lines mark time constants of 1 h (top), 10 h (middle), and 100 h (bottom)."

An exponential relationship is found that indicates that oversizing the fuel cell is more convenient at high $r_{s/c}$ when the mission energy is high. This is explained by the fact that in this case the system weight is dominated by the storage system and a bigger, more efficient, fuel cell would reduce the amount of fuel consumed. For shorter, more power-intensive missions then a fuel cell designed close to the maximum power point, with a degree of oversizing close to 1, would be more attractive to reduce system weight. These findings are extended to a Ragone plot comparing current and future fuel cell technology to gas turbine and battery technology. Although current technology suffers in pure power density in comparison to gas turbines, utilizing an optimized liquid hydrogen storage system would already result in competitive systems at a mission time of 10h.

Another paper by researchers of DLR [40] explores the optimal operating conditions of a fuel cell system for aircraft applications. The research is based on a 1D fuel cell model capable of representing water management issues such as membrane dry-out and flooding. The model was validated on a commercial fuel cell stack by the company Hydrogenics. With this model at hand, an optimization of the cell-level operating conditions resulted in expected high temperatures, pressures, and humidity levels as well as moderately high stoichiometric air ratios. When including the effect of compressor parasitic power and low ambient pressure at high altitudes, the optimal operating conditions for system-level efficiency differed considerably. Lower pressures and stoichiometries are preferred to limit the detrimental effect of compressor parasitic power. Additionally, it was found that the oversizing factor has a strong influence on the system efficiency in different flight phases. At altitude, the efficiency tends to be lower and operation at low current densities (high oversizing factor) is more beneficial. A stack sized for close to maximum power point operations at take-off will be oversized for cruise and could represent a good trade-off. Unfortunately, no representation of the thermal management system with its effect on added parasitic drag and optimal fuel cell operating temperature is included but it is suggested that further research in this aspect would improve the understanding of optimal system operating conditions.

Another recent paper by Nicolay *et al.* [12] (2021) presents a multidisciplinary design optimization routine for a general aviation liquid hydrogen fuel cell aircraft. The concept relies on fuel cells mounted in the cross-section of the wing. Given the tight geometrical constraints, the optimization does not allow for an oversized fuel cell when considering currently achievable power densities. With a higher power density, as can be expected from future development in the field, the optimization does lead to some degree of oversizing to increase efficiency and reduce fuel consumption. In general, similar performance and operational empty weight as reference general aviation aircraft were achieved with a prospective fuel cell system (only BOP without LH2 tank) with a power density of 1.72 kW/kg.

Finally, a paper by Datta *et al.* [11] in collaboration with NASA, outlines the modelling and verification of two fuel cell systems. One based on year 2000 technology and one based on modern automotive technology. It is found that a modern fuel cell system (excluding hydrogen storage) can achieve a specific power in the range of 1.5 kW/kg further supporting the design routine in the previously presented paper by Nicolay *et al.*

[12]. These models, together with detailed weight estimations of components are used to design and size a potential 500 kW system to use in an eVTOL tilt-rotor aircraft. The author opts for a fuel cell stack operating at unpressurized ambient conditions, given a low mission altitude. This option reaches lower specific power densities but reduces overall specific fuel consumption as the compressor weight and power demand can be saved. This is in contrast with the results from DLR [40] that were derived for higher altitude operation with a different application in mind pointing to the fact that a fuel cell system always needs to be tailored to the specific application.

## 2.3. FUEL CELL THERMAL MANAGEMENT

As discussed in previous sections fuel cells can be operated at relatively high efficiencies in the order of 50% - 60% at maximum power. Although it is comparatively higher than their combustion counterpart, cooling of fuel cells presents different challenges. The primary challenge is that fuel cells do not rely on hot exhaust gases to reject waste heat to ambient and a dedicated cooling strategy needs to be put in place to extract low-temperature waste heat from the system.

### 2.3.1. COOLING AND ENERGY BALANCE

The energy balance of a fuel cell is simply analyzed by taking into account the enthalpies of the reactants entering the stack, including the heating value of the fuel, the enthalpies of the reactants leaving the stack, whereas in systems with hydrogen recirculation the recirculated hydrogen can be omitted if the boundaries for the analysis are defined well, the produced electric power and the waste heat. The waste heat needs to be extracted with a cooling system to keep the fuel cell operating in a steady-state. The overall energy balance can be summarized as

$$\sum (H_i)_{\text{in}} = W_{\text{el}} + \sum (H_i)_{\text{out}} + Q, \tag{2.22}$$

and the following detailed explanation follows closely the one presented by Barbir [22]. It is important to already state that the water produced in the reaction and its state when leaving the system needs to be considered carefully as the enthalpy of evaporation of the produced water can have a large impact on the overall energy balance.

The enthalpy of the gaseous reactants can be defined as

$$H = \dot{m} c_p T. \tag{2.23}$$

It is important that a common reference temperature is used for all species throughout the analysis or the proper corrections should be applied. For hydrogen, also the heating value should be included as

$$H = \dot{m} \left( c_p T + h_{HHV}^{T_{ref}} \right). \tag{2.24}$$

Both Barbir [22] and Larminie and Dicks [23] recommend the use of the higher heating value of hydrogen in fuel cell energy analysis as it is the correct representation of the amount of energy released while the amount of water produced that actually evaporates is calculated separately.

When accounting for the enthalpy of water it should be defined differently according to the state it is in:

$$H = \dot{m}_{H2O(g)} \left( c_{p,H2O(g)} T + h_{fg}^{T_ref} \right) \tag{2.25}$$

is used for water in the gaseous state and includes the latent heat of evaporation;

$$H = \dot{m}_{H2O(l)} c_{p,H2O(l)} T \tag{2.26}$$

is used for liquid water. To close the analysis, the amount of water produced that evaporates needs to be estimated. It can often be assumed that the air stream at the cathode exits in saturated conditions. The difference in the amount of water vapour at the outlet with respect to the inlet gives the amount of produced water that evaporated inside the fuel cell. Any excess produced water that did not evaporate will be blown out from the fuel cell in liquid form.

### 2.3.2. IMPLICATIONS FOR WATER MANAGEMENT

Water evaporation, especially at the cathode where it is produced, does not only improve the cooling requirements by absorbing thermal energy through the evaporation process. It also reduces the amount of liquid water at the cathode outlet, thus limiting the risk of cell flooding. To understand better the relationship between cooling and water management, a liquid-cooled fuel cell can be used as an example.

In a liquid-cooled fuel cell, the heat transfer coefficient between liquid coolant and reactant streams is very good and only a limited temperature difference of around $1K$ is expected at the outlet in a cathode-coolant co-flow arrangement [41]. Most of the thermal energy is absorbed by the coolant with the evaporation of water being the second most important mechanism of waste heat removal. In an ideal case (100% evaporation of produced water) the heat absorbed is the difference between the higher heating value of hydrogen and the lower heating value: 141.88 $MJkg^{-1}$ vs 119.96 $MJkg^{-1}$ (15% difference) that for an assumed efficiency of 50% equals 30% of the required cooling. Another limited amount of heat is absorbed by the reactant streams. As the mechanism of heat absorption by the liquid coolant is mostly through a change in sensible enthalpy the temperature change of coolant between the inlet and outlet is inversely proportional to the mass flow rate of coolant given a constant heat load. Thus the flow rate of coolant not only controls the operating temperature of the stack but also directly influences the temperature difference between the inlet and outlet of the cathode stream.

Ideally, the cathode stream has a high relative humidity at the inlet to avoid dehydrating the membrane and keeps a high humidity throughout the cathode channel for the same reason. Additionally, the produced water is ideally evaporated without saturating the air. This can be achieved by heating up the cathode air stream and allowing it to absorb more water vapour without reaching saturation[1]. Operation at higher stoichiometries on the air side improves water management as less temperature change is needed at the cathode to ensure the full evaporation of the produced water. Thus, a complex interaction between operating conditions of cathode and coolant exists that involves cathode pressure and mass flow as well as coolant mass flow and impacts both water and thermal management in the fuel cell stack. It is thus important when designing a cooling system to include in the evaluation of its efficiency the water management aspects described above.

Indeed it has been proven by Wang and Wang [41] that a fuel cell operated with a finite coolant mass flow rate operates better than one with an ideal infinite mass flow rate that ensures almost isothermal operation. In the case of the finite flow rate of coolant, the cathode stream underwent a gradual temperature change and improved the distribution of water in the membrane as the relative humidity levels were more homogeneous throughout the cathode channel. Both membrane dryout at the inlet and flooding at the outlet were avoided.

### 2.3.3. COOLING METHODS

An extensive review of thermal management developments for PEM fuel cells has been performed by Chen *et al.* [20] and gives good insight into the possible cooling strategies. It is clear from the reviewed research that for large fuel cell stacks (>100 kW) simple cooling techniques like air cooling or heat pipes can't cover all of the required heat removal capacity, thus more advanced strategies are needed. Three main strategies exist that can be taken into account. The first is traditional liquid cooling with de-ionized or glycol-ethylene water. This has been the standard in the automotive industry and offers advantages such as high technology readiness level and reduced complexity together with simple operating control strategies. For comparative purposes with other systems, a flow diagram and temperature-entropy diagram of the liquid cooling strategy are included in Figure 2.7 and Figure 2.8. As can be seen, the working fluid remains in the fully subcooled liquid phase.

The second option is evaporative cooling. This strategy is a phase change technique in which liquid water is injected into the reactant stream before or within the fuel cell stack. Water is then evaporated due to the lower partial pressure of water vapour in the reactants. Due to the relatively high operating conditions ($\sim 80°C$) the reactants can absorb large amounts of water and thanks to the high latent heat of evaporation of water the whole cooling requirement can be met [24].

The third strategy, also based on phase change, is flow boiling. This requires a cooling fluid that boils close to the operating temperature of the fuel cell and a separate closed cooling loop as in the liquid cooling

[1] The reader shall refer to the section on operational conditions or commonly available web resources to familiarize with the properties of humid air e.g. this useful link:https://www.engineeringtoolbox.com/maximum-moisture-content-air-d_1403.html

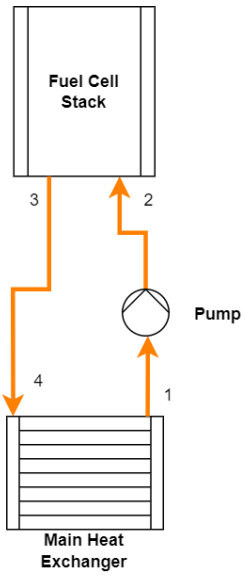


Figure 2.7: Liquid cooling flow diagram.

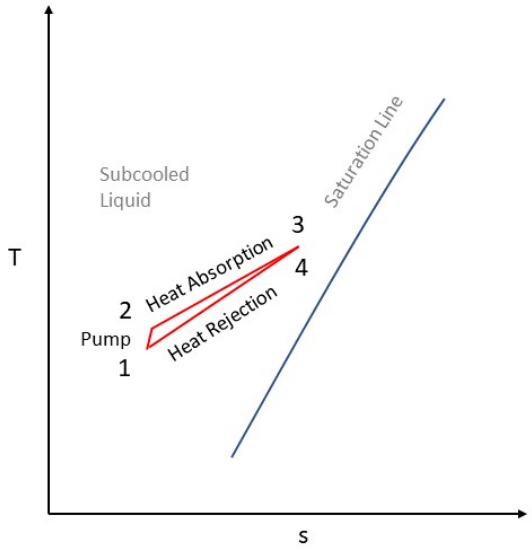


Figure 2.8: Liquid cooling temperature-entropy diagram.

case. The characteristic of this strategy is to have the benefits of both liquid cooling, in terms of simplicity and closed-loop design, as well as phase change cooling by exploiting the cooling potential of latent heat of evaporation of the cooling fluid possibly reducing the amount of fluid needed and increasing the heat transfer coefficient [27].

Although phase change systems present many challenges they also come with advantages but their TRL remains low. In fact, no current research was found on phase change strategies applied to fuel cell aircraft cooling. Most of the literature considers the traditional liquid cooling strategy for aircraft application.

### 2.3.4. COOLING IN AIRCRAFT APPLICATIONS

Current research on fuel cell aircraft thermal management focuses on the liquid cooling system. A paper by Kozulovic [15] (2020) gives a good preliminary estimate of the effect of the cooling system on the overall aircraft performance. The paper considers a passenger aircraft of similar size to an Airbus A320 powered entirely by fuel cells. Even though the external aerodynamic drag of the radiator nacelle installation is not modelled in detail, it is found that a power demand increase to offset the produced extra drag is 27.3% and the radiator cross-section is almost as big as the fuselage itself. Although the increase in required power is considerably large it also makes research in alternative solutions very appealing as margins for improvement are big.

Kellermann *et al.* [18] (2020) propose a general approach to thermal management of hybrid aircraft in which the focus is on the heat rejection to ambient air rather than the type of propulsion system employed making the presented methodology applicable also to fuel cell powered aircraft. A ram air thermal management system is sized by taking into account the drag contribution of the inlet internal (diffuser losses) and external (spillage drag) losses, outlet (nozzle) and radiator core losses. Although it might be questioned if some of the chosen loss models are directly transferable from their original intended use to the research performed (for example centrifugal compressor diffuser loss models applied to ram air inlet diffusers), a more detailed accounting of drag sources is made with respect to the research from Kozulovic [15] and serves as a reference for future work.

A paper by Chapman *et al.* [19] looks at heat exchanger optimization for hybrid electric aircraft applications. Although fuel cells are not considered in this paper the proposed methodology can serve as the foundation for fuel cell aircraft as the type of cooling architecture and drag accounting is equivalent. In this paper, puller fans are considered to provide airflow over the radiator also in static conditions. It is found that the drag due to the core flow (internal diffuser, radiator and nozzle losses) can be offset with a combination of ram jet effect and puller fans resulting in some thrust. As this research is focused on an internal heat ex-

changer (not mounted externally in a nacelle as would be the case in a fuel cell aircraft where waste heat is larger) no conclusions can be taken at the aircraft level but it does give interesting insights into the possibility of offsetting external drag with core flow thrust. Also, Kozulovic [15] found that the core flow drag was compensated by a large part (71%) by the ramjet effect. The ramjet effect is caused by the air heating up in the radiator core and thus expanding to a larger volume than the one it had entering the ram air duct. To allow for this expansion the flow of air needs to speed up and thus create some thrust.

Finally, recent research efforts of Kösters *et al.* [42] resulted in a novel fuel cell cooling approach for aircraft applications. The thermal management system proposed is based on a phase-change heat pump and resulted in drag decreases of up to 23% with respect to a conventional single-phase liquid cooling system. Water is used as a coolant and is evaporated in cooling channels inside the fuel cell. The water steam is then compressed with a compressor to high pressures (5 bar) and fed to a condenser. The condenser is cooled by ram air and the liquid water is then throttled through an expansion valve and circulated back to the fuel cell. With this approach, the temperature of the steam entering the condenser is raised to 324 °C. This leads to much higher heat transfer potential, due to the increased temperature difference with air, and results in smaller heat exchangers. The system operates at a low subatmospheric pressure of 0.2 bar in the fuel cell cooling channel and requires a compressor with a high pressure ratio of 25. A detailed design of such a compressor is not provided and it has to be verified if is feasible in practice.

## 2.4. PHASE CHANGE COOLING SYSTEMS

### 2.4.1. EVAPORATIVE COOLING SYSTEMS

The evaporative cooling strategy presented in Ref. [24] is schematically represented in Figure 2.9. Water liquid water is injected into the fuel cell stack and is evaporated at the cathode. The latent heat of evaporation of the injected water accounts for all the cooling requirements of the stack. As the evaporation of the produced water can only account for 30% of the cooling requirement the injected water is at least 2.33 times higher than the produced water. This means that the evaporated water needs to be separated again from the exhaust to be fed to the fuel cell such that the system has enough water to operate continuously. This is achieved with a condensing radiator and a water separator. A tank can cover the transient phases where the water needed for cooling is more than the one separated from the exhaust.

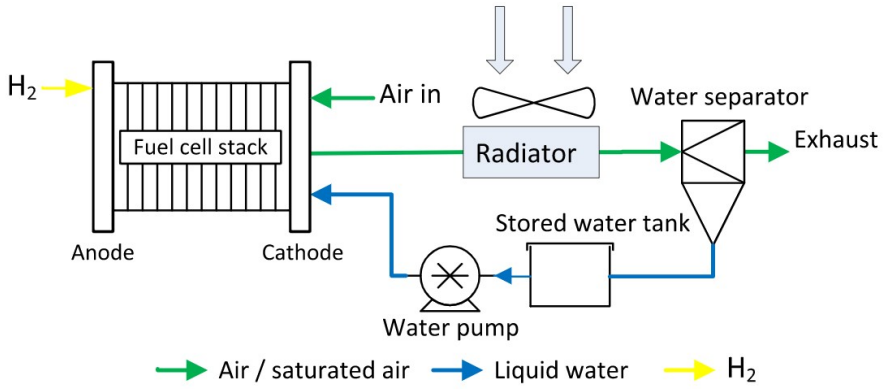


Figure 2.9: Evaporative cooling system with condensing radiator for automotive application. Reproduced from Ref. [24].

The evaporative cooling strategy has two main advantages. On one hand, no separate cooling loop is required, simplifying the system. On the other, the main radiator frontal area might become smaller [24]. The reduction in frontal area is mainly due to the improved heat transfer coefficient that is achievable in condensing radiators although it was found that the potential reduction in area can only be achieved if a highly efficient water removal solution is found (over 95%). If not enough water is separated a net positive water flow (net positive = more water is produced by the reaction than what is needed to cool the fuel cell) needs to be achieved to sustain steady-state operation. This is only possible with a reduction in stack operating temperature thus limiting the potential for heat transfer with ambient air. The operating range, in terms of current density, is also limited by the net positive water flow requirement and poses an additional limitation on the

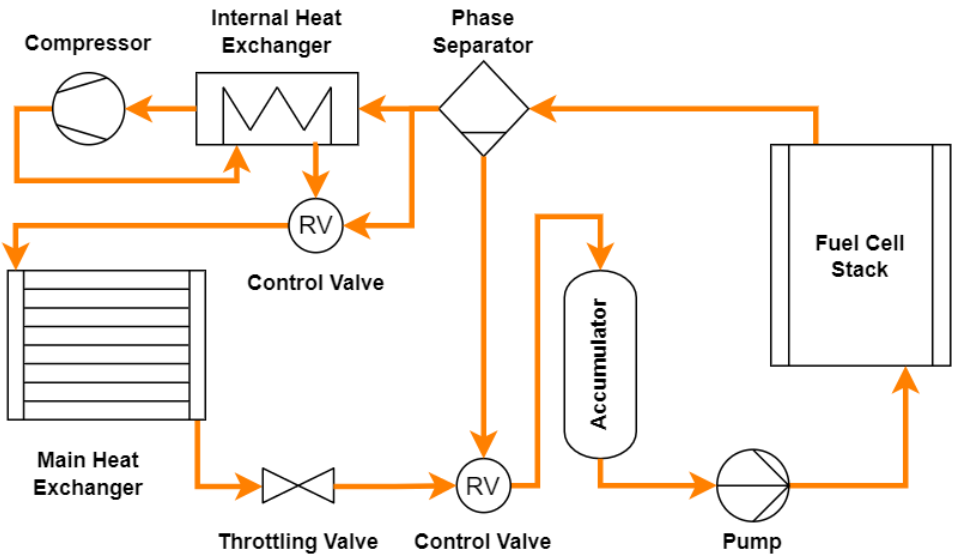


Figure 2.10: Phase change compressed cooling system for automotive applications adapted from Reichler [25].

design flexibility of such a system. Additionally, to avoid flooding of the cells usually higher stoichiometries (2.5 in the example of Fly and Thring [24]) are needed which increase the parasitic power of a blower or compressor and do not increase the efficiency of the cell much further as oxygen concentration is already high. In fact, Kulikovsky [43] shows that stoichiometries above 2.5 at the cathode have diminishing returns on fuel cell efficiency as oxygen concentration within the cathode channel is already high. The maximum operating pressure is also limited by the operating temperature as the ability of air to absorb water diminishes with increasing pressure and imposes additional constraints [44]. Further drawbacks of the evaporatively cooled system include the necessity of using de-ionized water to avoid damaging the stack. This last requirement forbids the use of traditional condensing radiators made of aluminium as corrosion would result in contaminated water. If a stainless steel heat exchanger needs to be used, lower heat transfer coefficients are expected resulting in a larger frontal area and higher weight.

### 2.4.2. FLOW BOILING COOLING SYSTEMS

A flow boiling system as depicted in Figure 2.10 uses a separate closed-loop circuit but offers some of the advantages of the evaporative system. The increased heat transfer coefficient of a condensing flow can still be exploited in the condenser (acting as the main radiator as in the case of evaporative cooling) while the separate closed loop does not pose any contamination risk to the stack and does not require separation from the exhaust stream[25]. Furthermore, the latent heat of evaporation rather than the sensible heat is used to cool the stack as well allowing for weight-saving as the amount of fluid needed is less than in a liquid cooling system. Additionally, the stack operation is independent of the cooling system and more flexibility is achieved in dealing with different power settings and ambient conditions. Finally, as the system is closed from the environment, the possibility exists of pressurizing the vapour before entering the condenser, increasing its temperature and raising the potential for heat transfer with ambient air. This will come at the expense of needing a compression system which consumes power and adds weight. Investigations of these possibilities have been carried out by Reichler [25] in his PhD thesis and it was found that the increased system parasitic power due to the compression system can be offset by the gain in cooling capacity. The proposed system (shown in Figure 2.10) becomes effectively a high-temperature heat pump and can be analyzed with methods proposed in Ref. [45].

It is not clear from existing literature what the effects on the whole system performance of such a compressed phase change cooling system could be and more research is needed to understand if the trade-off between additional system power, complexity, and weight and increased heat transfer potential is beneficial in an aviation setting. Furthermore, the increased cooling fluid temperature might enhance the ram jet effect and offset even more drag.

## 2.5. ADVANCED STRATEGIES AND CONSIDERATIONS ON FLOW BOILING SYSTEMS

In this section the flow boiling strategy will be analyzed in more detail and topics that require additional care when designing such a system will be explored. First, more fundamental considerations on the heat transfer characteristics, water management and component design will be made. Then a system-level description of possible configurations will be presented. Finally, proposed systems and strategies available in open literature will be presented.

### 2.5.1. HEAT TRANSFER CHARACTERISTICS

The heat transfer characteristics of boiling fluids have been studied for a long time and correlations can be found in [46]. The coolant channels present in bipolar plates of fuel cells have cross-sections that are often in the $1 mm^2$ order of magnitude (for example the ones used by Wang and Wang [41]). At small hydraulic diameters, the effect of surface tension grows significantly and impacts the fluid dynamic behaviour. When this happens the channel can be regarded as a mini- or micro-channel and different correlations must be used for this application for example the ones proposed by Kandlikar [47]. Kandlikar proposes that minichannels are channels with hydraulic diameters below 3mm and that microchannels have hydraulic diameters below 200µm [48]. Further research on the topic of microchannel flow boiling has been conducted by Thome [49, 50] who published a book on the topic. An important aspect of this type of flow boiling mechanism is that, depending on the geometry, fluid and operational properties of the system, the flow regime inside the channel can change significantly and the heat transfer properties accordingly. A model that relates the heat transfer properties to the flow regime has been proposed by Harirchian and Garimella [51]. Finally, it must be taken into account that pressure fluctuations due to bubble instabilities and heat transfer coefficient degradation due to dry-out can impose significant limitations on the amount of fluid that can be evaporated. This implies that conditions at the exit of the cooling channels will be still saturated. If high vapour qualities are reached the reduction in heat transfer coefficient due to dry-out might result in thermal instability of the fuel cell. Aspects regarding these instabilities have been summarized in a review paper by Mao *et al.* [52] and different strategies involving geometrical design or operational aspects exist to limit instabilities. Once the heat transfer characteristics are understood, traditional heat exchanger design and analysis methods can be used to size the required external heat exchanger. In this respect a book with design guidelines for different types of heat exchanger layouts and geometries has been written by Shah and Sekuli [53].

### 2.5.2. EFFECTS OF ISOTHERMAL FLOW BOILING

Operating a fuel cell in isothermal conditions is not ideal [41]. When utilizing pure substances as cooling fluid in a flow boiling application problems arise as the phase change of a pure substance is isothermal. This can influence negatively water management at the cathode side. Operation at low humidities or with large amounts of liquid water present at the cathode outlet needs to be validated experimentally to ensure that no drying or flooding of the membranes occurs. A more advanced strategy could be to make use of multicomponent fluid mixtures as cooling fluid. This idea has not been found applied to fuel cell flow boiling cooling systems and was inspired by literature in a related field. In fact, the field of closed power cycles [54] and heat pumps serve as a good source of theory and methods. The working principle of a heat pump, also called reverse Rankine cycle or vapour compression cycle, is equivalent to a flow boiling fuel cell cooling cycle in which the heat source is the fuel cell and the heat sink is the ambient air. Thus, literature on high-temperature heat pumps, working above ambient temperatures, not for refrigeration purposes but for heating purposes, or organic Rankine cycles, their power-generating counterpart, can be of great importance to the proposed research. The pioneering literature in this field by Angelino and Colonna [55] already recognized the problem of non-isothermal source and sink matching and proposed the use of multicomponent mixtures to solve it. Research on mixtures that undergo a non-isothermal phase change, also called zeotropic mixtures, is available and can be used to estimate important parameters like the heat transfer coefficient in the fuel cell during the evaporation phase [56] and in the external heat exchanger during the condensing phase [57].

### 2.5.3. FLUID PUMPING AND COMPRESSION DEVICES

When considering a closed-loop flow boiling system two strategies can be applied. The first strategy is to use a pump to overcome the pressure drops in the system and drive the fluid from the fuel cell to the heat

exchanger and back. In this case, the pump is positioned on the liquid side of the system and the most important consideration, apart from weight and size, is to avoid cavitation. Typically, cavitation is a problem in radial pumps where the pressure on the surface of the impeller blades and at the suction side, falls lower than the boiling point of the fluid at the given temperature. When this happens bubbles form in the fluid and collapse again when higher pressures are encountered towards the exit of the pump. The implosion of the bubble can lead to severe damage on the surface of the blades and the bubbles can lead to flow instabilities. Thus, cavitation has to be avoided. A thorough explanation of this phenomenon is given by Brennen [58] in their book on the hydrodynamics of radial pumps. The topic of cavitation is of special interest in this case as the fluid has a limited amount of subcooling after the condensing radiator and thus is close to the saturation line. Additionally, the fluid has to enter the fuel cell, right after the pump, close to saturation to ensure that a phase transition is present throughout the cooling channels.

The second option is to pressurize the vapour section of the cycle to raise the vapour temperature. This is essentially the strategy that a heat pump uses to transfer thermal energy from a cold source to a hot source. In the case of the considered application, the source of heat is typically hotter than the ambient air and heat would flow naturally to the ambient but the rate of heat transfer can be improved or the heat transfer area of the external radiator reduced. Several concerns need to be addressed when considering this option. The first regards the increased power demand of a compressor with respect to a pump. As already mentioned, Reichler [25] explores this in his dissertation and it will be one of the main variables that will be explored in this thesis. It has to be shown that the advantage of the higher temperature offsets the disadvantages in parasitic power. Furthermore, heat pumps are either used in stationary applications, like home heating or have to deal with limited heat duties, like environmental control systems in cars and aircraft. The compressors used traditionally in these applications are volumetric compressors which contribute significantly to the system mass. For example, an environmental control system sized for a large helicopter by Mannini [59]. An alternative to volumetric compressors are radial compressors. Preliminary studies on the use of radial compressors in heat pumps have been carried out by Schiffmann and Favrat [60, 61] and their findings point to the benefits of operating oil-free, thanks to self-lubricated foil bearings, and the possibility to easily designing multi-stage machines. Additionally, significant weight savings could be achieved. For example, a radial compressor for an aircraft environmental control system designed to operate with an olefin fluid is an order of magnitude lighter than a scroll compressor from Danfoss designed for the same cooling power working with R134A[2] [62]. An important limitation of radial compressors is that they can get damaged easily when droplets of liquid coolant are entrained with the vapour. Thus it must be ensured that only vapour enters the compressor by either separating the liquid part at the exit of the fuel cell or superheating the vapour before the compressor inlet. These considerations will have an impact on the layout of the cooling cycle as was already shown by Reichler [25].

### 2.5.4. HYBRID OPERATION BETWEEN PUMPED AND COMPRESSED SYSTEMS

If space and weight constrain allow it and a benefit can be identified, a hybrid system can be employed where both a pump and a compressor operate the system. This configuration already could improve the operation of a low-temperature heat pump to be used in data centre cooling [63]. The idea behind the concept is that when the ambient temperature is high, the compressor is operated to raise the coolant temperature above ambient temperature and drive the heat rejection to ambient air. When, during the winter months, the air temperature is lower than the operational temperature of the data centre then a simple pumped system can be used in which the phase transition still takes place but the temperature of the vapour side is not changed. Similarly, an aircraft has two main operating conditions that vary greatly in terms of heat duty and ambient temperature. During takeoff, ambient temperatures are typically high and according to the latitude of operation and season can reach up to $40°C$. On the other hand, during cruise conditions much lower temperatures (even below $-50°C$) are encountered and the required power is less. This might open up the possibility to operate the system only with a pump in cruise and save the compressor power to increase the system efficiency.

### 2.5.5. PUMPED MULTI-PHASE SYSTEM OVERVIEW

The phase change system in which the fluid is simply circulated with a pump and no compression is present is often called a *Pumped Multi-Phase* system and it is used in high-performance electronic cooling for instance satellite sensors or antennas [64]. The main function of the pump is to overcome the pressure drop over the

[2] From personal communication with Aeronamics B.V.

cooling lines although the possibility exists of pressurizing the evaporation side of the loop to control the evaporation temperature. This can be achieved with a valve after the evaporator, which in the case of a fuel cell system is the fuel cell stack itself, as shown in Figure 2.11. The evaporation happens at a slightly higher pressure than the condensation thus no temperature lift is present in such a system. In the system shown the evaporation does not reach the superheated vapour state (see Figure 2.12) as is common in applications where the temperature homogeneity is important and the heat transfer coefficient needs to be kept high. Another common strategy is to pass the flow at the outlet of the pump through a heat exchanger in counter flow with the flow coming from the evaporator. In this way, the fluid approaching the evaporator reaches saturation conditions before entering the evaporator while the pump can work in a sufficiently subcooled state to avoid cavitation [64]. Merino *et al.* [64] suggest that the most important parameter for choosing the working fluid for a PMP system is the pressure drop per transported heat through the system as it defines the size of the pump and the power consumption. A figure of merit is proposed that takes into account only the fluid's contribution to pressure drop and heat transport that can be used to select an appropriate working fluid.

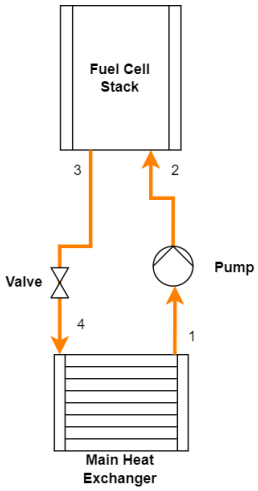


Figure 2.11: Pumped multi phase cooling flow diagram.

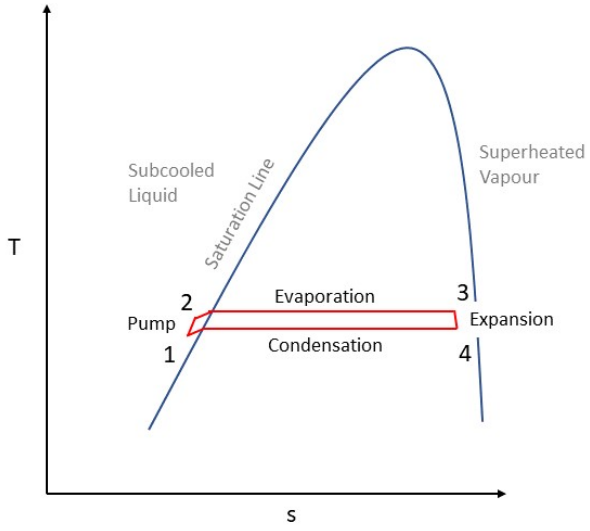


Figure 2.12: Pumped multi phase cooling temperature-entropy diagram.

### 2.5.6. VAPOUR COMPRESSION SYSTEM OVERVIEW

If a flow boiling cooling system operates with compressed vapour it can be defined as a vapour compression system. These systems are mainly used as heat pumps for refrigeration, air conditioning or heating in many different industrial and home applications. The main idea behind a VCS is that the amount of energy that can be transferred between two sources is many times more than the energy that is used to compress the vapour. After compression, the vapour reaches higher temperatures and thus rejects heat to a sink that might be at a higher temperature than the heat source. A valve is then used to throttle the condensed vapour back to its evaporation pressure. The degree to which the fluid gets subcooled in the condenser will affect the starting vapour quality in the evaporation. A simple vapour compression cycle diagram is given in Figure 2.13 while the related thermodynamic cycle representation in the T-s plane is given in Figure 2.14. A typical variation of the vapour compression cycle consists in integrating an internal heat exchanger that transfers heat from the high-pressure condensate at the exit of the condenser with the low-pressure vapour at the exit of the evaporator. In this way, the fluid is both subcooled after the condenser and superheated after the evaporator at the same time and better throttling as well as avoiding condensation in the compressor is achieved [45]. The choice of fluid impacts the pressure at which evaporation happens matching the operating temperature of the fuel cell. Another important aspect of fluid selection is molecular complexity. The molecular complexity of the fluid has an impact on a wide range of aspects including the specific enthalpy of evaporation and the critical temperature and pressure of the substance. Additionally, the slope of the saturated vapour line is affected

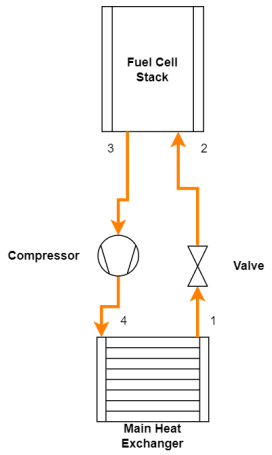


Figure 2.13: Vapour compression cooling flow diagram.

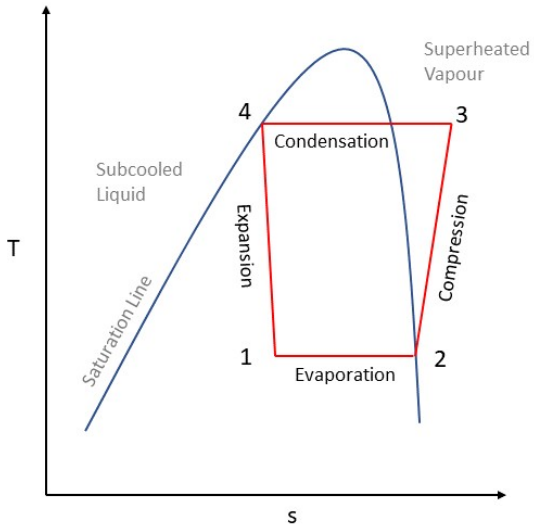


Figure 2.14: Vapour compression cooling temperature-entropy diagram.

by molecular complexity which influences the operation of the compressor and the degree of superheating at the end of the compression. In an ideal case, the degree of superheating is kept as low as possible which can be achieved with fluids that have a near straight or slight positive saturated vapour line. Fluids with high molecular complexity and their impact on system design and performance has been analyzed extensively by Angelino and Invernizzi [65] already in 1988. Some general considerations when choosing a coolant fluid for this application include [27]:

- Ozone depletion potential and global warming potential of the fluid
- Saftey, handling toxicity and flammability
- Low conductivity and dielectric behaviour
- Freezing temperature below minimum operational and non-operational temperatures
- High latent heat of vaporization and specific heat
- High thermal conductivity and low viscosity
- Low ratio of specific volumes between liquid and vapour

Additionally, the effect of the working fluid on compressor design for a radial machine has been explored by Giuffre *et al.* [62, 66] and Ascione *et al.* [67]. It has been found that radial compressors can encounter manufacturing limitations if the system needs to work with low volumetric flow rates and this should be considered when designing a vapour compression system. A fluid with a high volumetric flow rate was identified as viable for a radial compressor although with the disadvantage of a larger, heavier condenser to reduce pressure drop during condensation.

### 2.5.7. APPLICATION TO PEM FUEL CELLS

Garrity *et al.* [28] explored the use of phase change cooling in a fuel cell in 2007. In his research, he investigated the use of a thermosiphon system to cool a cold plate that simulated the typical heat generation in a fuel cell. The thermosiphon concept relies on the difference in density that is established throughout the hot and cold part of the system to drive the fluid flow. The channels that cool the cold plate are in the range of hydraulic diameter to show typical microchannel boiling flow behaviour. The flow through the cycle is influenced by the thermal energy input and is limited by instabilities at high heat fluxes. The maximum heat flux that could be sustained before the onset of instabilities was 32kW/kg which is more than a typical fuel cell considered for aviation application would produce. The main focus of the research was on assessing the instabilities that

would form due to the adverse change in pressure drop caused by the vapour phase at high heat fluxes. This phenomenon, called Ledinegg instability, limits the maximum amount of heat that can be rejected by the system. The fluid used in the experiment was HFE-7100 with a saturation temperature at ambient pressure of $61^{\circ}C$ which ensures enough cooling channel wall superheat to ensure boiling while keeping the cold plate within fuel cell operating conditions between $66^{\circ}C$ and $82^{\circ}C$.

Different fluid and cooling system concepts were used by Soupremanien *et al.* [27]. In this research paper, a simple pumped cooling cycle is considered and the focus is shifted to the effects of cooling channel geometry on the onset of nucleate boiling (ONB) and the critical heat flux (CHF) at which dryout starts to happen. The fluid used is Forane 365 HX with a saturation temperature of 55°. The ONB and CHF points are critical as the best heat transfer coefficients can be achieved within these two points. Especially after the critical heat flux the fluid in contact with the walls creates a vapour blanket that severely reduces the heat transfer coefficient. Thus operating at heat fluxes above the CHF point is to be avoided at all costs. The flow within the channels does not behave like a microchannel flow as the channels considered are bigger than in Ref. [28]. During the experiments, the heat transfer coefficient of single-phase Forane was also analyzed and it was found that the boiling fluid can have an HTC up to 3 times higher. The critical heat fluxes of the different channel configurations investigated were compared against typical heat fluxes present in fuel cells and all channel geometries show promising results in the ability to cool the fuel cell without incurring CHF and staying above ONB. The best channel is then selected based on the lower pressure drop characteristics. Unfortunately, no empirical or analytical correlation is presented that could be used to predict ONB and CHF in different channel geometries. Additionally, no analysis of the vapour quality development through the channel is included.

A numerical study of flow boil cooling of fuel cells was conducted by Choi *et al.* [26]. In his study, the thermal energy released by the reaction along the membrane face was dependent on oxygen concentrations on the catalyst and was higher at the cathode outlet during operation at high current densities. His model could also represent the temperature distribution normal to the membrane plane from anode to cathode. The findings show that boiling HFE-7100 can maintain a better temperature uniformity along the cooling channel with respect to single-phase HFE-7100 at equal mass flow rates. Furthermore, the delayed onset of nucleate boiling was captured well and depended on the mass flow rate of the coolant if the current density was kept constant. At high mass flow rates, the ONB was delayed but the heat transfer coefficient did not change significantly and the temperature uniformity was maintained. An important conclusion is that the mass flow rate has to be adjusted to operating conditions to avoid dry-out. It is indeed the case that the heat flux at which dry-out occurs is dependent on vapour quality and flow conditions. This limits the amount of fluid that can be evaporated as the vapour quality at the outlet cannot be too high. Finally, the possibility of regulating the operational temperature by pressurizing the coolant was explored. At higher pressures, the saturation temperature increases and the coolant flows in single phase for a larger portion of channel before ONB is reached. The vapour quality at the outlet of the cooling channel remains close to constant and ensures that no dryout is encountered. This proves to be a successful strategy to control fuel cell temperature.

The numerical results were further validated with an experimental campaign performed by [29] on a cold plate reproducing typical channel geometries and heat fluxes as seen in PEM fuel cells. The fluid used was HFE-7100 and the results showed that phase change flow boiling was an effective cooling strategy. In particular, it was found that although the heat transfer coefficient was affected by heat flux and vapour quality, it was not affected by mass flux. The cause was identified in the boiling regime which was mainly nucleate boiling. Nucleate boiling is a boiling regime in which the heat transfer coefficient is mainly influenced by the heat flux, thus the boiling intensity, and not the fluid flow as is commonly the case in single-phase heat transfer or convection boiling. Only when mass fluxes were low enough to incur partial dry-out the heat transfer coefficient would drop. It was found that a maximum wall superheat of 25 K can be reached in critical heat flux conditions thus appropriate control of the flow boiling is needed to avoid damaging the fuel cell.

# 3

# METHODOLOGY

To address all the relevant physical phenomena of a ram air fuel cell cooling system using single-phase or two-phase cooling, without introducing too much modelling complexity, a 0D lumped-parameter approach is used. This approach simplifies the modelling of the system as each component is modelled as a separate unit and the distribution of physical quantities within each component is assumed to be uniform. Furthermore, the performance of the system is evaluated only at the design conditions. Thus all components are modelled in steady-state. Only when evaluating the temperature distribution of the cooling plate of a fuel cell the 0D approach is insufficient and a 1D approach is preferred. This approach resolves the evolution of relevant physical quantities in a single spatial direction.

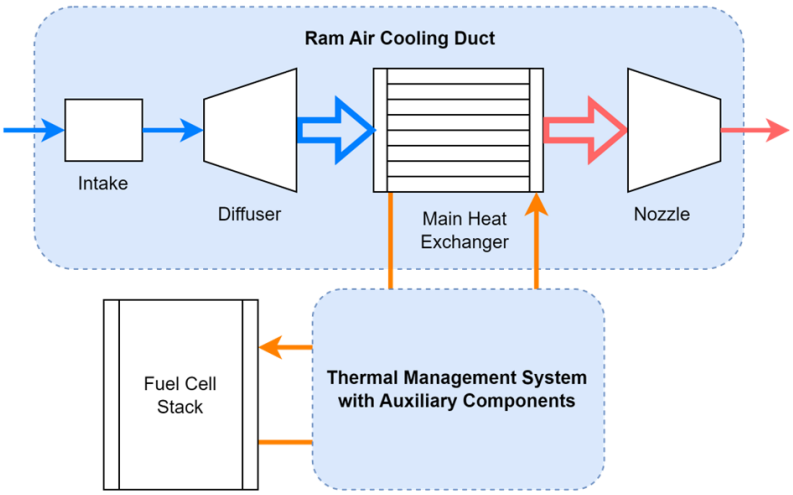


Figure 3.1: High level thermal management system and ram air duct representation.

A general representation of the overarching thermal management concept is shown in Figure 3.1. The fuel cell stack is always present as the heat source and only the cooling channels are modelled in detail. The main heat exchanger residing in the ram air duct is common to all systems but acts as a single-phase exchanger, condenser, or a combination of both according to the selected architecture. The ram air duct has an inlet, which is modelled to capture primarily external aerodynamic forces. A diffuser is placed between the inlet and main heat exchanger to slow down and compress the flow. The diffuser model serves to predict the maximum allowable area ratio before boundary layer growth and stall degrades the pressure recovery of the core flow. Finally, a nozzle is added after the main heat exchanger to expand and accelerate the core flow to ambient pressure. The components used to connect the fuel cell and main heat exchanger are defined

as auxiliary components to the specific system they are used in. For example, Figure 3.2, shows a possible implementation of a thermal management system based on the vapour compression system concept. Other architectures considered in this work are presented in section 3.8 to section 3.10.

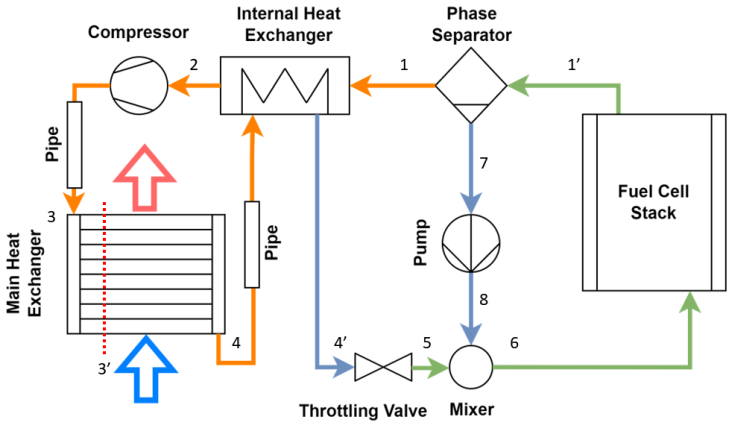


Figure 3.2: Example of VCS system further treated in section 3.10.

## 3.1. COOLING FLUID SELECTION

The first step in designing and modelling a cooling system is the choice of a cooling medium. In the case of a conventional single-phase cooling system used in the mobility sector an ethyl-glycol water mixture (EGW) is used. This coolant has a saturation temperature that is above the operational temperatures of PEM fuel cells at ambient pressure, thus remains liquid at all times during operation, and possesses thermal characteristics that are favourable to fuel cell operation like a high heat capacity and thermal conductivity. As fuel cells are often designed to be used with a specific coolant only and the objective of this study is to explore a solution that is practical and could be easily implemented as a viable alternative, the alternative coolant choice has to match the physical properties of the coolant used conventionally and the operating boundary conditions imposed by the fuel cell.

For a flow boiling cooling solution, the saturation conditions need to be within the operating temperatures of the fuel cell with an additional temperature margin of 10 to 20 K to ensure proper heat transfer from the cooling plate walls to the boiling fluid [28]. Additionally, the saturation pressure of the coolant needs to be above ambient temperature and below the maximum operating pressure of the fuel cell stack. Sub-ambient operation should be avoided to minimize the risk of air leaking into the cooling system [25] and the coolant should not freeze at low ambient temperatures encountered during the lifespan of the intended application. The latent heat of evaporation of the coolant should be as high as possible to minimize the mass flow rate of the system and reduce system power. The thermal conductivity of the fluid should be as high as possible to ensure a high heat transfer coefficient and the viscosity low to reduce pressure drops which not only affect the power needed to circulate the coolant but also affect the saturation temperature. The pressure drop in two phase flow is also influenced by the ratio of vapour to liquid phase density and this ratio should be low to minimize pressure losses. The coolant should have good dielectric properties and low electrical conductivity as within the fuel cell it is in direct contact with the current carrying bipolar plates and a risk of internal leakage currents exists. Furthermore, the coolant should be safe for both the operators of the system and the environment, meaning that low toxicity as well as low global warming potential (GWP) and low, if not null, ozone depletion potential (ODP) are favourable [27]. The flammability of the coolant is also to be considered a potentially hazardous property although flammable substances are an integral part of both the conventional (kerosene) as well as future (hydrogen) airplane concepts thus they are not to be excluded a priori and proper safety measures should be put in place for their use instead. Finally, the coolant should be compatible with the materials used in the system and have generally low corrosive properties. In summary, the desirable characteristics of a cooling medium to be used in a flow boiling system are:

- Saturation Temperature: 60 to 80 °C
- Saturation Pressure: 1 to 5 bar
- High latent heat of evaporation
- High thermal conductivity
- Low viscosity
- Low ratio of vapour to liquid density
- High dielectric constant
- Low electrical conductivity
- Low toxicity
- Low/Null GWP
- Null ODP
- Not corrosive and well compatible with a wide range of materials
- (Low/Null Flammability)

### 3.1.1. SELECTION CRITERIA

In addition to the desired characteristics, the coolant should also ensure that the resulting system has a good performance. The performance of a cooling system considered separately to the overall system performance can be easily expressed with the coefficient of performance (COP). This coefficient, which is conventionally used in refrigeration systems and heat pumps is defined as

$$\mathrm{COP} = \frac{\dot{Q}_{\mathrm{cool}}}{\dot{W}_{\mathrm{sys}}}, \tag{3.1}$$

and represents the ratio of useful cooling effect to cooling system power. The useful cooling effect to be achieved is a requirement from the fuel cell while the system power is a result of the fluid selected and system design. In PMP systems the system power is mainly dominated by the coolant pump that needs to circulate the coolant from the fuel cell to the main heat exchanger. The pump power is thus a function of the mass flow rate of coolant and the generated pressure drop through the system piping and components. In a VCS system, where the saturation temperature in the condensing main heat exchanger is higher than the saturation temperature in the fuel cell, the system power is mainly dominated by the compressor that needs to pressurize the vapour. Here the main factors that influence the COP are the thermodynamic characteristics of the fluid and their influence on the differing properties of the fluid at high and low saturation pressures. The pressure drop encountered in the system components is thus of secondary importance.

As the PMP and VCS systems are affected by fluid characteristics differently two different strategies are necessary to evaluate the fluid choice. Additionally, a fluid database is necessary for both strategies and the REFPROP database of NIST is used for this purpose [68]. The fluid properties from the REFPROP database are evaluated through the CoolProp interface [69].

#### FIGURE OF MERIT FOR PUMPED MULTI-PHASE SYSTEMS

As selection criteria for a PMP system, the method proposed by the NLR for space thermal control systems is used [70]. Although the method is presented for space application it is based on fundamental fluid and system properties that do not differ from application to application and is thus generalizable. The method uses figures of merit, which have no physical meaning on their own but shall be used comparatively within a set of fluids to be evaluated. Two figures are proposed: the first one,

$$M_{\Delta \mathrm{p}} = \frac{1}{\mu_{\mathrm{l}}^{1/4} / \left(\rho_{\mathrm{l}} {h_{\mathrm{lv}}}^{7/4}\right) + \mu_{\mathrm{v}}^{1/4} / \left(\rho_{\mathrm{v}} {h_{\mathrm{lv}}}^{7/4}\right)}, \tag{3.2}$$

represents the pressure drop that the fluid generates and the second one,

$$M_{P_{pump}} = \frac{\rho_l h_{lv}}{\mu_l^{1/4} / \left(\rho_l {h_{lv}}^{7/4}\right) + \mu_v^{1/4} / \left(\rho_v {h_{lv}}^{7/4}\right)}, \tag{3.3}$$

represents the pump power. In both cases only the effects of the fluid on system performance are considered and the effects of system geometry or overall power demand are excluded. The denominator in both figures represents the pressure drop and is dependent on both vapour and liquid viscosity, density and volumetric flow rate. The latter is inversely proportional to the latent heat of evaporation and the fluid density as in

$$\dot{V} \propto \frac{1}{\rho h_{lv}}. \tag{3.4}$$

In the low pump power figure the pressure drop is multiplied by the volumetric flow rate. High values of the proposed figures are comparatively better and represent low pressure drop and low pump power respectively.

An additional requirement for a good cooling fluid is a high heat transfer coefficient. The work by NLR does not include a figure of merit for the heat transfer coefficient, thus a new figure of merit is proposed. This figure is derived from the flow boiling heat transfer correlation proposed by Kandlikar and Balasubramanian [71] and discussed in subsection 3.2.4, Equation 3.58. The correlation is a function of boiling and convective numbers and the heat transfer coefficient of the fluid in its liquid phase.

For laminar flow, which is the dominant flow regime in fuel cells, the two-phase heat transfer coefficient becomes

$$h_{TP} = f\left(Bo^{0.7}, Co^{-0.9}, Nu_{lam}\right) \tag{3.5}$$

As shall be proven with the analysis of the geometry of fuel cell cooling channels, Bo, defined as

$$Bo = \frac{q_{ch}}{G\, h_{lv}}, \tag{3.6}$$

is only a function of geometry, if the outlet vapour quality is imposed to be equal for all fluids. Additionally, If the channel geometry is given, the laminar Nusselt number becomes a function of thermal conductivity only. Finally, Co, which is defined as

$$Co = \left(\frac{\rho_v}{\rho_l}\right)^{0.5} \left(\frac{1 - x_{vq}}{x_{vq}}\right)^{0.8} \tag{3.7}$$

is dependent on vapour quality and the ratio of vapour to liquid densities. Only the latter is a function of the fluid as the outlet vapour quality is fixed. The terms that depend on the fluid for the three numbers that influence the heat transfer coefficient are thus:

$$Bo: const, \tag{3.8}$$

$$Co: \left(\frac{\rho_v}{\rho_l}\right)^{0.5}, \tag{3.9}$$

$$Nu_{lam}: k. \tag{3.10}$$

Neglecting the constant term related to $Bo$, a new figure of merit that represents the relative performance of boiling heat transfer coefficient between fluids, is proposed and expressed as:

$$M_{h,TP} = k\left(\frac{\rho_v}{\rho_l}\right)^{-0.45}. \tag{3.11}$$

### FIGURE OF MERIT FOR VAPOUR COMPRESSION SYSTEMS

To select the best fluid to be used in a VCS system the COP in its conventional form can be used. For an ideal gas working in an ideal refrigeration cycle with no entropy generation, the COP can be proven to be only a function of temperature and is equal to

$$COP_{cooling} = \frac{T_{Cool}}{T_{Hot} - T_{Cool}}. \tag{3.12}$$

As can be inferred from the relation a higher difference between the low and high temperature in the cycle reduces the COP and increases the system power. Thus, the fluid that allows the highest COP for the given temperature levels should be used.

In a real heat pump, the calculation of COP is not straightforward as many aspects, including pressure drops, thermodynamic characteristics of fluids and component efficiencies, affect the overall system power requirement. In order to estimate the real COP of such a system a simplified model is used. This model calculates all the thermodynamic states of the fluid throughout the system and is able to calculate the necessary fluid mass flow rate and compressor power to cool a fuel cell.

The model follows the station numbers presented in Figure 3.2 and calculates the thermodynamic state by constraining two thermodynamic state variables of the fluid according to the design constraint at each station. The pressure drop due to coolant flow in pipes is neglected at this preliminary stage. The explanation of system architecture and design constraints is given in section 3.10.

When two thermodynamic state variables are constrained the remaining quantities are calculated using an equation of state as provided by REFPROP. The notation used here is for example $T(p,h)$ to be intended as $T$ function of $p$ and $h$ evaluated through the equation of state.

The first station is 1' and is at the fuel cell cooling channels outlet. Here the imposed boundary conditions are the saturation conditions, either temperature or pressure, and the vapour quality. In a VCS applied to fuel cell cooling the fuel cell acts as the evaporator and the notation "evap" will be used. As dry-out of the cooling fluid needs to be avoided a vapour quality of $x_{\mathrm{vq1'}} = 0.8$ is used for preliminary calculations as indicated in Ref. [72]. Additionally, a pressure drop of 2% is imposed at the cooling channel outlets.

$$\begin{aligned} p_{1'} &= p_{\mathrm{sat}}(T_{\mathrm{evap}}) \cdot 0.98 \\ h_{1'} &= h(p_{1'}, x_{\mathrm{vq1'}}) \end{aligned} \tag{3.13}$$

After the cooling channels, the vapour phase is separated from the liquid phase in order to safeguard the operation of the centrifugal compressor which might be damaged if liquid particles hit its fast-spinning impeller blades. The conditions at station 1 differ from station 1' only in the vapour quality $x_{\mathrm{vq1'}} = 1$.

$$\begin{aligned} p_1 &= p_{1'} \\ h_1 &= h(p_1, x_{\mathrm{vq1}}) \end{aligned} \tag{3.14}$$

Before entering the compressor the cooling fluid is super-heated in order to minimize the risk of condensation droplets entering the compressor. A degree of superheating of 5K is used.

$$\begin{aligned} T_2 &= T_2 + 5\mathrm{K} \\ p_2 &= p_1 \end{aligned} \tag{3.15}$$

The compressor is modelled with an isentropic efficiency of $\eta_{\mathrm{comp}} = 0.75$. The enthalpy at the compressor outlet, station 3, can be found using the isentropic enthalpy and efficiency using

$$h_3 = \frac{h_{3\mathrm{s}} - h_2}{\eta_{\mathrm{comp}}} + h_2. \tag{3.16}$$

The pressure after the compressor is set by the condenser pressure which in turn is a function of the specified condenser saturation temperature and the isentropic enthalpy is found by using the entropy at station 2.

$$\begin{aligned} p_3 &= p_{\mathrm{sat}}(T_{\mathrm{cond}}) \\ h_{\mathrm{s}3} &= h(p_3, s_2) \end{aligned} \tag{3.17}$$

As the compressor is not suited to operate within the saturated region, where liquid droplets might be present, special considerations need to be taken at this point. Some fluids with complex molecules have the dew line that has a positive slope in the temperature - entropy diagram namely:

$$\left(\frac{\delta T}{\delta s}\right)_{\mathrm{sat,v}} > 0. \tag{3.18}$$

These fluids are considered 'wet fluids' in VCS applications as the compression process starting from a superheated vapour can end up back in saturated conditions. If, for the given system specifications, a fluid is saturated after compression, it is discarded from the selection. An example of a fluid that falls under this category is Novec649 and an exemplary T-s diagram highlighting this case is given in Figure 3.3.

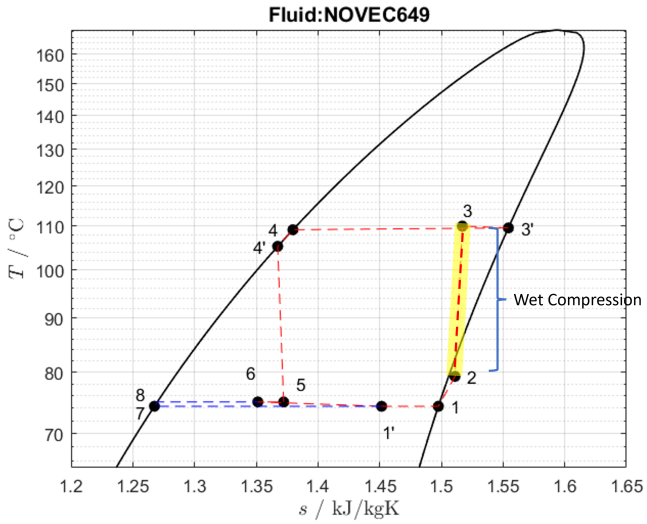


Figure 3.3: Example of fluid with positive $\left(\frac{\delta T}{\delta s}\right)_{\text{sat,v}}$ slope and compression ending in saturated conditions.

After the compressor, the vapour is desuperheated and arrives at saturation conditions in station 3' resulting in $x_{\text{vq3}'} = 1$. A pressure drop of 1% is imposed on the desuperheating process.

$$\begin{aligned} p_{3'} &= p_3 \cdot 0.99 \\ h_{3'} &= h(p_{3'}, x_{\text{vq3}'}) \end{aligned} \tag{3.19}$$

The saturated vapour is then condensed in the condenser leaving in saturated liquid conditions ($x_{\text{vq4}} = 0$) at station 4. Also here a pressure drop of 1% is imposed resulting in a total pressure drop of 2% over the heat rejection process.

$$\begin{aligned} p_4 &= p_{3'} \cdot 0.99 \\ h_4 &= h(p_4, x_{\text{vq4}}) \end{aligned} \tag{3.20}$$

The thermal energy used to superheat the vapour at the compressor inlet is now taken from the saturated liquid at the condenser outlet. This is done through the means of an internal heat exchanger that helps ensuring both subcooled conditions before the valve (station 4') and superheated conditions at the compressor inlet.

$$\begin{aligned} h_{4'} &= h_4 - (h_2 - h_1) \\ p_{4'} &= p_4 \end{aligned} \tag{3.21}$$

The valve is modelled as an isoenthalpic expansion process bringing the fluid back to the saturation conditions at the fuel cell cooling channels inlet.

$$\begin{aligned} h_5 &= h_{4'} \\ p_5 &= p_{\text{sat}}(T_{\text{evap}}) \end{aligned} \tag{3.22}$$

Here the fluid is mixed with the liquid that was initially separated at the cooling channels outlet. This part of the cycle, which is a recirculation of un-evaporated fluid, starts at station 7 after the two phases have been separated. Here the fluid is in saturated liquid conditions with $x_{\text{vq7}} = 1$.

$$\begin{aligned} p_7 &= p_{1'} \\ h_7 &= h(p_7, x_{\text{vq7}}) \end{aligned} \tag{3.23}$$

After separation the saturated liquid is pumped to a higher pressure in order to overcome the pressure drop encountered over the cooling channels. The pump is modeled with an isentropic efficiency of $\eta_{\text{pump}} = 0.75$ and the calculation procedure for state 8 is identical to the calculation procedure for the compressor.

$$\begin{aligned} h_8 &= \frac{h_{8s} - h_7}{\eta_{\text{pump}}} + h_7 \\ p_8 &= p_{\text{sat}}(T_{\text{evap}}) \\ h_{s8} &= h(p_8, s_7) \end{aligned} \tag{3.24}$$

The state at station 6, after mixing of the recirculated and flashed coolant, can be found knowing the vapour quality after the evaporation process which determines the mass ratio of coolant that is separated.

$$\begin{aligned} h_6 &= x_{\text{vq1}'} \cdot h_5 + (1 - x_{\text{vq1}'}) \cdot h_8 \\ p_6 &= p_{\text{sat}}(T_{\text{evap}}) \end{aligned} \tag{3.25}$$

After all the states in the cooling cycle are defined the COP can be calculated through the thermal energy absorbed during evaporation,

$$h_{\text{evap}} = h_{1'} - h_6, \tag{3.26}$$

and the mechanical energy used by the compressor and pump,

$$\begin{aligned} w_{\text{comp}} &= (h_3 - h_2), \\ w_{\text{pump}} &= (h_8 - h_7). \end{aligned} \tag{3.27}$$

Specific quantities can be used here as the thermodynamic states in the cycle are not cooling power dependent. Only the mass flow rate of the coolant needs to be adjusted in order to scale the system cooling power. This results in the definition of COP as in

$$\text{COP} = \frac{\Delta h_{\text{evap}}}{x_{\text{vq1}'} \cdot \Delta h_{\text{comp}} + (1 - x_{\text{vq1}'}) \cdot \Delta h_{\text{pump}}}. \tag{3.28}$$

### 3.1.2. COMPATIBLE FLUIDS

Based on the constraints of operating temperature and pressure, a total of 33 potential fluids from the REFPROP database are feasible. The fluids presented in Figure 3.4 are selected for PMP systems but only meet the quantitative requirements. Additionally, the results of the COP evaluation with a saturation temperature in the condenser of 110°C and of 75°C in the fuel cell is presented in Table 3.1.

Methanol is the best-performing fluid for the PMP system and places third for VCS with only a slight difference to R150 and ethanol in terms of COP. The available temperature range between 1 and 5 bar is larger than ethanol and R150. Methanol is slightly toxic and flammable. This might pose a practical limitation but, given that flammable fluids are already present on an aircraft, and the potential shown is high, it should be further considered. The best non-flammable, non-toxic fluid with both zero ODP and low GWP is R1233ZDE (trans-1-Chloro-3,3,3-trifluoropropene). Its performance is low compared to methanol but its characteristics make it an easier fluid to handle in practical applications.

The saturation pressure of methanol and R1233ZDE is 0.13 and 1.08 bar respectively. This poses a limitation to the shutdown conditions of a two-phase system cooling system for methanol as sub-atmospheric pressures would be present as explained in section 3.10.

Methanol and R1233ZDE are chosen as fluids to further investigate their applicability to fuel cell systems. Despite the limitation of both fluids, they belong to two very different fluid categories and are thus prime candidates to highlight the effects of fluid family on cooling system design.

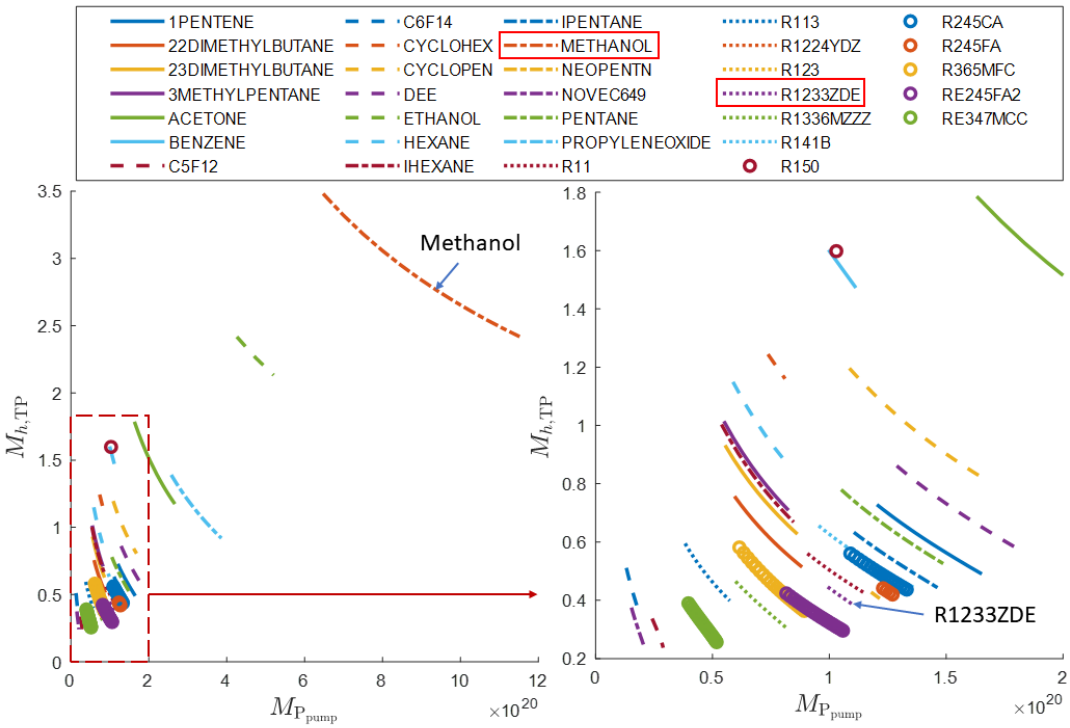


Figure 3.4: Figures of merit for pump power and heat transfer coefficient of compatible fluids for fuel cell PMP cooling systems.

## 3.2. FUEL CELL THERMAL MODEL

As shown in chapter 2 the processes inside a PEM fuel cell are many and involve chemical, electrical, mass transport and heat transfer processes. As this research is mainly focused on the design and modelling of a cooling system for fuel cell application only the relevant heat transfer processes are considered. Furthermore, from a system-level perspective, only the coolant stream is of relevance to the modelling of a cooling system, thus the rest of the balance of plant (hydrogen storage and supply, air supply, electronics) is neglected.

### 3.2.1. ASSUMPTIONS AND SIMPLIFICATIONS

The first simplification is that the electrochemical processes are not modelled. The underlying assumption is that the effect of the electrochemical processes can be described only by the operational cell voltage $V_{\mathrm{op}}$ and current density $i_{\mathrm{op}}$. The relationship between these two values is given by the polarization curve which is dependent on many operational variables and is characteristic for one specific type of MEA construction. All this complexity can be eliminated if the operating voltage and current density of a specified fuel cell stack are known.

Additionally, it is assumed that the reaction is happening in a uniformly distributed way over the entire active area of the membrane. This assumption is known not to be correct as the current density can vary over the area of the membrane [73] but it is deemed acceptable as the operating voltage and current density are an average over the membrane area and are relevant from a system level perspective. This assumption simplifies the thermal modelling as the thermal energy released per unit area by the reaction can be expressed by a single variable $q_{\mathrm{cell}}$ which is constant over the entire active membrane area.

To simplify the energy balance of the fuel cell stack it is assumed that no thermal energy transfer occurs to the environment through radiation, conduction or free convection. Only the thermal energy transfer through forced convection or flow boiling to the coolant is taken into account. Additionally, the sensible enthalpy change of the reactants is neglected and only the latent enthalpy needed to evaporate the produced liquid water is taken into account. On one hand, this assumption is conservative as the air increases its temperature and thus convects thermal energy away from the cell. As this is only a few percent with respect to the thermal energy transferred to the coolant it is omitted. On the other hand, the assumption that all the produced water

Table 3.1: Fluids compatible with VCS systems for fuel cell cooling applications and their respective performance parameters and characteristics.

| Fluid | $T_{min}$ °C | $T_{max}$ °C | $COP$ - | $p_{cond}$ bar | $PR$ - | GWP | ODP | toxic | flammable |
|---|---|---|---|---|---|---|---|---|---|
| R150 | 83.1 | 85.0 | 6.71 | 2.18 | 2.83 | - | - | yes | yes |
| ETHANOL | 78.1 | 85.0 | 6.70 | 3.13 | 3.54 | - | - | no | yes |
| METHANOL | 64.1 | 85.0 | 6.66 | 4.80 | 3.18 | moderate | - | low | yes |
| BENZENE | 79.6 | 85.0 | 6.60 | 2.34 | 2.71 | - | - | yes | yes |
| ACETONE | 60.0 | 85.0 | 6.55 | 4.78 | 2.57 | low | - | low | yes |
| CYCLOHEX | 80.3 | 85.0 | 6.42 | 2.26 | 2.66 | - | - | yes | yes |
| PROPYLENEOXIDE | 60.0 | 85.0 | 6.41 | 8.67 | 2.36 | - | - | yes | yes |
| CYCLOPEN | 60.0 | 85.0 | 6.38 | 5.24 | 2.38 | - | - | yes | yes |
| R141B | 60.0 | 85.0 | 6.24 | 8.41 | 2.27 | high | low | low | no |
| R11 | 60.0 | 78.1 | 6.24 | 10.15 | 2.19 | high | moderate | low | no |
| R113 | 60.0 | 85.0 | 6.13 | 5.49 | 2.37 | high | moderate | low | no |
| R123 | 60.0 | 80.9 | 6.01 | 9.76 | 2.27 | high | low | low | no |
| DEE | 60.0 | 85.0 | 5.95 | 8.17 | 2.32 | - | - | no | yes |
| 1PENTENE | 60.0 | 85.0 | 5.94 | 8.58 | 2.23 | - | - | no | yes |
| R245CA | 60.0 | 75.0 | 5.80 | 11.64 | 2.32 | high | no | low | no |
| R1233ZDE | 60.0 | 69.1 | 5.78 | 12.88 | 2.22 | low | no | low | no |
| R1224YDZ | 60.0 | 64.7 | 5.53 | 14.32 | 2.20 | low | no | low | no |
| R245FA | 60.0 | 62.8 | 5.52 | 15.71 | 2.26 | high | no | low | no |

is evaporated is not always valid as the air stream in the fuel cell may be saturated with water vapour and not all the liquid water can be evaporated. The implemented fuel cell model has no means of simulating this phenomenon in more detail but the assumption is supported by literature [22, 23].

### 3.2.2. COOLING PLATE GEOMETRY AND THERMAL LOADS

The cooling channels in a fuel cell are embedded in the bipolar plate (see Figure 2.2 and Figure 3.5). These plates can be metallic or made out of graphite and the channels are typically of rectangular cross section. Many different cooling channel configurations have been researched with more complex configurations showing better temperature uniformity over the membrane and more simple geometries showing less pressure drop [74]. For sake of simplicity, the parallel channel configuration is implemented in this model.

If the fuel cell stack power and voltage are defined from the required application the active membrane area can be found. First, the stack current is calculated with

$$I_{stack} = \frac{P_{stack}}{V_{stack}}, \tag{3.29}$$

then, as the cells are connected in series in a fuel cell stack ($I_{cell} = I_{stack}$)the cell current is known and the membrane active area is found with

$$A_{cell} = \frac{I_{cell}}{i_{op}}. \tag{3.30}$$

Here the operational current density is intended as design current density as the model does not currently include off-design simulations.

Given the operational cell voltage and current density, the thermal energy release per unit cell area is calculated. First, the area-specific power of the cell is calculated with

$$P''_{cell} = i_{op} \cdot V_{op}, \tag{3.31}$$

then, the heat flux due to the reaction is

$$q_{react} = P''_{cell}\left(\frac{1}{\eta_{cell}} - 1\right). \tag{3.32}$$

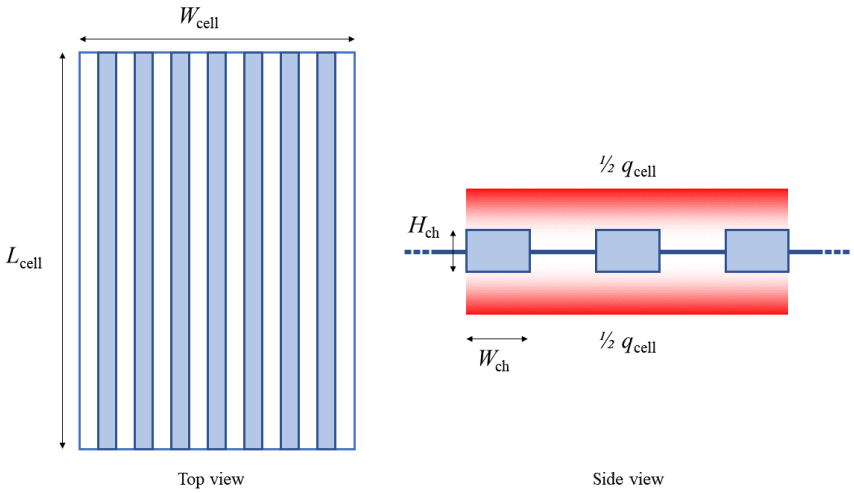


Figure 3.5: Fuel cell cooling channel geometry.

To this, the thermal energy absorbed by the evaporation of the produced liquid water should be removed. The latent heat of evaporation of water is, depending on conditions, approximately 40.7kJ mol$^{-1}$ and the absorbed heat flux thus

$$q_{\text{H2Oevap}} = \frac{i_{\text{op}}}{2F} \cdot h_{\text{H2Oevap}}. \tag{3.33}$$

Finally, the heat flux that needs to be convected by the cooling system is

$$q_{\text{cell}} = q_{\text{react}} - q_{\text{H2Oevap}}. \tag{3.34}$$

The total thermal energy that needs to be rejected by the cooling system per fuel cell stack can be found by multiplying the cell area by the heat flux and the number of cells in a stack. The latter is found with

$$N_{\text{cell}} = \frac{V_{\text{stack}}}{V_{\text{op}}}, \tag{3.35}$$

and the former with

$$\dot{Q}_{\text{stack}} = q_{\text{cell}} \cdot A_{\text{cell}} \cdot N_{\text{cell}}. \tag{3.36}$$

To characterize the forced convective heat transfer in a rectangular duct the duct geometry parameters are needed. A schematic representation of the cooling channel geometry is given in Figure 3.5. First, the active cell dimensions to be cooled can be calculated by imposing a cell aspect ratio $\Lambda_{\text{cell}}$ with

$$W_{\text{cell}} = \sqrt{\frac{A_{\text{cell}}}{\Lambda_{\text{cell}}}}, \tag{3.37}$$

$$L_{\text{cell}} = \frac{A_{\text{cell}}}{W_{\text{cell}}}. \tag{3.38}$$

The aspect ratio is a free parameter that influences the length and the number of cooling channels per cell. The cooling ducts are distributed uniformly over the membrane with uniform spacing equal to their width. The number of cooling channels per cell is thus

$$N_{\text{ch}} = \frac{W_{\text{cell}}}{2W_{\text{ch}}}, \tag{3.39}$$

and their length is equal to the cell length ($L_{\text{ch}} = L_{\text{cell}}$).

The channel width and height are parameters to be chosen and both typically vary between 4 and 0.5 mm [22]. From these two parameters, the important hydraulic diameter and cross-sectional area can be calculated with

$$D_h = \frac{2 \cdot W_{\text{ch}} H_{\text{ch}}}{H_{\text{ch}} + W_{\text{ch}}}, \quad \text{and} \tag{3.40}$$

$$A_{\text{ch}} = H_{\text{ch}} \cdot W_{\text{ch}} \tag{3.41}$$

respectively.

Finally, the heat flux on the channel walls can be calculated by first finding the channel wall surface area with

$$A_{\text{walls}} = L_{\text{ch}} \cdot (2W_{\text{ch}} + 2H_{\text{ch}}), \tag{3.42}$$

and the heat flux at the walls with

$$q_{\text{walls}} = \frac{q_{\text{cell}} A_{\text{cell}}}{N_{\text{ch}} A_{\text{walls}}}. \tag{3.43}$$

The overall channel heat transfer rate is then

$$\dot{Q}_{\text{ch}} = q_{\text{walls}} \cdot A_{\text{walls}} \tag{3.44}$$

### 3.2.3. SINGLE PHASE COOLING

In the case of single-phase liquid cooling, the coolant mass flow rate can be determined if a requirement on the maximum temperature difference $\Delta T$ between inlet and outlet is imposed. Per channel, the mass flow rate can be calculated knowing the heat capacity of the coolant $c$ with

$$\dot{m} = \frac{\dot{Q}_{\text{ch}}}{\Delta T \cdot c}. \tag{3.45}$$

#### HEAT TRANSFER COEFFICIENT

The heat transfer coefficient of the coolant flowing in the cooling channels can be calculated using correlations available in literature. Laminar flows are mostly expected in fuel cells but for completeness, the correlations used also include turbulent regimes. The combination of heat transfer correlations by Petukhov [75]

$$h_{\text{c}} = \frac{Re\,Pr(f/2)(k/D_h)}{1 + 12.7\left(Pr^{2/3} - 1\right)(f/2)^{0.5}} \qquad \text{for } 10^4 \leq Re \leq 5 \cdot 10^6, \tag{3.46}$$

and Gnielinski [76]

$$h_{\text{c}} = \frac{(Re - 1000)\,Pr(f/2)\,(k/D_h)}{1 + 12.7\left(Pr^{2/3} - 1\right)(f/2)^{0.5}} \qquad \text{for } 3000 \leq Re \leq 10^4 \tag{3.47}$$

are proposed by Kandlikar and Balasubramanian [71] for the turbulent regime. The Reynolds and Prandtl numbers are defined as

$$Re = \frac{G D_h}{\mu}, \quad \text{and} \tag{3.48}$$

$$Pr = \frac{c_p \mu}{k} \tag{3.49}$$

respectively, with $G$ being the mass flux over the channel cross-sectional area, $\mu$ the dynamic viscosity and $k$ the thermal conductivity.

In the laminar regime, the Nusselt number $Nu_{\text{lam}}$ can be used. In a circular duct, it is a constant over the whole laminar regime but in a rectangular duct, it is dependent on both the aspect ratio of the channel as well as the thermal boundary conditions (QBC) [77] as in

$$Nu_{\text{lam}} = \frac{h_{\text{c}} D_h}{k} = f(\Lambda_{\text{ch}}, \text{QBC}). \tag{3.50}$$

The thermal boundary conditions for the laminar convection in fuel cell applications can be of the H1 and H2 types [72]. Both have a constant axial heat flux along the channel length but vary in the heat flux over the channel perimeter. The H1 condition is for a constant circumferential temperature and the H2 condition is for a constant circumferential heat flux. The results of two numerical studies [73, 78] indicate that the H1 condition is more appropriate as the materials used in fuel cell bipolar plates are good heat conductors and ensure temperature uniformity over the whole cooling channel circumference. Additionally, the number of heated channel sides can have an impact on the heat transfer coefficient. The same studies by Afshari find a higher $Nu_{\text{lam}}$ than a channel heated on all four sides would suggest. The value of $Nu_{\text{lam}} = 4.92$ of Ref [78] falls between 4.12 and 5.2 which are for a 4-side heated channel and a 2 opposite sides heated channel respectively. This is expected as the heat flux from the membranes is primarily from the top and bottom surface, nevertheless, the more conservative 4-side heated channel $Nu_{\text{lam}}$ is used in this model. Tabulated values of $Nu_{\text{lam}}$ with dependency on aspect ratio are given in Ref. [77].

The axial conduction of heat through the channel walls is neglected in the present work. Davis & Gill define a parameter $\beta$ that serves to evaluate the importance of axial wall conduction in forced laminar convection in ducts. It is defined as

$$\beta = \frac{k_{\text{wall}} D_h}{k_{\text{fluid}} L_{\text{ch}}}. \tag{3.51}$$

When $\beta << 1$, the axial conductivity can be neglected. The material of the bipolar plates in fuel cells can be either carbon-based (graphite) or metallic. Metals employed are usually stainless steel or titanium alloys [79]. The thermal conductivity of a graphite bipolar plate was given in Ref. [73] to be 24 $\text{Wm}^{-1}\,\text{K}$. Stainless steel and titanium have similar thermal conductivity, both around 15 $\text{Wm}^{-1}\,\text{K}$.

In the transition region a linear interpolation between the turbulent and laminar heat transfer coefficient at $Re = 3000$ and $Re = 1600$ respectively.

The local temperature difference between the flow bulk temperature and the coolant channel wall can be calculated with

$$\Delta T_{\text{wall}} = \frac{q_{\text{ch}}}{h_{\text{c}}}. \tag{3.52}$$

### PRESSURE DROP

The pressure drop due to frictional forces in the cooling channels can be calculated with

$$\Delta p_{\text{ch}} = \frac{2 f G^2 L_{\text{ch}}}{D_h \rho}. \tag{3.53}$$

The fanning friction factor $f$ needs to be evaluated for laminar flow in rectangular ducts. It is dependent on the duct aspect ratio and the Reynolds number and independent of surface roughness. The function

$$f_{\text{lam}} = 24(1 - 1.3553\,\Lambda_{\text{ch}} + 1.9467\,\Lambda_{\text{ch}}^2 - 1.7012\,\Lambda_{\text{ch}}^3 + 0.9564\,\Lambda_{\text{ch}}^4 - 0.2537\,\Lambda_{\text{ch}}^5) Re^{-1} \tag{3.54}$$

is presented in Ref. [77].

### VERIFICATION

The correlations for single-phase liquid cooling have been verified and validated with the numerical work of Afshari *et al.* [78]. A fuel cell bipolar plate of 150 x 150 mm has been modelled with water as coolant. The relevant boundary conditions together with the comparison results are given in Table 3.2. It should be noted that in Ref. [78] the Darcy friction factor is used rather than the Fanning friction, which differs only by a factor of 4 ($f_D = 4 \cdot f$). The difference in the results can be attributed to two main factors. The first factor is the thermal boundary condition. The H1 4-side and 2 opposite sides QBCs are representing only ideal edge cases that do not appear so perfectly in reality. In the case of fuel cell cooling channels, as the one simulated in Ref. [78], the QBC is a combination of both and the resulting $Nu$ falls in between these two values ($Nu$ relative to the H1 2 opposite sides QBC is in parentheses in the table). The second aspect is that in the reference work, a uniform inlet velocity distribution is assumed. This causes the friction factor to be higher in a developing laminar boundary layer resulting in a higher pressure drop over the channel. In a real application, It is difficult to say with certainty what the status of the boundary layer is at the inlet. Pipes, manifolds, obstructions and distribution elements can both disrupt the boundary layer or promote the formation of a new one.

Table 3.2: Comparison of single phase cooling model with Ref. [78]

| Parameters | Ref. [78] |
|---|---|
| $Re$ | 330 |
| $\Lambda_{\text{ch}}$ | 0.5 |
| $L_{\text{ch}}$ | 150 mm |
| $D_h$ | 1.33 mm |
| $\dot{V}$ | 6e-6 $\text{m}^3\,\text{s}^{-1}$ |

| Results | Ref. [78] | Present Work |
|---|---|---|
| $f_D \cdot Re$ | 61 | 62.23 |
| $Nu$ | 4.93 | 4.12 (5.22) |
| $\Delta p$ | 285 Pa | 274.3 Pa |

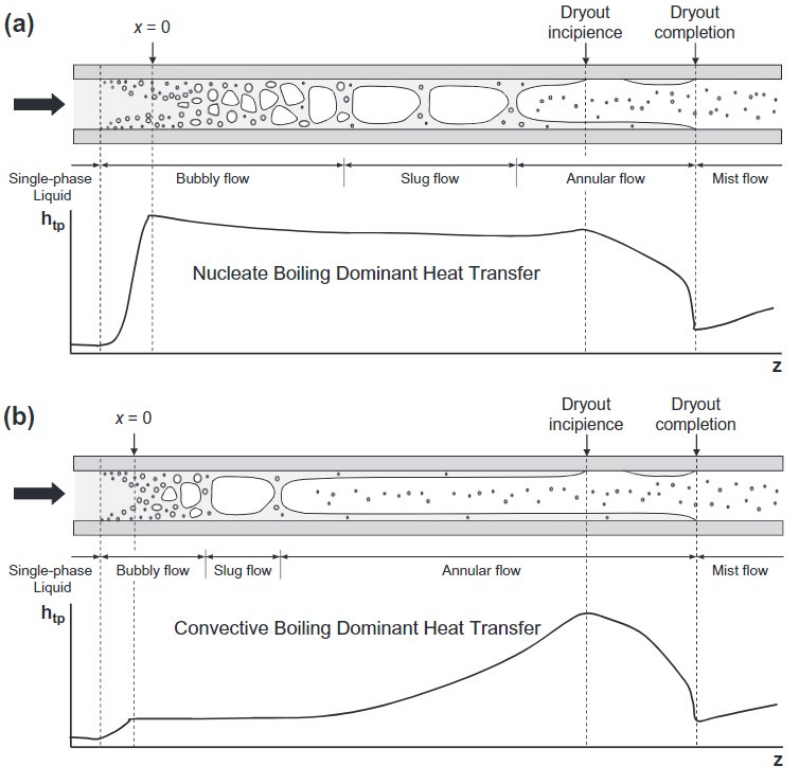


Figure 3.6: Boiling flow regimes and heat transfer coefficient trends reproduced from Ref. [80]. a) Nucleate Boiling b) Convective Boiling.

### 3.2.4. TWO PHASE COOLING

When cooling a fuel cell by means of a boiling flow the mass flow requirements are bound to the latent heat of evaporation of the chosen fluid. In an ideal condition, all the fluid entering the cooling channels is evaporated. This is not possible in practice if the heat transfer coefficient inside the channel needs to remain high throughout the evaporation process. In fact, the highest heat transfer coefficients during flow boiling are achieved when a thin film of fluid covers the channel walls and evaporates progressively. At high vapour qualities, this film breaks down and the channel walls are exposed to the vapour phase directly. This phenomenon is called dry-out and coincides with a strong reduction in the heat transfer coefficient. Thus a limiting vapour quality exists after which the thin liquid film becomes unstable and high-temperature hot spots might arise along the cooling channel walls. To include this in the determination of the coolant mass flow, the evaporation enthalpy can be multiplied by the limiting vapour quality. Additionally, the vapour quality at the channel entrance can be subtracted resulting in

$$\dot{m} = \frac{\dot{Q}_{\text{ch}}}{h_{\text{lv}}\left(x_{\text{vq}_{\text{out}}} - x_{\text{vq}_{\text{in}}}\right)}. \tag{3.55}$$

### FLOW BOILING HEAT TRANSFER COEFFICIENT

The boiling heat transfer coefficient correlation used was initially developed by Kandlikar [47] and then updated to include laminar flow in mini- and microchannels [71]. A typical trend in heat transfer coefficient for boiling flow is depicted in Figure 3.6. The correlation is based on the liquid-only heat transfer coefficient which is then enhanced through a factor dependent on both the boiling and convection numbers. They are defined as

$$Bo = \frac{q_{ch}}{G\, h_{lv}}, \quad \text{and} \tag{3.56}$$

$$Co = \left(\frac{\rho_v}{\rho_l}\right)^{0.5} \left(\frac{1 - x_{vq}}{x_{vq}}\right)^{0.8} \tag{3.57}$$

respectively. Two heat transfer coefficients are calculated with the correlation. One for the nucleate boiling-dominated region and one for the convective boiling-dominated region as in

$$\begin{aligned} h_{TP,NBD} &= 0.6683 Co^{-0.2} (1 - x_{vq})^{0.8} h_{c,LO} + 1058.0 Bo^{0.7} (1 - x_{vq})^{0.8} F_{Fl} h_{c,LO}, \\ h_{TP,CBD} &= 1.136 Co^{-0.9} (1 - x_{vq})^{0.8} h_{c,LO} + 667.2 Bo^{0.7} (1 - x_{vq})^{0.8} F_{Fl} h_{c,LO}, \\ h_{TP} &= max\left(h_{TP,NBD}, h_{TP,CBD}\right). \end{aligned} \tag{3.58}$$

The higher value of the two is used and the transition between the nucleate boiling and convection boiling region is marked by the intersection of the two functions. The liquid-only heat transfer coefficient ($h_{c,LO}$) is calculated with the methods in subsection 3.2.3 and the parameter $F_{Fl}$ is a fluid-surface specific parameter that is recommended to be set at 1 for surface-fluid combinations that have not yet been researched or in general for preliminary analysis. This correlation is valid for Reynolds numbers up to 3000 and down to 100. Below $Re$ 100 only the nucleate boiling term is used as convection boiling is suppressed.

The use of the correlation by Kandlikar and Balasubramanian [71], Equation 3.58, is recommended in Ref. [53]. The correlation is subjected to many studies of its performance and results strongly depend on the specific application in question [81–83]. No best overall correlation is found in literature that can cover many fluids and flow conditions. Thus, the effect of uncertainties and correlation errors (commonly up to 50%) needs to be studied.

### ONSET OF NUCLEATE BOILING AND DRY OUT INCIPIENCE

If the coolant enters the cooling channels in the sub-cooled state, bubble nucleation will occur at the wall before the bulk flow reaches saturation conditions. This effect is called sub-cooled flow boiling and it is important to estimate the onset of nucleate boiling (ONB) in these conditions in order to verify if a certain cooling concept is compatible with flow boiling. If the liquid is not boiling for a long distance along the channel the lower heat transfer coefficient might lead to hot spots in the fuel cell membrane.

The ONB can be calculated with a method first proposed by Hsu [84] and presented in Refs. [72, 85]. The method relies on the fact that a bubble needs to have an internal pressure which is high enough to sustain the force given by the surface tension $\sigma$ at the vapour-liquid interface. Assuming the internal temperature of a bubble residing in a cavity at the wall surface is equal to the wall temperature, the wall temperature needed to generate an internal pressure great enough to sustain the bubble can be found. The temperature and pressure inside the bubble are related to one another through the saturation conditions of the fluid. The method expresses the wall superheat as the temperature difference of the wall to the saturation temperature of the fluid at the local pressure as in

$$\Delta T_{Sat} = T_{wall} - T_{sat}. \tag{3.59}$$

The wall superheat $\Delta T_{Sat,ONB}$ at which bubble nucleation occurs is calculated with

$$\Delta T_{Sat,ONB} = \sqrt{\frac{8.8 \sigma T_{Sat} q_{ch}}{\rho_v h_{lv} k_l}}. \tag{3.60}$$

From the definition of heat transfer coefficient and the wall-to-bulk flow temperature difference in Equation 3.52 the degree of sub-cooling can be found with

$$\Delta T_{Sub,ONB} = \frac{q_{ch}}{h_c} - \Delta T_{Sat,ONB}, \tag{3.61}$$

where $h_c$ is the local convective heat transfer coefficient. If the liquid coolant enters the cooling channel with a subcooling degree higher than the one given by $\Delta T_{\text{Sub,ONB}}$, the mechanism for heat transfer is single phase convection only. Thus, to ensure that the high heat transfer coefficients of flow boiling are maintained also at the channel inlet, the coolant cannot enter with a degree of subcooling higher than $\Delta T_{\text{Sub,ONB}}$.

At the outlet of the channel, dry-out may occur. The correlation developed by Kim and Mudawar [80] to predict the vapour quality at dry-out incipience (DI) is

$$x_{\text{vq,DI}} = 1.4 We_{\text{LO}}^{0.03} p_{\text{R}}^{0.08} - 15.0\, Bo^{0.15} Ca^{0.35} \left(\frac{\rho_{\text{v}}}{\rho_{\text{l}}}\right)^{0.06}, \tag{3.62}$$

where the liquid-only Weber number , Capillary number and reduced pressure are defined as

$$We_{\text{LO}} = \frac{G^2 D_h}{\rho_{\text{l}} \sigma}, \tag{3.63}$$

$$Ca = \frac{\mu_{\text{l}} G}{\rho_{\text{l}} \sigma} = \frac{We_{\text{LO}}}{Re_{\text{LO}}}, \quad \text{and} \tag{3.64}$$

$$p_{\text{R}} = \frac{p}{p_{\text{crit}}} \tag{3.65}$$

respectively. When the vapour quality at dry-out incipience is reached, the liquid film covering the channel walls breaks down and the walls are exposed directly to the vapour phase. This induces a rapid reduction in heat transfer coefficient as the boiling of the thin liquid film through convection with the vapour phase cannot happen anymore. The vapour quality at dry-out incipience is a design constraint that has to be carefully taken into account.

### TWO PHASE PRESSURE DROP

The pressure drop in a two-phase flow can be estimated using the correlation developed by Friedel [86] and presented in [87]. This correlation has also been used in the in-house developed thermal management system library of the Aerospace Power & Propulsion Group at TU Delft and has thus been verified and validated extensively in previous work like Ref. [67].

The Friedel Correlation consists in modifying the liquid-only pressure gradient with a two-phase multiplier as in

$$\left(\frac{\Delta p_f}{L_{\text{ch}}}\right)_{TP} = \phi_{LO}^2 \left(\frac{\Delta p_f}{L}\right)_{LO}, \tag{3.66}$$

where $\phi_{LO}^2$ is the two-phase multiplier and $\left(\Delta p_f / L\right)_{LO}$ is the negative pressure gradient due to friction for total flow as a liquid.

The two-phase multiplier is calculated with

$$\phi_{LO}^2 = E + \frac{3.24 FH}{Fr^{0.045} We^{0.035}}, \tag{3.67}$$

where

$$\begin{aligned}
E &= (1 - x_{\text{vq}})^2 + x_{\text{vq}}^2 \left(f_{VO} / f_{LO}\right) \left(\rho_{\text{l}} / \rho_{\text{v}}\right), \\
F &= x_{\text{vq}}^{0.78} (1 - x_{\text{vq}})^{0.24}, \\
H &= \left(\rho_{\text{l}} / \rho_{\text{v}}\right)^{0.91} \left(\mu_{\text{v}} / \mu_{\text{l}}\right)^{0.19} \left(1 - \mu_{\text{v}} / \mu_{\text{l}}\right)^{0.7}, \\
Fr &= \frac{G^2}{g D_h \rho_{\text{TP}}^2} = \text{ Froude number }, \\
We &= \frac{G^2 D_h}{\rho_{\text{TP}} \sigma} = \text{ Weber number }, \\
\rho_{\text{TP}} &= \left[x_{\text{vq}} / \rho_{\text{v}} + (1 - x_{\text{vq}}) / \rho_{\text{L}}\right]^{-1}.
\end{aligned} \tag{3.68}$$

The parameters $E$ and $F$ ensure that the correlation gives correct results for liquid-only and vapour-only flow at $x_{\text{vq}} = 0$ and $x_{\text{vq}} = 1$ respectively.

As for the heat transfer coefficient correlation, also the pressure drop correlation suffers from large uncertainties as found in Refs. [82, 88] and the effects need to be investigated.

Table 3.3: Verification results of two-phase heat transfer coefficient and pressure drop correlations with Echterm. Fluid: Methanol.

| Parameters | Present Work |
|---|---|
| $T_{sat}$ | 80 °C |
| $G$ | 25 $kg s^{-1} m^{-2}$ |
| $q_{ch}$ | 4278 $W m^{-2}$ |
| $D_h$ | 0.75 mm |
| $x_{vq}$ | 0.35 |

| Results | Echterm | Present Work |
|---|---|---|
| $h_{TP}$ | 2261 $W m^{-1} K^{-1}$ | 2200 $W m^{-1} K^{-1}$ |
| $\Delta P/\Delta L$ | 49736 $Pa m^{-1}$ | 48475 $Pa m^{-1}$ |

#### VERIFICATION

The verification of the two-phase heat transfer correlation by Kandlikar has been manually verified through the reproduction of the exercises given in Ref. [72] by the same author. Additionally, the commercial software Echterm by Greth[1] is used as a further verification tool. The channel geometry used for verification is the same used for the 1D analysis of the cooling channel and is given in Table 3.3. The operating conditions and saturation temperature of the fluid, methanol, are also identical to the ones observed in the test case. Theboth two-phase heat transfer coefficient and frictional pressure drop correlation show good agreement with the commercially validated software with errors of only -2.7% and -2.5% respectively.

### 3.2.5. CONSTRAINTS FROM WATER MANAGEMENT

Apart from keeping the temperature of the cooling plate and membrane low and uniform, fuel cell cooling has also a strong effect on water management and overall performance. Researchers have shown that a temperature gradient along the cell can improve the water distribution in the membrane and increase efficiency and power density [41, 89]. This can be explained by the interaction of the coolant, air and water produced at the cathode.

The membrane of a LT-PEM fuel cell needs to be hydrated in order to become conductive to protons. This requires that the air at the fuel cell is humidified such that it can not dry out the membrane by evaporating too much of the contained water. Usual relative humidity at air inlet can vary from 60% to 100% [22] depending on the fuel cell stack construction and materials. While the air is not saturated with water vapour the produced liquid water can be evaporated. This is particularly beneficial in reducing the cooling requirement of the fuel cell stack. Once a relative humidity of 100% is reached the produced water remains liquid and accumulates in the membrane and GDL and is partially removed by the airflow passing through the cathode. If the temperature of the air does not increase, the saturation conditions are reached before the outlet of the cathode flow path and flooding of the stack due to too much liquid water can occur. To avoid this the air can be heated. As the saturation pressure of the water vapour increases with temperature more water can be evaporated and absorbed by the air.

A relation between the inlet conditions and ideal outlet conditions of cathode air can be set up in order to find the required temperature increase.

The inlet molar ratio of vapour in air can be found according to Equation 2.17. At the outlet for the cathode, the molar ratio depends on the water present at the inlet and the stoichiometry of the air fed to the fuel cell as in

$$\chi_{out} = \frac{\chi_{in}\lambda_{O2}/r_{O2} + 2}{\lambda_{O2}/r_{O2} - 1}, \tag{3.69}$$

where $\lambda_{O2}$ is the stoichiometry and $r_{O2}$ the molar percentage of oxygen in air, typically 21%.

To avoid flooding the outlet relative humidity is at a maximum 100% and the corresponding saturation pressure can be calculated with

$$p_{vs,out} = \frac{\chi_{out} p_{out}}{1 + \chi_{out}}. \tag{3.70}$$

The corresponding saturation temperature can be found using REFPROP or CoolProp and the outlet temperature of the air is known.

Figure 3.7 shows how the inlet conditions affect the required temperature increase. For operation above 60°C and pressurized operation above 1.5 bar the temperature increase is in the range of 10 K.

[1] https://greth.fr/echtherm/

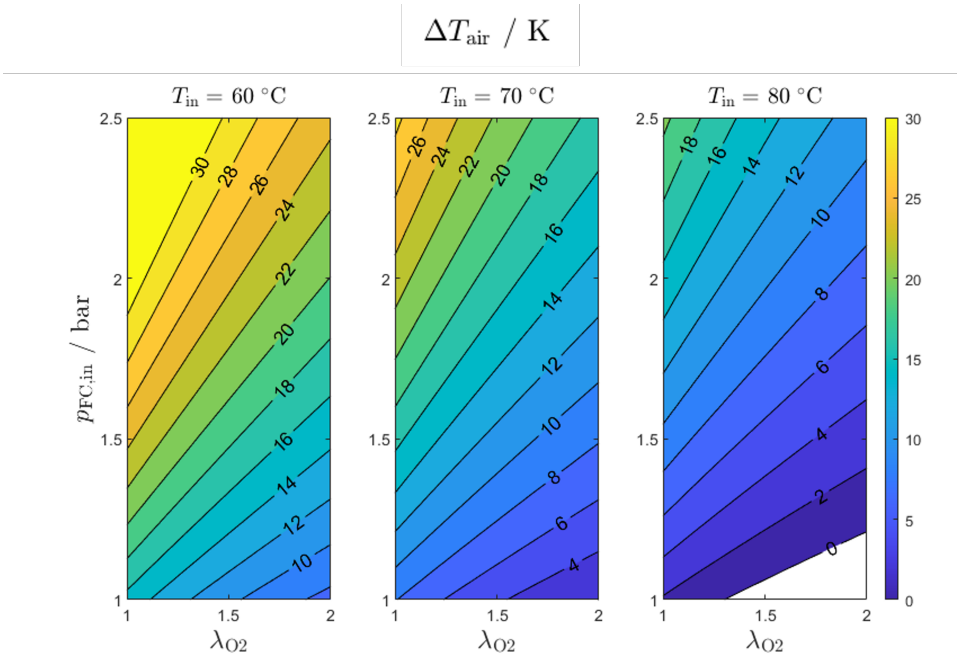


Figure 3.7: Temperature increase of air in cathode for 100% relative humidity at outlet. Evaluated with $\varphi_{FC,in} = 0.8$.

As the air passes inside the bipolar plate in close contact with the MEA it follows the same temperature profile of the MEA from inlet to outlet. The temperature of the MEA is regulated by the coolant. As the coolant has twice the contact area with the MEA than the air stream (see Figure 2.2) and although the separation through the bipolar plate adds resistance to the thermal path from MEA to coolant it can be argued that the coolant is the flow dominating the heat transfer. In fact, water has a thermal conductivity which is more than 20 times higher than air (667 $mW m^{-1} K^{-1}$ vs 30 $mW m^{-1} K^{-1}$ respectively) which is the key factor in determining the heat transfer coefficient in laminar flow as the Nusselt number is constant. Thus, the temperature difference of coolant inlet to outlet used to determine the coolant mass flow rate according to Equation 3.45 can be imposed from the water management requirements. For this work, 10K are used as reference but the exact $\Delta T$ should be determined either through detailed 3D simulation of the fuel cell or through experimental procedures.

It is clear that for a single-phase coolant that absorbs thermal energy through a change in sensible enthalpy, the relation between $\Delta T$ and mass flow rate is simple. Apart from the changes in heat transfer coefficient due to the changes in density and viscosity arising from the increasing temperature, the temperature profile in the cooling channels is mostly linear. For a boiling fluid, this is not the case. In an ideal case where the changes in vapour quality are small and the frictional pressure drop is negligible, the temperature profile in a boiling flow can be expected to be isothermal. When boiling occurs over a wide range of vapour qualities, the heat transfer coefficient can change significantly as different boiling regimes take over. Additionally, the frictional pressure drop influences the saturation pressure and the temperature of the boiling fluid tends to fall over the channel length. The pressure drop could be exploited to tune the channel geometry, working fluid and coolant mass flow rate to obtain the wanted temperature gradient.

### 3.2.6. 1D AND 0D COOLING CHANNEL MODELLING

The fuel cell cooling channel is modelled and analyzed at two different levels of detail. At the most detailed level, a single cooling channel is modelled to understand the evolution of various physical quantities over the cooling channel length. At a higher system level, the fuel cell is modelled as a thermal energy source and only the inlet and outlet coolant conditions are calculated. At this level, the heat transfer coefficient is neglected and only the energy added to the coolant and the pressure drop in the cooling channels is of importance.

#### 1D MODEL

The cooling channel is discretized in $N_{\text{nodes}}$ points and at each node the local heat transfer coefficient and fluid properties are calculated. The heat flux at the cooling channel wall is constant. This means that for a single-phase flow the temperature increases linearly while for a two-phase flow, it is the vapour quality that increases linearly. The frictional pressure gradient is calculated at each node and the pressure drop is integrated over the node length. This allows for an evolution in pressure that in the case of two-phase flow changes the local saturation temperature. The flow is assumed to be developed laminar flow throughout the whole length of the cooling channel. The wall temperature is also calculated with the local heat transfer coefficient and the evolution of such temperature is recorded from inlet to outlet.

#### 0D MODEL

In the case of the 0D model to be used in the overall system model, the local variation of properties is neglected. The pressure drop is calculated with the mean fluid properties which represent the arithmetic average of the inlet and outlet states. The inlet thermodynamic conditions are fixed and the coolant mass flow is determined according to Equation 3.45 and Equation 3.55, where $Q_{\text{ch}}$ is replaced with $Q_{\text{stack}}$.

## 3.3. HEAT EXCHANGER MODEL

### 3.3.1. EPSILON-NTU METHOD

The main heat exchanger, which resides in a ram air duct (Figure 3.1), rejects the waste heat to the ambient air and is modelled using the $\epsilon$-NTU method presented in [53]. The method is used if the overall heat transfer coefficient is unknown and the heat transfer surface needs to be determined for a given heat load. The effectiveness $\epsilon$ is defined as the ratio of the actual heat transfer between one fluid and the other and the maximum possible heat transfer as in

$$\epsilon = \frac{Q}{Q_{\text{max}}}, \tag{3.71}$$

where $Q_{\text{max}}$ is limited by the fluid with the least heat capacity rate $C$ and the maximum temperature difference encountered in the heat exchanger. The heat capacity rate is defined as

$$C = c_p \dot{m}, \tag{3.72}$$

and the maximum temperature difference is the difference between the inlet temperatures of the hot and cold stream. The maximum heat transfer possible is thus

$$Q_{\text{max}} = C_{\text{min}} \left( T_{\text{h,in}} - T_{\text{c,in}} \right). \tag{3.73}$$

$C_{\text{min}}$ is often the air as the coolant has a larger heat capacity, when liquid, or has an apparent infinite heat capacity (isothermal heat transfer) if condensing.

While $Q_{\text{max}}$ is easy to calculate given the inlet conditions, the actual heat transferred is a function of the effectiveness as in

$$Q = \epsilon C_{\text{min}} \left( T_{\text{h,in}} - T_{\text{c,in}} \right). \tag{3.74}$$

Thus, a method to calculate the effectiveness is needed. Through the derivation in [53] it can be shown that for any type of heat exchanger the effectiveness is a function of the heat capacity rate ratio

$$C_r = \frac{C_{\text{min}}}{C_{\text{max}}}, \tag{3.75}$$

and the number of transfer units (NTU) as in

$$\epsilon = f\left(\text{NTU}, C_r\right). \tag{3.76}$$

NTU is dependent on both the media characteristics and the geometry as explained in subsection 3.3.2 of the heat exchanger and the functional form of the $\epsilon$-NTU relationship is given by the heat exchanger topology.

If the geometry needs to be sized, and the inlet and outlet conditions of one of the two fluids are imposed from design constraints, then the heat transferred is known and the effectiveness becomes an input parameter. The geometry necessary to arrive at the required NTU needs to be found iteratively.

#### SINGLE PHASE FLOWS

The topology investigated is of the cross-flow type as it is the most common topology of compact heat exchangers and is easy to manufacture. The air passes through the core of the heat exchanger from front to back while the coolant is crossing the core from one side to the other. As the airflow is finned and the coolant flow is constrained in mini channels within the flat tubes, thus neither flow mixes itself while passing through the heat exchangers and the temperature is not uniform over the heat exchanger area. The $\epsilon$-NTU relationship to be used for a cross-flow type heat exchanger with both fluids unmixed is

$$\epsilon = 1 - \exp\left[\left(\frac{1}{C_r}\right)(\mathrm{NTU})^{0.22}\left\{\exp\left[-C_r(\mathrm{NTU})^{0.78}\right] - 1\right\}\right] \tag{3.77}$$

as reported in Ref. [90]

#### CONDENSING FLOWS

In the case of a condensing flow, the apparent heat capacity rate is infinite and the heat transfer is almost isothermal at the coolant side. In this case the $\epsilon$-NTU relation changes and becomes independent of topology and $C_r$ as in

$$\epsilon = 1 - \exp(-\mathrm{NTU}). \tag{3.78}$$

### 3.3.2. GEOMETRY

The geometry selected for the main heat exchanger is the flat minichannel tube - offset strip fin geometry. Offset strip fins have the best balance of air side pressure drop and heat transfer coefficient according to Ref. [91], while flat tubes are easy to extrude and manufacture and are resistant to high pressures. Minichannel diameters can be manufactured down to 2 mm which limits the tube thickness thus reducing the blockage of air and increasing the surface area to volume ratio.

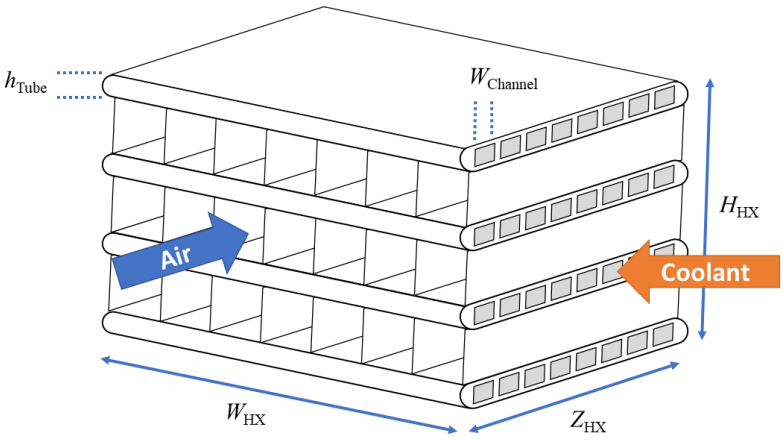


Figure 3.8: Flat minichannel tube - offset strip fin geometry.

The geometry is shown in Figure 3.8. The width and height of the heat exchanger are design parameters constrained by the available installation space. The depth $Z_{\mathrm{HX}}$ is a result from the sizing calculation. The fins and flat tubes have a fixed geometry. The flow velocity through the flat tubes and the number of channels is dependent on the width and so is the heat transfer coefficient on the coolant side. Thus an iterative approach is needed to calculate the necessary depth.

The tube geometry is defined by its height $h_{\mathrm{tube}}$ and its structural thickness $t_{\mathrm{tube}}$. The internal channel geometry is chosen to be square and is defined as

$$W_{\mathrm{channel}} = H_{\mathrm{channel}} = h_{\mathrm{tube}} - 2t_{\mathrm{tube}}. \tag{3.79}$$

The heat transfer area on the coolant (hot) side is given by the channel number, channel perimeter and HX width as in

$$A_{\text{hot}} = 2(W_{\text{channel}} H_{\text{channel}}) W_{\text{HX}} N_{\text{channel}}, \quad \text{with} \tag{3.80}$$

$$N_{\text{channel}} = \frac{Z_{\text{HX}}}{W_{\text{channel}} + t_{\text{channel}}} \frac{H_{\text{HX}}}{h_{\text{fin}} + h_{\text{tube}}}. \tag{3.81}$$

The heat transfer area on the air (cold) side is given by

$$A_{\text{cold}} = N_{\text{fin}}(A_{\text{primary}} + A_{\text{fin}}), \quad \text{with} \tag{3.82}$$

$$A_{\text{primary}} = 2\,s\,l, \tag{3.83}$$

$$A_{\text{fin}} = 2\,h_{\text{fin}}\,l + 2\,h_{\text{fin}}\,t_{\text{fin}} + s\,t_{\text{fin}}, \quad \text{and} \tag{3.84}$$

$$N_{\text{fin}} = \frac{W_{\text{HX}}}{s + t_{\text{fin}}} \frac{H_{\text{HX}}}{h_{\text{fin}} + h_{\text{tube}}}. \tag{3.85}$$

The overall heat transfer capacity of the heat exchanger $UA$, defined as the overall heat transfer coefficient times the overall heat transfer area, can then be calculated with

$$\frac{1}{UA} = \frac{1}{h_{\text{c,hot}} A_{\text{hot}}} + \frac{1}{h_{\text{c,cold}} A_{\text{cold}} \eta_{\text{surf}}}, \tag{3.86}$$

where the surface efficiency $\eta_{\text{surf}}$ is the efficiency of the surface extended by the offset strip fins. It is defined as

$$1 - \left( \frac{A_{\text{fin}}}{A_{\text{cold}}} (1 - \eta_{\text{fin}}) \right). \tag{3.87}$$

The fin efficiency $\eta_{\text{fin}}$ is a measure of how well the heat is conducted through the fin with respect to how well it is convected away. If the convection is poor and the conduction is high, the fin will almost have the same temperature as the base and thus have a high efficiency. It can be calculated with methods explained in [53] and is equal to

$$\eta_{\text{fin}} = \frac{\tanh(ml)}{ml}, \quad \text{with} \tag{3.88}$$

$$ml = \sqrt{\frac{2h_{\text{c,cold}}}{k_{\text{fin}}\,t_{\text{fin}}}} \frac{h_{\text{fin}} + t_{\text{fin}}}{2}. \tag{3.89}$$

Finally the NTU is defined as

$$\text{NTU} = \frac{UA}{C_{\text{min}}}. \tag{3.90}$$

In VCS systems, the coolant enters the main heat exchanger, which acts as a condenser, in superheated conditions. The heat exchanger is thus divided into two sections along its width with a moving boundary, one for desuperheating and one for condensation. This boundary, together with the heat exchanger depth, is calculated iteratively such that the desuperheating and condensation processes are satisfied.

Finally, the metal volume can be calculated from the overall geometrical details of the heat exchanger, and with it the weight. An additional 20% of metal is added on top of the calculated weight to account for header tanks, mounting points and fittings. Aluminum 3003 is assumed as heat exchanger material.

### 3.3.3. AIR SIDE

The most accurate experimental characterization of offset strip fin heat exchanger cores has been performed by Manglik and Bergles [92] and is reproduced in Ref. [53]. The geometry of an offset strip fin core is presented in Figure 3.9.

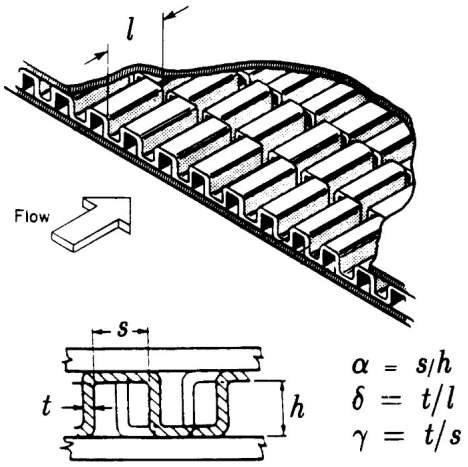


Figure 3.9: Geometry of offset strip fin heat exchanger core reproduced from Ref. [92].

### HEAT TRANSFER COEFFICIENT

The empirical correlation for the Colburn factor $j$ found in [92] is

$$\begin{aligned} j =& 0.6522\,\mathrm{Re}^{-0.5403}\,\alpha^{-0.1541}\delta^{0.1499}\gamma^{-0.0678} \\ &\times \left[1 + 5.269\times10^{-5}\,\mathrm{Re}^{1.340}\,\alpha^{0.504}\delta^{0.456}\gamma^{-1.055}\right]^{0.1}, \end{aligned} \tag{3.91}$$

where $\alpha$, $\gamma$, and $\delta$ are given in Figure 3.9. The Colburn factor is related to the Nusslet number by

$$j = \frac{Nu\cdot Pr^{-1/3}}{Re} \tag{3.92}$$

### PRESSURE DROP

The friction factor is similarly correlated to the geometrical variables through

$$\begin{aligned} f =& 9.6243\,\mathrm{Re}^{-0.7422}\,\alpha^{-0.1856}\delta^{0.3053}\gamma^{-0.2659} \\ &\times \left[1 + 7.669\times10^{-8}\,\mathrm{Re}^{4.429}\,\alpha^{0.920}\delta^{3.767}\gamma^{0.236}\right]^{0.1} \end{aligned} \tag{3.93}$$

The core inlet and outlet pressure drop contribution can be neglected in the case of small air-side blockage. Thus, the frictional pressure drop is dominating as suggested in Ref. [53].

### VERIFICATION

The air side correlations are verified with the use of the EchTerm software by Greth[2]. The results are shown in Table 3.4. The geometry and air velocity are values typically found in the application under investigation in this work. The results are within 2% error in difference as EchTerm uses the same widely validated correlations as the present work.

## 3.3.4. COOLANT SIDE

The coolant can either be a single-phase liquid or superheated vapour, for which the same calculation method for heat transfer coefficient and pressure drop as presented in subsection 3.2.3 applies or a two-phase condensing fluid. For this case, the pressure drop is calculated with the Friedel correlation and the tube entrance and exit losses are neglected according to the recommendations of Shah for preliminary analysis [53].

### HEAT TRANSFER COEFFICIENT

The heat transfer coefficient of a condensing flow can be calculated with the relation developed by Shah [93]. This relation is especially useful for the $\epsilon$-NTU method as it gives an accurate mean heat transfer coefficient

[2] https://greth.fr/echtherm/

Table 3.4: Air side correlations verification with EchTerm

| Parameters | Reference |
|---|---|
| $t_{fin}$ | 0.1 mm |
| $h_{fin}$ | 2.3 mm |
| $s_{fin}$ | 1.16 mm |
| $l_{fin}$ | 3.1 mm |
| $Z_{HX}$ | 2.2 cm |
| $V_{air}$ | 27.11 $m s^{-1}$ |
| $T_{air}$ | 20 °C |
| $P_{air}$ | 1 bar |

| Results | EchTerm | Present Work |
|---|---|---|
| $h_c$ | 336.3 $W m^{-2} K^{-1}$ | 343.55 $W m^{-2} K^{-1}$ |
| $\Delta p$ | 794.9 Pa | 781.5 Pa |

if used with the mean vapour quality encountered through the condensation process. The relation is

$$h_{TP,cond} = h_{LO}\left[(1-x_{vq,mean})^{0.8} + \frac{3.8 x_{vq,mean}^{0.76}(1-x_{vq,mean})^{0.04}}{P p_R^{0.38}}\right]. \tag{3.94}$$

### VERIFICATION

The verification of the coolant side heat transfer coefficient for condensation is verified with EchTerm using the same channel size as defined for the flat tubes of the main heat exchanger simulated in this work (Table 3.5). The uncertainty in predicting the condensing heat transfer coefficient is high and EchTerm provides a range of minimum, average and maximum heat transfer coefficients. The correlation used in the present work is on the lower side of the given heat transfer coefficient range. The impact of coolant side heat transfer coefficient is low in general, as the overall heat transfer in the heat exchanger is limited by the thermal resistance on the air-side. Thus, it is expected that the effect of uncertainty of coolant side heat transfer coefficient on heat exchanger design is low. Shah and Sekuli [53] suggest that for preliminray sizing of liquid to air heat exchangers the coolant side NTU can be even neglected by assuming a distribution of heat transfer resistance of 90% air and 10% liquid side, which is a typical distribution found in real compact heat exchanger applications.

Table 3.5

| Parameters | Reference |
|---|---|
| $T_{sat}$ | 90 °C |
| $G$ | 41 $kg s^{-1} m^{-2}$ |
| $x_{vq,eval}$ | 0.5 |
| $H_{channel}$ | 2.1 mm |
| $W_{channel}$ | 2.1 mm |

| Results | EchTerm | Present Work |
|---|---|---|
| $h_{TP,cond}$ | 3022 - 4862 - 6606 $W m^{-2} K^{-1}$ | 3409 $W m^{-2} K^{-1}$ |

## 3.4. AIR INTAKE MODEL

The ram-air duct that feeds air to the main heat exchanger starts with the intake. The intake model is needed to predict the drag caused by the ingestion and spillage of the incoming flow and to predict the pressure recovery that is obtainable from free stream conditions. The model is based on the technical report by ESDU [94] and is meant for subsonic Mach numbers. It is simplified for use in the present work by eliminating a dependency on Mach number and making it valid only for incompressible flow below $M = 0.2$. The type of inlet used is the scoop type as these inlets offer the highest pressure recovery. Additionally, flushed inlets can only be used if the heat exchanger is positioned inside a larger body, like the fuselage, but in this work a nacelle installation is used in order to make use of the higher dynamic pressure flow in the propeller wake for cooling also at low speeds.

The drag of the scoop inlet is separated into three components. The first drag contribution comes from the ingested air and its attributed momentum. This air then leaves the cooling duct but the contribution of the air exiting the duct to the overall force balance is accounted for in the nozzle model. The second component of drag is due to the spillage of air around the inlet. This happens if the ingested stream tube at infinity has a lower area than the inlet area and is schematically represented in Figure 3.10. In this situation, the inlet is

defined as running below nominal full flow conditions. It is not always possible to match the inlet area with the incoming stream tube area. In fact, the inlet area is determined by the diffuser which directly follows the intake. The diffuser area ratio is limited by the boundary layer growth inside the diffuser and the intake area might thus be larger than the stream tube it ingests. In this case, the air needs to slow down in a pre-diffusion and some will deviate around the inlet, causing the spillage drag. Finally, the drag contribution of the inlet and its fairing working at nominal conditions (full flow) due to airflow over and around it is added on top of the previous ones.

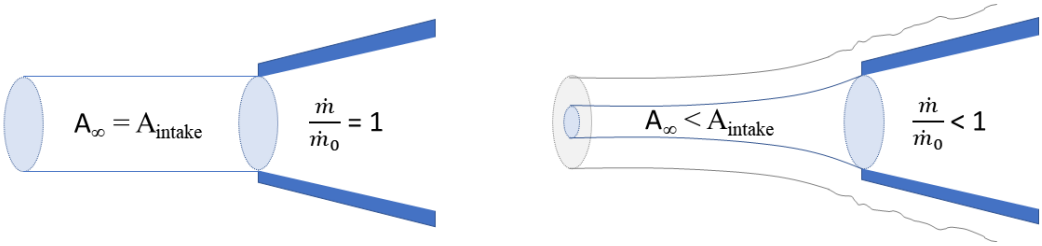


Figure 3.10: Representation of inlet running at full and reduced mass flow.

The drag contribution can be thus expressed as

$$D_{sc} = KV_0\dot{m} + D_{sp} + D_{f,full}. \tag{3.95}$$

where $V_0$ is the free stream velocity, $K$ is the momentum loss factor due to the ingestion of boundary layer, $D_{sp}$ is the contribution of spillage drag, and $D_{f,full}$ is the contribution of the fairing drag at full mass flow. The drag can be non-dimensionalized by dividing with the dynamic pressure of the free stream equivalent to $\frac{1}{2}\dot{m}_0 V_0$, where $\dot{m}_0$ is the mass flow that passes through an area of equal size to the inlet area in free stream conditions. This results in,

$$C_{Dsc} = 2K\left(\frac{\dot{m}}{\dot{m}_0}\right) + C_{Dsp} + C_{Df,full}. \tag{3.96}$$

$C_{Df,full}$ is constant with mass flow. $K$ depends on the relative height of the ingested boundary layer with respect to the inlet height. In the case of an inlet installed on the nacelle, the boundary layer is thin as it formed less than a meter in front of the inlet. Also due to the low Mach number, $K$ is between 0.95 and 1 thus its contribution is small. $C_{Dsp}$ is dependent on the inlet aspect ratio and lip geometry and can be expressed with

$$C_{Dsp} = k_f k_{sp,sc}\left(C'_D - C_{Df,full}\right)_{sh}. \tag{3.97}$$

The term $\left(C'_D - C_{Df,full}\right)_{sh}$ is the difference between the drag of the inlet at zero mass flow and full mass flow and the factor $k_{sp,sc}$ allows for the variation between zero and full mass flow of the spillage drag. Finally, the factor $k_f$ differentiates the lip geometry with NACA or elliptical-shaped lips having significantly less drag than sharp lips due to the suction effect they develop when spilled air passes over them.

The values of $k_f$, $k_{sp,sc}$, $\left(C'_D - C_{Df,full}\right)_{sh}$, $C_{Df,full}$, and $K$ are tabulated in charts given in Ref. [94].

## 3.5. DIFFUSER MODEL

The air entering the ram-air duct is slowed down in front of the radiator and this is achieved with a 2D diffuser. In a 2D diffuser of rectangular cross-section, only two opposite walls diverge to increase the diffuser area while the other two remain parallel to the core stream. The diffuser is sized and modelled following the work of Sovran and Klomp [95].

Diffusers are limited in the area ratio they can work at due to the excessive momentum decrease of the boundary layer and subsequent separation from the internal walls. This can be seen in Figure 3.11 where the lines show the combination of non-dimensional length and diffuser angle that result in flow separation.

A short diffuser can have a large diffuser angle but would result in a low area ratio due to the short axial length. Long diffusers need to have a much lower diffuser angle in order to avoid separation resulting in a

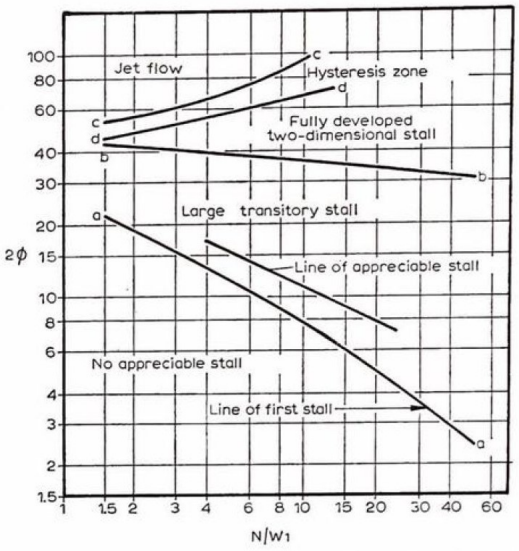


Figure 3.11: 2D Diffuser stall lines reproduced from Ref. [95].

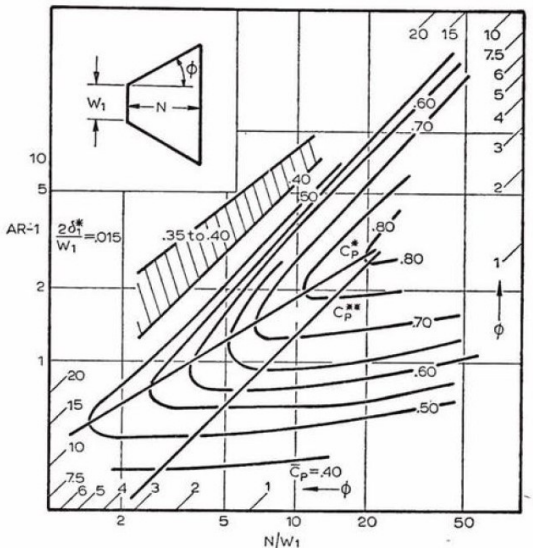


Figure 3.12: Diffuser performance chart first published in Ref . [96] and reproduced from Ref. [95]. $N$ is the diffuser length.

limited area ratio still. Suppose the boundary layer is slowed down excessively. In that case, it will occupy a larger portion of the cross-sectional area of the diffuser creating a non-uniform velocity distribution at the exit which limits the degree to which the core flow can be slowed down.

This is visualized with the diffuser performance map in Figure 3.12 developed by Reneau *et al.* [96] and reported in Ref. [95]. From the figure, two regions can be distinguished. The pressure recovery is almost linear with aspect ratio in the first region at low diffuser angles. For a given aspect ratio, a maximum pressure recovery point exists. This point, falling on the $C_P^{**}$ line, is at a non-dimensional length that maximizes the outlet effective area. This maximization is a balance between boundary layer growth due to excessive boundary layer deceleration and frictional losses. If a diffuser is too long, frictional losses will be excessive and induce boundary layer growth. Conversely, if the diffuser angle is high, a strong adverse pressure gradient can slow down the boundary layer and even promote separation.

The second region is marked by high diffuser angles. In this region, the maximum pressure recovery for a given diffuser non-dimensional length can be found. The maximum pressure recovery for given $N/W_1$ lies on the $C_P^*$ line. On this line, the pressure recovery is limited by excessive boundary layer growth due to strong adverse pressure gradients. If for a given $N/W_1$, the area ratio is made larger, the diffuser angle would be such that the boundary layer grows or detaches reducing the effective area at the outlet instead of increasing it further. The $C_P^*$ line marks the design space of compact optimal diffusers, limited by installation space, as they are in aerospace applications.

Analyzing the performance of diffusers with different inlet boundary layer displacement thicknesses, it was found that the $C_P^*$ line is independent of inlet conditions. Thus, the maximum possible area ratio achievable for a given diffuser installation space is easily found (see Figure 3.13).

Although the geometry for maximum pressure recovery is independent of inlet boundary conditions, the value of the pressure recovery achievable is. To calculate it, a method is proposed in Ref. [95] and reported here. The effectiveness of a diffuser is defined in terms of the ideal and actual pressure recovery as in

$$\varepsilon_0 = \frac{\Delta p}{\Delta p_i} = \frac{\Delta p/\bar{q}_1}{\Delta p_i/\bar{q}_1} = \frac{C_P}{C_{P,i}}. \tag{3.98}$$

where the pressure recovery $C_P$ is defined as

$$C_P = \frac{\Delta_p}{\bar{q}_1}, \quad \text{and} \tag{3.99}$$

$$\bar{q}_1 = \frac{\bar{u}_1^2}{2}\rho, \tag{3.100}$$

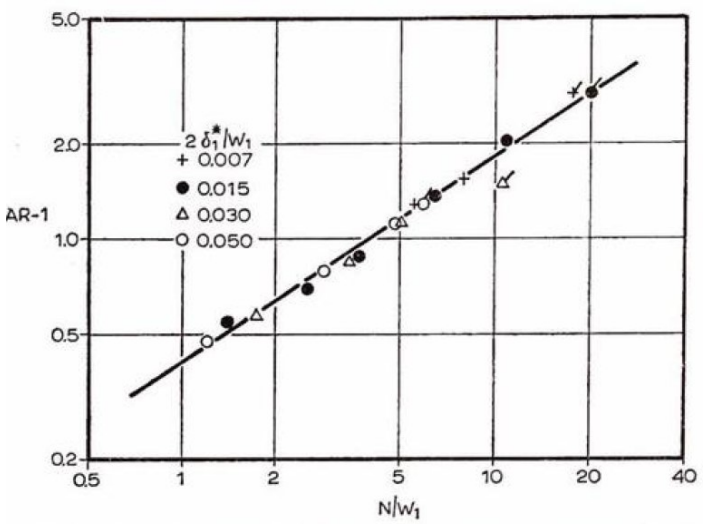


Figure 3.13: Area ratio at maximum pressure recovery independence from inlet boundary layer height. Taken from Ref. [95].

where $\bar{u}_1$ is the average flow velocity at the inlet. The ideal pressure recovery for an incompressible flow is a function of area ratio $AR$ as in

$$C_{\mathrm{P,i}} = 1 - \frac{1}{AR^2} \quad \text{with} \tag{3.101}$$

$$AR = \frac{W_2}{W_1}. \tag{3.102}$$

The effective area of a diffuser can be defined as the area that would be required for the flow to pass through with a uniform velocity distribution equal to the maximum velocity $U$ of the actual flow distribution, where the local actual flow velocity is $u$ with

$$A_{\mathrm{E}} = \int^{A} \frac{u}{U}\,\mathrm{d}A \tag{3.103}$$

If the effective area fraction $E$ is defined as

$$E = \frac{A_{\mathrm{E}}}{A}, \tag{3.104}$$

and the volumetric flow rate through the actual diffuser area is

$$\dot{V} = \int^{A} u\,\mathrm{d}A = \bar{u}A, \tag{3.105}$$

then it can be shown that

$$\dot{V} = \int^{A} u\,\mathrm{d}A = U\int^{A} \frac{u}{U}\,\mathrm{d}A = UAE, \tag{3.106}$$

and with it that

$$\frac{\bar{u}}{U} = E. \tag{3.107}$$

Thus, $E$ is the ratio of average velocity and maximum velocity of the flow through the diffuser. This parameter is important as the average velocity is related to the volumetric flow rate $\dot{V}$ and the maximum velocity is related to the velocity found in the inviscid core flow unaffected by the boundary layer. It is the velocity of the core flow that determines the pressure gradient in the diffuser and thus the pressure recovery.

Assuming that the inviscid core flow does not have any total pressure loss, the effectiveness can be redefined as

$$\varepsilon_0 = \frac{1}{E_1^2}\left[\frac{1 - \frac{(E_1/E_2)^2}{AR^2}}{1 - \frac{1}{AR^2}}\right]. \tag{3.108}$$

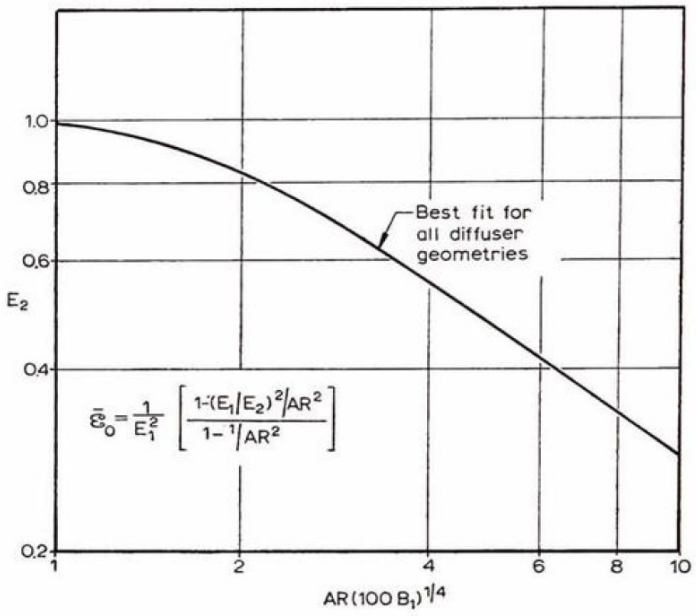


Figure 3.14: Fitted trend of E2 against $AR(100B_1)^{1/4}$ reproduced from Ref. [95].

Thus, by knowing the effective inlet and outlet area fraction $E_1$ and $E_2$ it is possible to determine the effectiveness of the diffuser. Through analysis of various published experimental datasets of subsonic diffusers ($M < 0.2$, $Re > 5 \cdot 10^4$), Sovran and Klomp [95] were able to derive a correlation for $E_2$ given the aspect ratio and inlet boundary layer height.

In fact it was shown that for diffusers on the $C_p^*$ line, the exit effective area fractio $E_2$ is correlated with the factor $AR(100B_1)^{1/4}$. The relation is shown in Figure 3.14, where

$$B_1 = 1 - E_1 = \frac{2\delta_1^*}{W_1}. \tag{3.109}$$

Where $B$ is the blocked area fraction.

The reduction in the effective exit area reduces the capability of recovering pressure. It is argued by Sovran and Klomp [95] that the pressure losses are negligible in subsonic diffusers due to the low boundary layer speed and as such the efficiency of diffusers is high. nevertheless, the reduction in pressure recovery is significant thus diffusers with low pressure recovery can be said to be 'ineffective'.

## 3.6. NOZZLE

The nozzle is modelled using the isentropic flow relations and it is assumed that total pressure losses are negligible. The outlet pressure is related to the Mach number through

$$p_{t,out} = p_{out} \cdot \left(1 + \frac{(\gamma-1)}{2} \cdot M_{out}^2\right)^{\gamma/(\gamma-1)}, \tag{3.110}$$

with the outlet pressure $p_{out}$ imposed to be equal to the ambient pressure. The nozzle is not expected to be chocked in any design condition but a check on the outlet critical pressure is implemented nevertheless. From the outlet Mach number, the flow velocity can be derived and the thrust force computed as in

$$F_{nozz} = \dot{m} V_{out}. \tag{3.111}$$

Additionally, the outlet area of the nozzle can be calculated through mass conservation as in

$$A_{out} = \frac{\dot{m}}{\rho V_{out}}. \tag{3.112}$$

## 3.7. AUXILIARY COMPONENTS MODELS

In this work, auxiliary components are defined as all the components that are not common to the various cooling systems analyzed.

### 3.7.1. PUMP

The pump works only with liquid, single-phase fluid, and thus is modelled simply with

$$P_{\text{pump}} = \frac{\Delta p}{\rho \eta_{\text{pump}}} \dot{m}, \tag{3.113}$$

where $\eta_{pump}$ is 0.75.

### 3.7.2. COMPRESSOR

The compressor works only with superheated vapour and is thus modelled through the ideal work done in isentropic conditions. The ideal enthalpy at the target outlet pressure is calculated assuming no entropy change from inlet to outlet giving

$$h_{\text{out,s}} = h(s_{\text{in}}, p_{\text{out}}). \tag{3.114}$$

The overall power consumed is then calculated through the actual enthalpy change as in

$$P_{\text{comp}} = h_{\text{out}} - h_{\text{in}} = \frac{h_{\text{out,s}} - h_{\text{in}}}{\eta_{\text{comp}}}, \tag{3.115}$$

where $\eta_{\text{comp}}$ is 0.75.

### 3.7.3. ELECTRIC MOTORS

Electric motors are connected to pump and compressor components. They drive them according to the power calculated in the respective components with an additional loss of 0.99 for mechanical friction and 0.95 for electrical losses. The power density of the electric motors, including the power electronics needed to drive them, such as inverters, is estimated to be 9 $\text{kWkg}^{-1}$ from existing commercially available electric motors[3,4].

### 3.7.4. INTERNAL HEAT EXCHANGERS

In some of the proposed cooling system variations, an internal heat exchanger is needed to transfer heat from one part of the cooling cycle to another. For example in the VCS subsystem, an internal heat exchanger is employed to superheat the vapour at the compressor inlet and to subcool the liquid at the condenser outlet. In this case, only the thermal energy transfer is calculated and the heat exchanger geometry and weight are neglected. It is assumed that having a rather small thermal energy transfer with respect to the main heat exchanger, the contribution to the overall system mass is small.

### 3.7.5. PHASE SEPARATOR

A phase separator is used in the VCS system to separate the vapour from the liquid phase at the outlet of the fuel cell. The separator has no weight nor pressure drop and the energy balance is computed on the basis of the incoming vapour quality and the saturated conditions as in

$$h_{\text{in}} \dot{m}_{\text{in}} = h_{\text{l,out}} \dot{m}_{\text{l,out}} + h_{\text{v,out}} \dot{m}_{\text{v,out}}, \quad \text{with} \tag{3.116}$$

$$\dot{m}_{\text{v,out}} = \dot{m}_{\text{in}} x_{\text{vq,in}}, \tag{3.117}$$

$$\dot{m}_{\text{l,out}} = \dot{m}_{\text{in}} (1 - x_{\text{vq,in}}). \tag{3.118}$$

[3] https://sci-mo.de/
[4] https://www.saluqimotors.com/

### 3.7.6. PIPING

The pipes that carry the coolant from the fuel cell stack to the main heat exchanger and back are modelled to include the pressure drop and the weight associated with the pipe material and the coolant they contain.

The pipe cross-section is determined by the imposed flow velocity, which is a design parameter. For liquid phases, the coolant velocity is 10 $m s^{-1}$. This is larger than the recommended 3 $m s^{-1}$ given in Ref. [97] but ensures that the pipe cross-section and the related weight are kept low. For two-phase flows, the velocity is set at 50 $m s^{-1}$ while for super-heated vapours a Mach number of 0.2 is imposed.

The pressure drop is calculated with the same correlation as presented in subsection 3.2.4. The wall thickness is set at a constant value of 2 mm while the pipe length is 3 m.

## 3.8. PUMPED SINGLE-PHASE COOLING SYSTEM MODEL

The model for the conventional pumped single-phase thermal management system (PSP) consists of a pump, heat exchanger and piping. The station in the cycle are shown in Figure 3.15. The P-h diagram for this cycle is shown in Figure 3.16. The coolant exits the fuel cell at a high temperature, corresponding to the highest specific enthalpy in the diagram at station 1. After the fuel cell, it is pumped to the highest pressure in the system at station 2. As the coolant is an incompressible liquid, the specific enthalpy does not change over the pump. It flows through the heat exchanger which lowers the temperature and thus enthalpy and causes a pressure drop (station 3). The pressure drop over the heat exchanger is added to the pressure drop over the piping and this is represented by a single process from 2 to 3. After the main heat exchanger, the coolant flows back to the fuel cell where it heats up again, increasing its specific enthalpy, and suffers a further pressure drop.

It amount of coolant needed to fill up the cycle is computed by summing up the volume of the fuel cell cooling channels, main heat exchanger flat tube channels and the pipes.

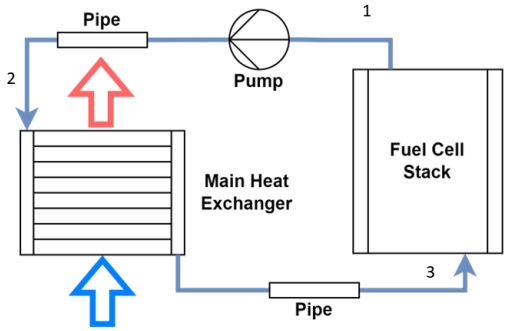


Figure 3.15: Conventional pumped single phase system model.

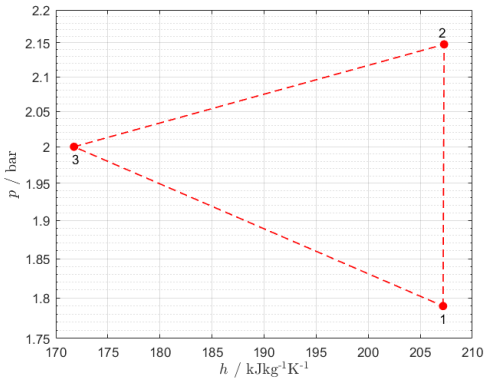


Figure 3.16: Representation of PSP system process on P-h diagram of 50% ethyl-glycol water mixture.

## 3.9. PUMP MULTI-PHASE SYSTEM MODEL

The pumped multi-phase system (PMP) comprises the same components as the PSP system and is shown in Figure 3.17. The pump is positioned after the main heat exchanger instead of the fuel cell. This is done as to avoid pumping a two-phase flow which would require higher power due to the volume change of the vapour phase during compression. The T-s diagram is chosen to highlight the thermodynamic processes in this system and is shown in Figure 3.18. The solid line represents the phase boundary. The coolant exits the fuel cell as a vapour-liquid mixture at station 1. After passing through the pipe it flows to the main heat exchanger and reaches station 2 in saturated liquid state. After being pumped, it enters the fuel cell at station 3 in subcooled conditions. The pressure drop encountered by the coolant while flowing in two-phase influences the amount of subcooling at the fuel cell inlet.

The system coolant charge is calculated by taking the bigger of either:

- The mass of coolant that is needed to fill up the whole cycle under operating conditions taking into account the density of the coolant at the operating pressures and temperatures in each component.
- The mass of coolant that is needed to fill up the entirety of the fuel cell cooling channel volume assuming the coolant in saturated liquid conditions at an ambient temperature of 20 °C.

The latter condition corresponds to a "flooded evaporator start" condition. This allows for the coolant to warm up during startup before reaching the desired operating temperature and pressure. For some coolants, this condition results in sub-atmospheric pressures being present in the system when in cold shutdown conditions.

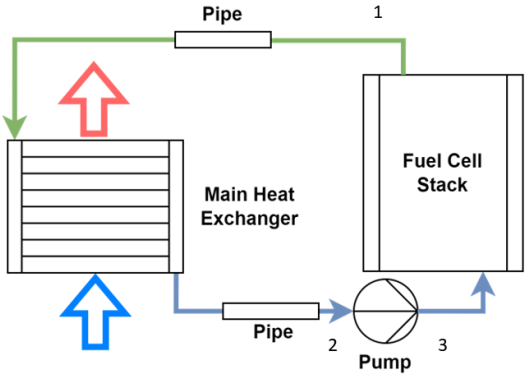


Figure 3.17: Pumped multi-phase system model.

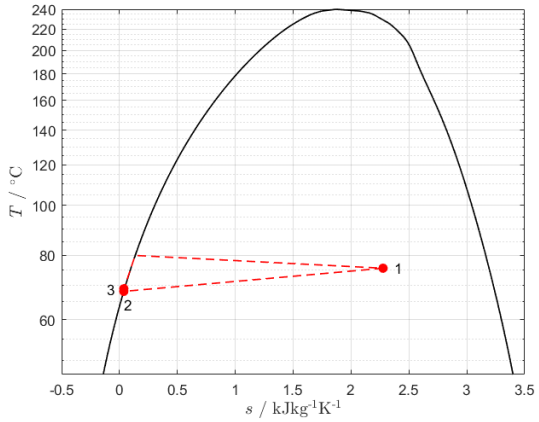


Figure 3.18: Representation of PMP system process on T-s diagram of methanol.

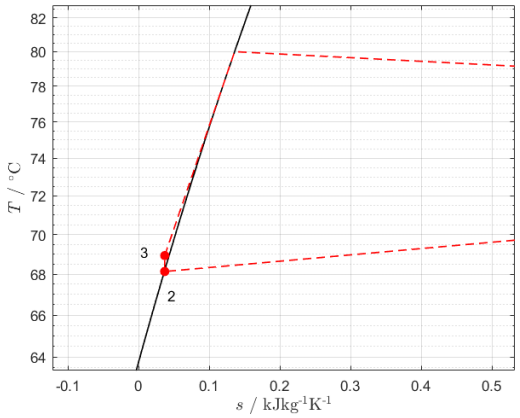


Figure 3.19: T-s diagram detail of the liquid pumping and subcooled coolant heating at the fuel cell inlet.

## 3.10. VAPOUR COMPRESSION SYSTEM MODEL

The vapour compression system modelled in this work has an architecture similar to the one used by Reichler [25] (see Figure 2.10). It differs in two main aspects. First, the superheating of the saturated vapour before entering the compressor is achieved by exchanging heat with the coolant after the condenser, not before. Although the pressure drop and size of the internal heat exchanger are not modelled, using a saturated liquid instead of superheated vapour could bring benefits in both size and reduced pressure drop. Secondly, the pump is moved from the two-phase flow region after the mixer to the single-phase liquid region between the separator and the mixer. In this way, the lowest pressure is at the fuel cell exit and the pump can operate with a liquid instead of a vapour-liquid mixture. Additionally, only part of the total coolant mass flow passes through the pump. The chosen system architecture is shown in Figure 3.20.

Figure 3.21 shows the T-s diagram for the VCS system. The coolant exits the fuel cell at station 1' in two-

phase flow. In the separator, the coolant is split between the vapour (station 1) and liquid (station 7) phases. The vapour phase is superheated in the internal heat exchanger and fed to the compressor at station 2. After passing the compressor and piping, it enters the main heat exchanger at station 3. The coolant is first de-superheated, reaching saturated vapour conditions mid-through the main heat exchanger at station 3'. Then it is condensed and exits in saturated liquid state at station 4. It then flows through the internal heat exchanger where it is subcooled to station 4'. It is then throttled (station 5) and meets the liquid part separated earlier at the mixer. At station 6 the two coolant streams are fully mixed and enter the fuel cell again. The liquid separated at station 7 is pumped to the mixer (station 8) to overcome the pressure drop of the fuel cell stack. A detailed view of the mixing process is shown in Figure 3.22.

The coolant charge needed to fill the cycle is calculated in the same way as the PMP system.

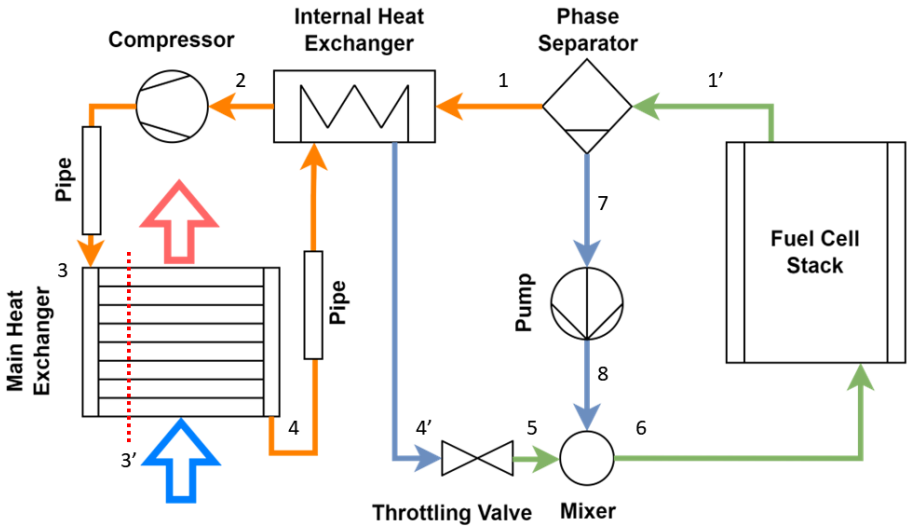


Figure 3.20: Vapour compression system model.

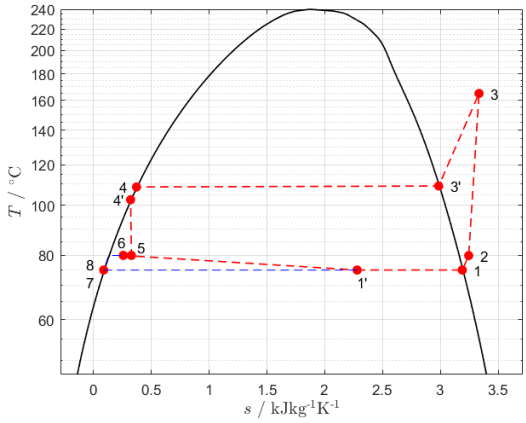


Figure 3.21: Representation of VCS system process on T-s diagram of methanol.

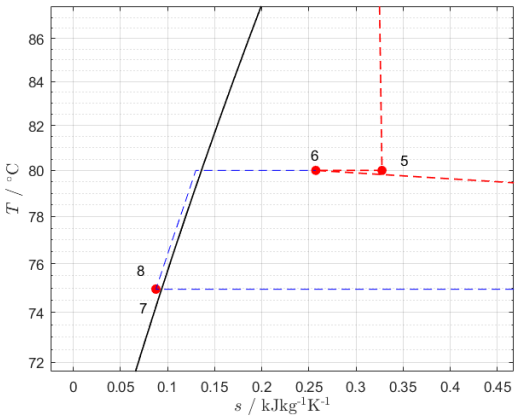


Figure 3.22: T-s diagram detail of the phase separation, liquid pumping and mixing at the fuel cell inlet.

## 3.11. AIRCRAFT INTEGRATION

The reference aircraft used to size and model the thermal management system is the Dash-8 Q300 regional turboprop airplane. Figure 3.23 shows the airplane in flight (Source: aerospace-technology.com[5]), while relevant airplane dimensions, including approximate nacelle dimensions relevant for the ram air duct sizing, are given in Figure B.1.

Figure 3.23: Dash-8 Q300 in flight. Credit: Bombardier Inc.

### 3.11.1. POWER REQUIREMENTS

The Dash-8 300 has two Pratt & Whitney PW123 turboprop engines[98] each delivering around 1800 kW of power[6]. To match the required take-off power the fuel cell stack sized and modelled by Datta *et al.* [11] for aircraft applications is used. Each stack has a gross power of 600 kW with 12.5% power absorbed by the balance of plant. The stack operates at a cell voltage of 0.7 V and a current density of 1.5 A cm$^{-2}$. The resulting efficiency is 47% at maximum power. Four stacks are used to form a single propulsion unit. It is assumed that ram air ducts could be mounted on both sides of the nacelle thus only half the system (2 fuel cell stacks) is simulated.

The only simulated operating point is take-off at maximum power. As the focus is on thermal management sizing, no snowball effects on fuel cell size or power output are included. Thus, the thermal power released by the fuel cell is constant for all simulated designs.

### 3.11.2. INSTALLATION SPACE AND GEOMETRY

The ram air duct geometry is shown in Figure 3.24. The overall length is set to 5.5 m with one meter always dedicated to the nozzle. The remaining length is split between the diffuser length and heat exchanger length as in

$$L_{\text{Diff}} + L_{\text{HX}} = 4.5\text{m}. \tag{3.119}$$

The heat exchanger length is a function of duct height and tilt angle as in

$$L_{\text{HX}} = H_{\text{Duct}} cos(\theta_{\text{HX}}) \tag{3.120}$$

The width of the duct (out of plane in Figure 3.24) is limited to 1.5 m to ensure the intake remains inside the propeller wash. The duct height is limited by the space available under the wing and is limited to 1.25 m.

With $\theta_{\text{HX}}$ angles smaller than 90°, a larger heat exchanger can be installed in the same duct cross-section. This allows for a larger frontal area and thus smaller thickness reducing pressure drop. Additionally, the air is slowed down even more before entering the heat exchanger as it passes through it normal to the front face rather than in line with the longitudinal duct axis.

[5] https://www.aerospace-technology.com/projects/bombardier_q300/
[6] https://www.pwc.ca/en/products-and-services/products/regional-aviation-engines/pw100-150

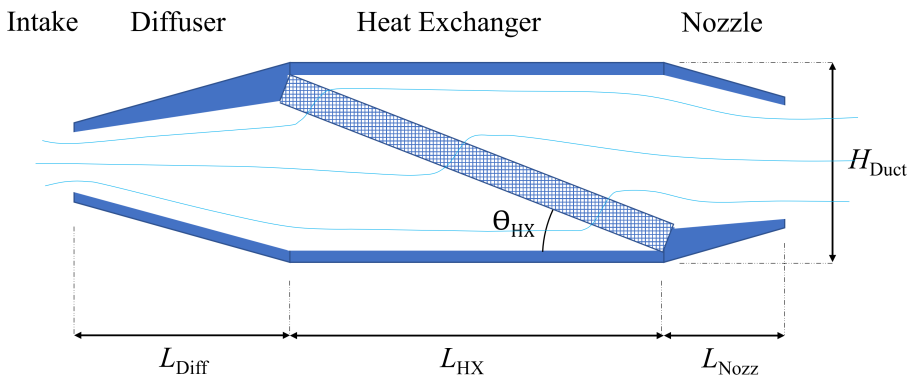


Figure 3.24: Ram air duct geometry.

The effects of heat exchanger angle with respect to the incoming airflow have been investigated already by NACA in 1942 [99]. Through experiments, it was found that at the same mass flow and heat exchanger frontal area, pressure drop increases slightly up to $\theta_{HX} = 30°$ ($\theta_{NACA} = 70°$) as shown in Figure 3.25. After that, a sudden rise in pressure drop is observed. This rise in pressure drop is induced by flow separation at the leading edge of the flat tubes in the heat exchanger core. Additional experiments have been performed by Henriksson *et al.* [100]. In these experiments, the supply duct was kept of the same geometry and the heat exchanger area exposed was thus inversely proportional to the tilt angle. For the same amount of flow, a lower pressure drop is induced over heat exchangers with lower tilt angles as shown in Figure 3.26. Below $\theta_{HX} = 30°$ the pressure drop starts to increase again. The results are equivalent to those of NACA but the perspective is shifted. If the duct geometry is fixed, heat exchanger tilt reduces pressure drop due to the increased frontal area. On the contrary, if the heat exchanger frontal area is fixed, the pressure drop increases slightly with lower tilts angles up until stall is reached. At that point, a large increase in pressure drop is observed. No method to model this phenomenon has been found in literature, thus results need to be judged qualitatively to infer whether increased pressure drop due to low tilt angle is to be expected or not.

Finally, the component dimensions matching has to be considered. The width of the duct is maintained equal to its entire length. The duct height varies. At the centre portion, the duct height is defined. The diffuser outlet matches the duct height as does the nozzle inlet. The intake height, which coincides with the diffuser inlet, is determined either by diffuser half-angle limitations or by ingested stream tube height, depending on which parameter is most limiting. The nozzle outlet height is determined through its area given that the nozzle outlet width is maintained equal to the duct width.

### 3.11.3. PROPELLER WAKE MODELLING

The installation of the ram air duct on the side of the nacelles of the aircraft exploits the propeller wake to cool the fuel cell also when the aircraft is not moving. Additionally, during take-off and climb out, increased dynamic pressure is present in front of the ram air duct further increasing cooling capacity. As a reference point for the aerodynamic boundary conditions in front of the duct, it is assumed that the aircraft is at the end of the take-off run. A take-off speed of approximately 111 knots (57 $m\,s^{-1}$) is assumed for the Dash-8 Q300. The propeller diameter is given in Figure B.1 and to estimate the propeller efficiency, JavaProp is used [101]. JavaProp is a simple application that allows estimating propeller performance through blade element theory. For the estimation of the efficiency, a 4-bladed propeller with the standard airfoil profile proposed in the software is used. The efficiency at take-off is 77% with 1800 rpm and 15 kN of thrust per engine.

To derive the airspeed and pressure after the propeller disc, an simple actuator disc model is used [102].

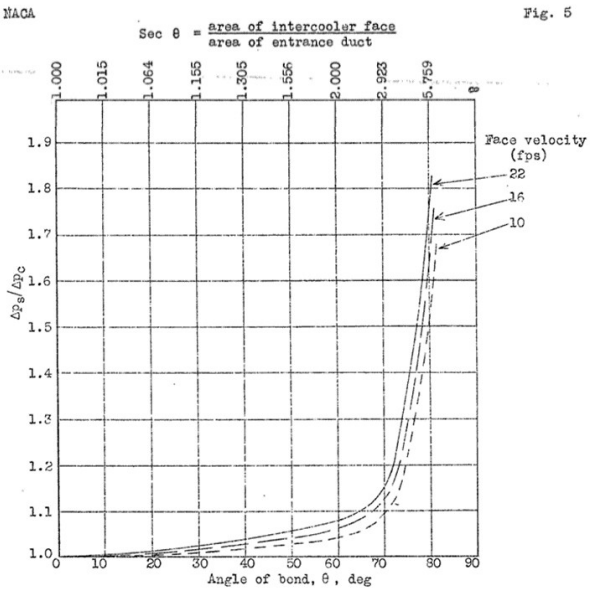


Figure 3.25: Pressure drop relative difference for various installation angles and fixed HX frontal area. In this figure $\theta_{NACA} = 90° - \theta_{HX}$. Reproduced from Ref. [99].

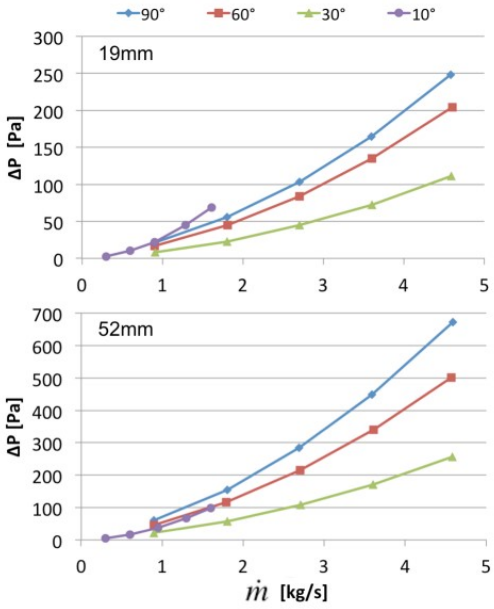


Figure 3.26: Pressure drop of two different HX cores at various tilt angles and fixed supply duct geometry. Reproduced from Ref. [100].

The model is based on a set of 3 equations that need to be solved iteratively. The equations are:

$$\dot{m} = \rho A_{\text{prop}} \frac{V_e - V_\infty}{2}, \tag{3.121}$$

$$F_{\text{prop}} = \dot{m}(V_e - V_\infty), \tag{3.122}$$

$$\eta_{\text{prop}} = \frac{F V_\infty}{P_{\text{prop}}}, \tag{3.123}$$

where $A_{\text{prop}}$ is the propeller disc area, $V_\infty$ and $V_e$ are the free stream air speed and the air speed far down-stream in the propeller wash, $F_{\text{prop}}$ is the propeller thrust and $P_{\text{prop}}$.

The flow velocity at the propeller disc is defined as

$$V_{\text{disc}} = \frac{V_e - V_\infty}{2}, \tag{3.124}$$

The total pressure in the propeller wake can be calculated from the conditions far down-stream where the pressure inside the wake has reached equilibrium with the ambient pressure as in

$$p_{t,e} = p_{\text{amb}} + \frac{1}{2}\rho V_e^2. \tag{3.125}$$

Finally, the static pressure right behind the propeller is calculated using

$$p_{\text{disc}} = p_{t,e} - \frac{1}{2}\rho V_{\text{disc}}^2. \tag{3.126}$$

As the intake is positioned right behind the propeller, $V_{\text{disc}}$ and $p_{\text{disc}}$ are used as reference-free stream conditions for the intake model. When an intake is simulated with a low mass flow ratio (see section 3.4), it is assumed that the stream tube divergence and thus pre-diffusion happens without limitations. The small space between the propeller and intake might limit the validity of this assumption as the airflow might not have the space necessary to undergo the pre-diffusion assumed.

### 3.11.4. PERFORMANCE INDICATORS

To compare and evaluate different system architectures and design variables, a few performance indicators are used. The most important one is total available power $P_{tot}$. The total available power represents the power that can be used to propel the aircraft. It takes into account power lost to drag, power lost to system components, and power lost to additional weight. It is calculated as in

$$P_{tot} = P_{FC} - P_{sys} - P_{drag} - P_{weight}. \tag{3.127}$$

Where $P_{FC}$ is the net power produced by the fuel cell system, which already includes losses due to balance of plant components. $P_{sys}$ is the power consumption of pumps and compressors in the thermal management system. The drag power is calculated as

$$P_{drag} = F_{drag} V_{\infty}, \quad \text{where} \tag{3.128}$$

$$F_{drag} = F_{intake} - F_{nozzle}. \tag{3.129}$$

Note that by convention, positive $P_{drag}$ means a power loss to drag, while a negative value means that the system is producing additional thrust.

The power loss relative to the system weight is due to the lift-induced drag and is calculated as

$$P_{weight} = \frac{m_{sys}\, g}{L/D}\, V_{\infty}, \tag{3.130}$$

where $L/D$ is the lift-to-drag ratio estimate for the given aircraft. For a Dash-8 an $L/D$ of 15 is used according to Ref. [103].

The cooling power penalty is similar to total available power but excludes the fuel cell power and is positive for power losses as in

$$P_{cool,penalty} = P_{sys} + P_{drag} + P_{weight}. \tag{3.131}$$

Finally, the core efficiency is defined for the ram air duct. Its purpose is to highlight if, and how well, the ram air duct - heat exchanger configuration is able to convert thermal power to thrust. It is derived from the jet generation efficiency of a conventional aero-engine and is defined as

$$\eta_{core} = \frac{\frac{1}{2}\dot{m}\left(V_{nozz,out}^2 - V_{\infty}^2\right)}{\dot{Q}_{HX}} \tag{3.132}$$

## 3.12. SYSTEM DESIGN SPECIFICATIONS

The design parameters selected for the system simulations are summarized in this section. Table 3.6 shows the design parameters for the fuel cell. Two fuel cells are simulated per side of the nacelle, totalling 4 per engine. The fuel cell design parameters are shared amongst all configurations. Similarly, Table 3.7 gives the design parameters of the main heat exchanger, which are again shared amongst all architectures. In Table 3.8, the process constraints specific to each cooling fluid are given. These parameters are needed to constrain the the thermodynamic states of the system. Finally, Table 3.9 gives the free design parameters that are used to span the explored design space. A linear range of each parameter is generated and the resulting vectors are permutated with each others. This generates a combination of designs that spans the complete range of values shown and is then simulated to generate the results shown in chapter 5.

## 3.13. MODELLING LANGUAGE AND SIMULATION ENVIRONMENT

Two programming languages are used to implement the models described in this work. The first language, Matlab, is used for the evaluation of fluids and the 0D and 1D simulation of cooling channels in the fuel cell. Additionally, Matlab is used for data processing and visualization.

For all other models needed for system simulations, Modelica[7] is used [104]. Modelica is an object-oriented programming language developed specifically for system simulation of any physical system. The

[7] https://modelica.org/

Table 3.6: Fuel cell design parameters valid for all system architectures.

| Fuel Cell Design Parameters | |
|---|---|
| $V_{stack}$ | 250 V |
| $P_{stack}$ | 600 kW |
| $N_{stacks}$ | 2 |
| $i$ | 1.5 A cm$^{-2}$ |
| $V_{op}$ | 0.7 V |
| $\Lambda_{cell}$ | 4 |
| $W_{ch}$ | 0.75 mm |
| $H_{ch}$ | 0.75 mm |

Table 3.7: Main heat exchanger design parameters valid for all system architectures.

| Main HX Design Parameters | |
|---|---|
| $h_{tube}$ | 2.5 mm |
| $t_{tube}$ | 0.2 mm |
| $t_{fin}$ | 0.1 mm |
| $\alpha$ | 0.5 |
| $\gamma$ | 0.086 |
| $\delta$ | 0.032 |

Table 3.8: Fluid specific design parameters. Condenser temperatures and pressures are only valid for VCS systems.

| EGW50 | |
|---|---|
| $T_{FC,in}$ | 70 °C |
| $\Delta T_{FC}$ | 10 K |

| Methanol | | | |
|---|---|---|---|
| $T_{sat,FC}$ | 80 °C | | |
| $p_{sat,FC}$ | 1.81 bar | | |
| $x_{vq,FC,out}$ | 0.7 | | |
| $T_{sat,cond}$ / °C | 90 | 100 | 110 |
| $p_{comp,out}$ / bar | 2.56 | 3.54 | 4.8 |

| R1233ZDE | | | |
|---|---|---|---|
| $T_{sat,FC}$ | 77 °C | | |
| $p_{sat,FC}$ | 6.11 bar | | |
| $x_{vq,FC,out}$ | 0.8 | | |
| $T_{sat,cond}$ / °C | 90 | 100 | 110 |
| $p_{comp,out}$ / bar | 8.33 | 10.42 | 12.88 |

Table 3.9

| Free design parameters | |
|---|---|
| $H_{duct}$ | 0.5 - 1.25 m |
| $W_{duct}$ | 0.75 - 1.5 m |
| $\epsilon_{HX}$ | 0.2 - 0.8 |
| $\theta_{HX}$ | 10 - 35 ° |

object-oriented nature of Modelica fits well with the development of modular a-causal system models. The most powerful feature of Modelica is the use of symbolic variables. This enables equation manipulation that allows one to write equations without defining a solution strategy, as it is later determined by the solver. The solution strategy is then compiled into C++ to be simulated.

The models were implemented inside the framework of the DeSimECS library developed by the Propulsion and Power department of the Aerospace faculty of TU Delft. Additionally, the ExternalMedia Library 3.2.1 and 3.3.1 were used as interfaces to REFPROP and CoolProp.

Dymola[8] is used as IDE and Visual Studio 2019 as C++ compiler. The solver used is DASSL [105] which is intended for solving differential algebraic equations. As the simulations are all steady state and no differential equations are present, only the portion of the algorithm that solves implicit equations with a variation of Newton's method is relevant.

To launch a large number of simulations automatically and parametrically, the python interface of Dymola is used to write a simulation manager. This program utilises the multiprocessing library of python to run simulations in parallel and improve simulation time. A set of 5040 simulations spanning 3 system configurations, 3 pressure levels and 4 free design parameters takes approximately 10 hours to run on an Intel Core i7-6700HQ CPU.

[8] https://www.3ds.com/products-services/catia/products/dymola/

# 4

# VALIDATION

## 4.1. PREDICTION OF HEAT TRANSFER COEFFICIENT IN FLOW BOILING FUEL CELL COLING

Out of the few experimental investigations using flow boiling to cool a fuel cell, Choi *et al.* [29] present the recorded data on heat transfer coefficient in a way that is readily comparable to the predictions of the Kandlikar two-phase boiling correlation. The coolant used is HFE-7100, which differs from the fluid chosen in this work for further investigation, but is more similar to R1233ZDE than Methanol in physical properties. No experimental investigation of Methanol and R1233ZDE applied to fuel cell cooling has been found.

The experiment uses electrical resistances to simulate the heat released by the fuel cell. The resistances are mounted within a graphite block in which the cooling channel are machined. The block is insulated from the environment in order to limit heat transfer through modes other than boiling. Only half a cooling channel plate is modelled in this way as thermal energy is introduced in the channels from one side (the bottom) while the top is covered in a transparent material to investigate the flow boiling phenomenon visually. The test section of the experimental setup by Choi *et al.* [29] is given in Figure 4.1. The channels are wider than the one used in this work but fall within the minichannel classification by Kandlikar. The geometry and operating conditions are given in Table 4.1.

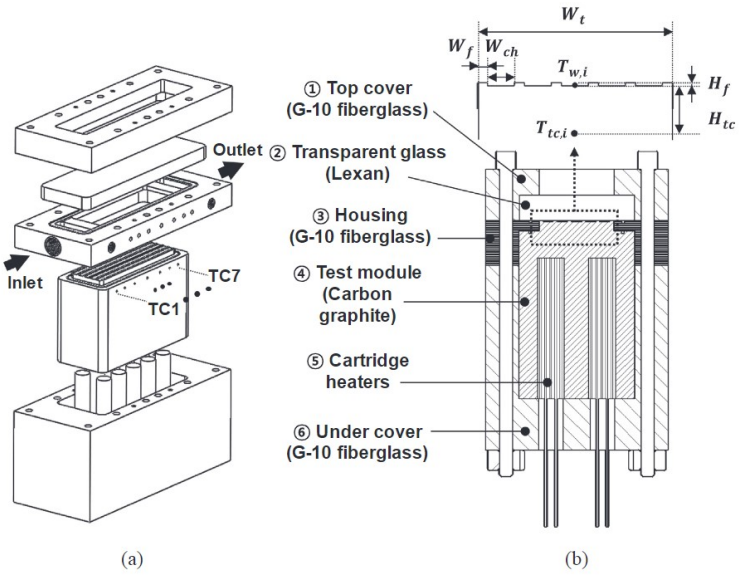


Figure 4.1: Test section of experimental set used in Ref [29]. a) Composition, b) Cross-view. Reproduced from Ref. [29].

Table 4.1: Geometrical, Operational and Fluid Parameters used in Ref. [29].

| Parameters | Ref. [29] |
|---|---|
| $W_{ch}$ | 4 mm |
| $H_{ch}$ | 0.5 mm |
| $L_{ch}$ | 90 mm |
| $D_h$ | 0.889 mm |
| $G$ | 200 $kg\,s^{-1}\,m^{-2}$ |
| $q_{ch}$ | 18.8 - 68.9 $kW\,m^{-2}$ |

| Fluid Properties | HFE-7100 Ref. [106, 107] |
|---|---|
| $T_{sat}$ | 61 °C |
| $p_{sat}$ | 1.01 bar |
| $\rho_l$ / $\rho_v$ | 1418.7 / 9.74 $kg\,m^{-3}$ |
| $\mu_l$ / $\mu_v$ | 42.6 / 0.012 mPa s |
| $c_p$ | 1183 $J\,kg^{-1}$ |
| $k_l$ | 0.069 $W\,m^{-1}\,K^{-1}$ |
| $h_{lv}$ | 112 $kJ\,kg^{-1}$ |
| $\sigma$ | 0.01 $N\,m^{-1}$ |

The fluid properties of HFE-7100 are not available for saturated conditions in REFPROP thus other sources are used as a reference for the fluid properties [106, 107]. The saturation temperature in the experiment of Choi *et al.* [29] is 61 °C and the relevant properties are in Table 4.1.

The investigated range of wall heat fluxes (18.8 - 68.9 $kW\,m^{-2}$) is rather high as channels of similar dimensions researched by Soupremanien et al. for fuel cell cooling only reach a maximum of 10 $kW\,m^{-2}$. This is more in line with the values obtained in this work (see section 5.2).

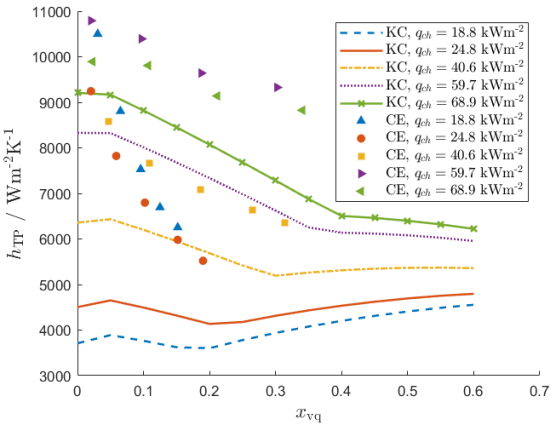


Figure 4.2: Flow boiling heat transfer coefficient as measured in Ref. [29] and predicted by the correlation of Kandlikar and Balasubramanian [71].

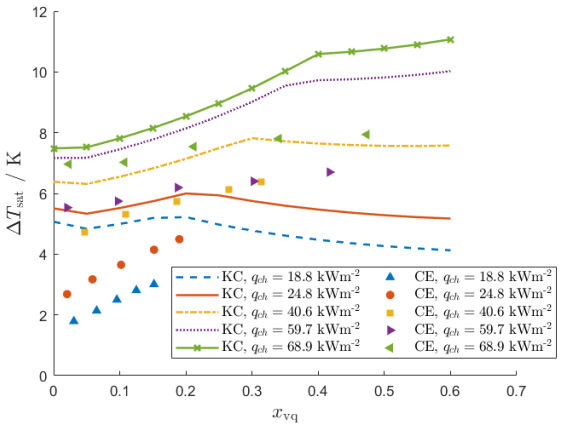


Figure 4.3: Wall superheat as measured in Ref. [29] and predicted by the correlation of Kandlikar and Balasubramanian [71].

Figure 4.2 shows the measured heat transfer coefficients in the experiment of Choi *et al.* [29] compared to the heat transfer coefficient obtained from the Kandlikar correlation. The difference between them is clear with the Kandlikar correlation underestimating the heat transfer coefficient. In the worst case, at the lowest heat flux, the difference in predicted and measured heat flux is a factor of 3. The negative trend of $h_{TP}$ with vapour quality is typical of nucleate boiling and the correlation matches the experiments with the correct trend for nucleate boiling.

In Figure 4.3 the wall superheat $\Delta T_{sat}$ is plotted. As the heat transfer coefficient is generally high, the absolute wall temperature error is small. In fact, at the worst case, a difference in $\Delta T_{sat}$ of only 3 K is found ($q_{ch}$ = 18.8 $kW\,m^{-2}$, low vapour quality). From the definition of $\Delta T_{sat}$ in Equation 3.59 the wall temperature at low $x_{vq}$ and $q_{ch}$ is measured to be 63 K but predicted to be 66 K. This is an error in wall temperature of just 4.8%, which is acceptable for preliminary system design.

In general, the validity of the Kandlikar correlation for fluids not included in the original dataset needs to be verified experimentally and the fluid-surface interaction parameter should be tuned accordingly. If a high enough heat transfer coefficient can be ensured, the error in wall temperature is small and the impact on system level design needs to be evaluated.

## 4.2. OFFSET STRIP FIN HEAT EXCHANGER

To validate the correlations for offset strip fins the experimental work of Hao *et al.* [108] is used as reference. Ref. [108] uses a simplified numerical approach to model an offset strip fin heat exchanger for cooling of a hybrid electric vehicle powertrain. The simplified method is used to optimize an existing heat exchanger geometry. The initial and optimized geometries are then tested in a set-up as shown in Figure 4.4. In the experiments, the water heater power is maintained constant, as is the water mass flow. As the air flow is varied, the system reaches a new steady state and the water inlet temperature to the heat exchanger varies accordingly. The system is left to reach steady state for 30 min at each test point. The experiment confirms that the optimized geometry has better performance, especially in air side pressure losses. As the purpose of using this study is a reference for validation, only the original geometry is used to compare numerical and experimental results with the predictions of the heat exchanger model presented in this work.

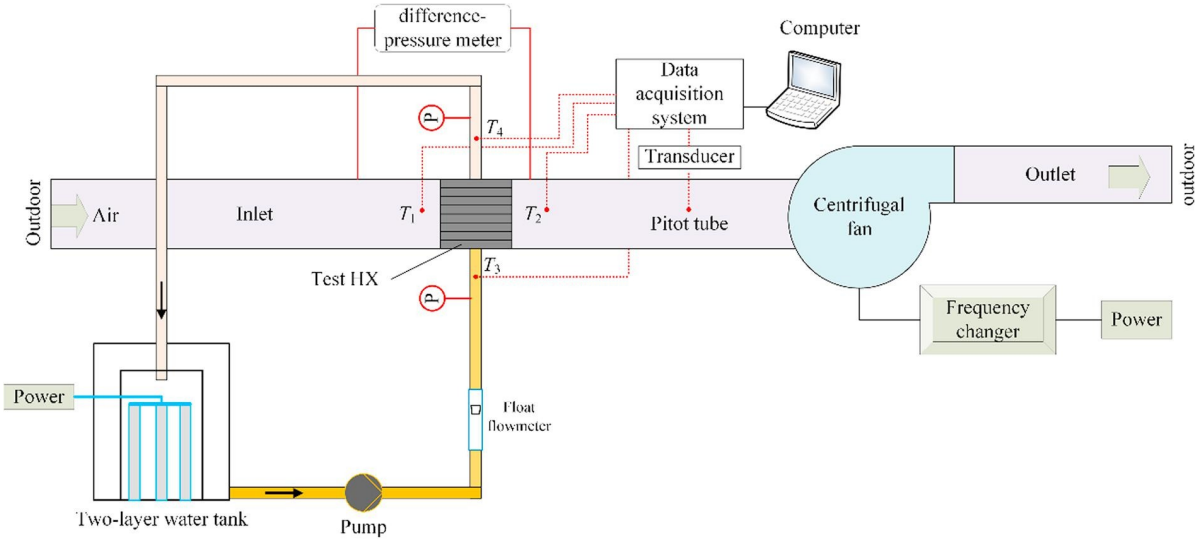


Figure 4.4: Test set-up used in Ref. [108]. Reproduced from Ref. [108].

The heat exchanger geometry and the operating parameters are presented in Table 4.2. Although in Ref. [108] both air and water side have offset strip fins, the heat exchanger model used in the present work has fins only on the air side. The water side is kept with continuos minichannels with the same dimensions as the offset fins in Ref. [108]. This is a limitation of the used model, but as the heat transfer is dominated by the resistance on the air side, and only the air side correlations are of interest for the validation, this is acceptable. Furthermore, it will be shown that even with this limitation, the presented heat exchanger model matches the experiments better than the one proposed by Hao *et al.* [108].

Table 4.2: Geometrical and operating parameters of the offset strip fin heat exchanger experiment in Ref. [108].

| Overall Geometry | | Water Tubes | | Air Fins | | Operating Parameters | |
|---|---|---|---|---|---|---|---|
| $W_{HX}$ | 200 mm | $h_{tube}$ | 5 mm | $t_{fin}$ | 0.2 mm | $\dot{m}_{water}$ | 0.54 kgs$^{-1}$ |
| $H_{HX}$ | 200 mm | $t_{tube}$ | 1 mm | $h_{fin}$ | 9.3 mm | $T_{water,in}$ | 51.5 - 56.5 °C |
| $Z_{HX}$ | 140 mm | $W_{channel}$ | 4.8 mm | $s_{fin}$ | 1.8 mm | $\dot{Q}_{heater}$ | +/- 10 kW |
| | | $t_{fin}$ | 0.2 mm | $l_{fin}$ | 4 mm | $\dot{m}_{air}$ | 0.36 - 0.55 kgs$^{-1}$ |
| | | $N_{tubes}$ | 13 | $N_{passages}$ | 14 | $T_{air,in}$ | 19.5 - 21.7 °C |

The first step in validating the presented heat exchanger model is to compare numerical results with Ref. [108]. This serves as initial verification that the model produces the expected trends. The overall heat transfer resistance $R$, shown in Figure 4.5, is a measure of the temperature difference between air and water inlets needed to exchange a unit of thermal energy. At design conditions ($\dot{m}_{air}$ = 0.45kgs$^{-1}$, $\dot{m}_{water}$ = 0.54kgs$^{-1}$), approximately 3 K temperature difference are needed to exchange 1 kW of thermal energy from water to air. The error in predicting the overall thermal resistance is below 10% for the whole range with a higher relative and absolute error at high air mass fluxes. The thermal resistance predicted by the proposed model is higher

than the one of Ref. [108]. This can be explained by the lacking offset strip fins at the waterside. By having an offset, the boundary layer is interrupted and restarted at each subsequent fin row, generating turbulence and increasing the heat transfer coefficient. In plain minichannels, the boundary layer reaches a fully developed state and remains as such for the remainder of the channel, resulting in lower heat transfer coefficients. Thus, a higher overall resistance for the present model is expected.

Figure 4.6 shows the predicted air side pressure drop of Ref. [108] and of the presented heat exchanger model. The pressure drop is higher with a maximum error of 14% at the highest air mass flow. The correlation by Manglik and Bergles [92] used in Ref. [108] is the same as the one used in the present work, but data on the air density and viscosity used in Ref. [108] are not given. Additionally, it is unclear from the simplified model in Ref. [108] how the core airspeed is calculated, thus the difference remains unexplained.

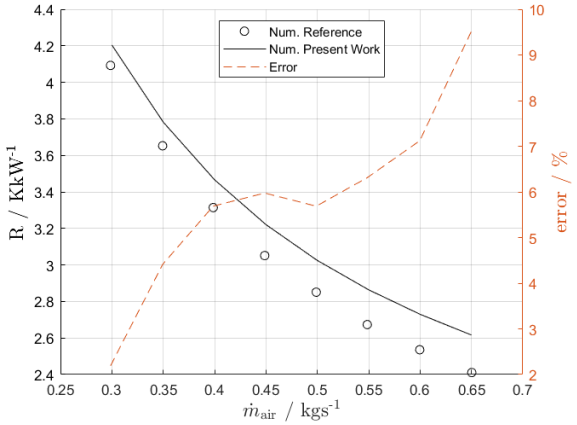


Figure 4.5: Comparison of numerical prediction of overall heat transfer resistance of HX presented in Ref. [108]. $T_{\text{water,in}}$ = 55 °C, $T_{\text{air,in}}$ = 20 °C.

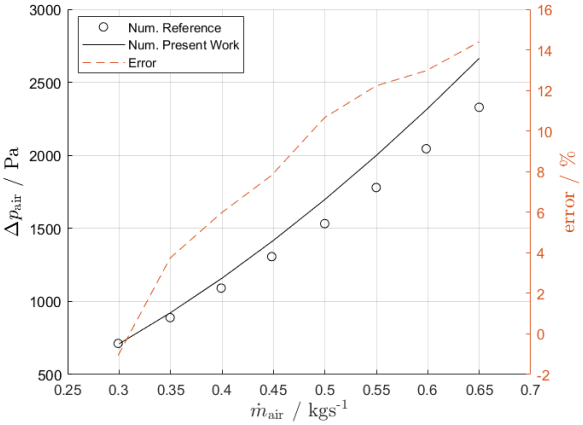


Figure 4.6: Comparison of numerical prediction of air side pressure drop presented in Ref. [108]. $T_{\text{water,in}}$ = 55 °C, $T_{\text{air,in}}$ = 20 °C.

The heat exchanger load found experimentally is shown in Figure 4.7. The inlet temperatures of air and water as reported in Ref. [108] are used to reproduce the results numerically. The numerical method of Hao et al. has an error ranging from +3.5% to -1% while the model presented in the present work can reproduce the experimental results more accurately with an error of +/- 0.5%. This shows that even with the simplification of water side fin characteristics the presented model predicts well the exchanged thermal energy. The experimental air side pressure drop is shown in Figure 4.8. The present model underestimates the pressure drop by more than 30%. It is unclear how two correlations, for heat transfer coefficient and pressure drop, developed and validated within the same research scope [92] can have such varying accuracy on the same heat exchanger geometry. As the details of data reduction and measurement techniques are not reported in Ref. [108], it is impossible to identify with certainty where the discrepancy comes from. Additionally, the numerical results of Hao et al. are not reported either, and an even higher error is expected as the pressure drop was estimated to be even lower than the present model in Figure 4.6. It is speculated that interactions of the boundary layer along the walls of the test section with the heat exchanger core might be a source of inaccuracy, given the small dimensions of the heat exchanger frontal area. It is possible that with larger cores and shorter inlet ducts, as would be the case in a ram air cooling duct, this effect is reduced. Nevertheless, the interaction of the heat exchanger core with the surrounding duct walls and its effect on air pressure drop needs to be properly investigated for detailed ram air duct design.

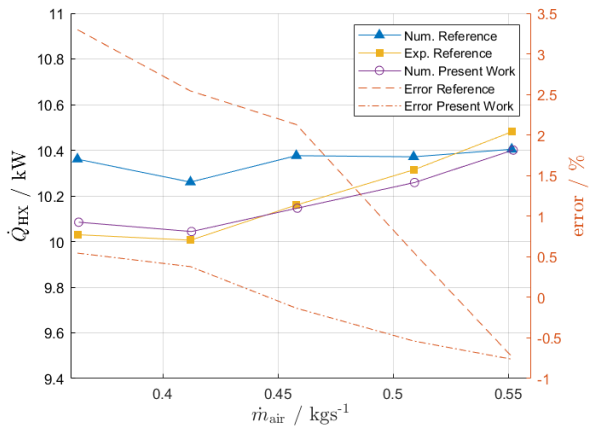


Figure 4.7: Comparison of experimental results and numerical predictions of heat duty presented in Ref. [108].

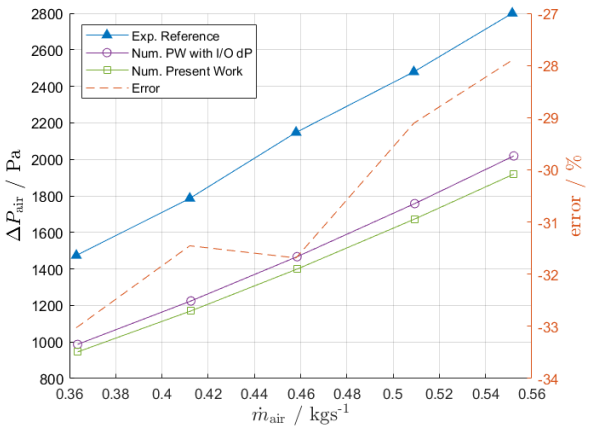


Figure 4.8: Comparison of experimental results of air side pressure drop presented in Ref. [108].

## 4.3. VCS AND AIR COOLED CONDENSER FOR FUEL CELL THERMAL MANAGEMENT

A final effort to validate the presented method is to try and reproduce the findings of Reichler [25]. Reichler investigated the use of flow boiling to increase the cooling capacity of a fuel cell thermal management system for vehicle applications. In Ref. [25], the main heat exchanger size and air mass flow are given by the car manufacturer as fixed constraints. Different fluids for use in both pumped multi-phase and vapour compression systems are identified and evaluated. R245FA is found to be a promising candidate and is chosen as a reference for validation of the methods presented in the present work. The heat exchanger used in Ref. [25] is of the louvred fin type. This type of fin, often used in automotive applications, has a higher heat transfer potential per unit length, but a higher pressure drop. The correlations for this fin were developed by Chang & Wang [109] and the geometry is presented in Figure 4.9. The focus of this validation step is not the air-side correlations, but rather the representation of relevant trends in enhancing fuel cell cooling through VCS systems.

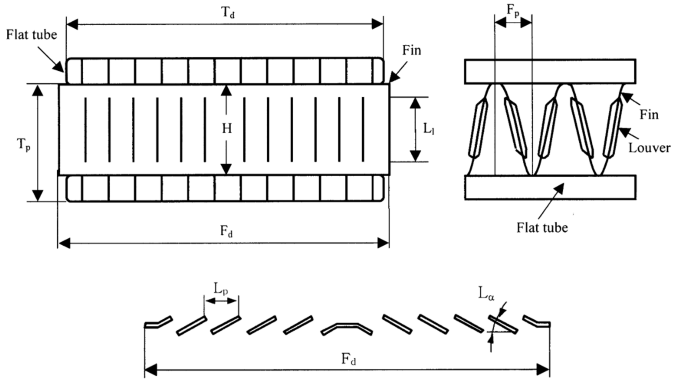


Figure 4.9: Louvred fin geometry reproduced from Ref. [110].

To evaluate the effectiveness of different fluids and systems, Reichler [25] uses a conventional, ethyl-glycol water based, single-phase cooling system as reference. The relevant geometrical parameters and operating conditions for the reference heat exchanger are given in Table 4.3. The experimental and numerical results on the performance of the reference heat exchanger are shown in Figure 4.10. The numerical results of the method in the present work are also shown in the same figure. As can be seen, both numerical methods underestimate the heat exchanger duty. Over the range of air mass flows, the present numerical method is in better agreement with experiments than the method of Reichler, with a maximum error of -5% and -10% respectively. The air side pressure drop in Figure 4.11 is calculated with the present method as it is not

explicitly given in Ref. [25]. In the vehicle application of Reichler, the air is driven by a fan behind the heat exchanger and the fan power is approximated with the same approach as the pump in subsection 3.7.1 as in

$$P_{\text{fan}} = \frac{\dot{m}_{\text{air}} \Delta p_{\text{air}}}{\rho_{\text{air}}}. \tag{4.1}$$

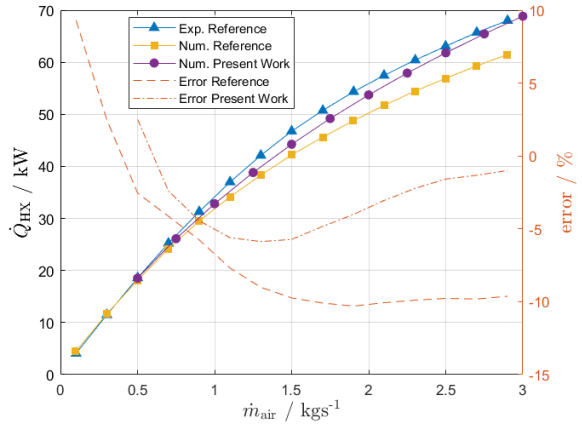


Figure 4.10: Water cooled main heat exchanger duty. Comparison of experimental and numerical results of Ref. [25].

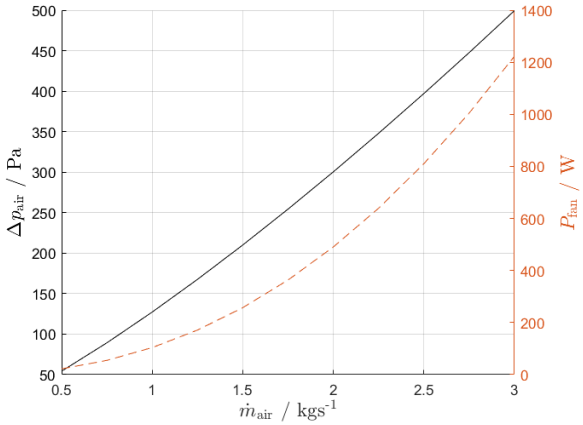


Figure 4.11: Water cooled main heat exchanger air side pressure drop and fan power as calculated by present work model.

Table 4.3: Geometrical and Operational Parameters of the main heat exchanger in used in Ref. [25].

| Overall Geometry | |
|---|---|
| $W_{\text{HX}}$ | 645 mm |
| $H_{\text{HX}}$ | 572 mm |
| $Z_{\text{HX}}$ | 38 mm |

| Water Tubes | |
|---|---|
| $h_{\text{tube}}$ | 2 mm |
| $t_{\text{tube}}$ | 0.1 mm |
| $W_{\text{channel}}$ | 1.8 mm |
| $t_{\text{fin}}$ | 0.1 mm |
| $N_{\text{tubes}}$ | 57 |

| Air Fins | |
|---|---|
| $t_{\text{fin}}$ | 0.1 mm |
| $H_{\text{fin}}$ | 8 mm |
| $F_{\text{p}}$ | 1.54 mm |
| $L_{\text{l}}$ | 6.8 mm |
| $L_{\alpha}$ | 28° |
| $L_{\text{p}}$ | 1 mm |
| $N_{\text{finned}}$ | 58 |

| Operating Parameters | |
|---|---|
| $\dot{m}_{\text{air}}$ | 2 kgs$^{-1}$ |
| $T_{\text{air,in}}$ | 40 °C |
| $\dot{m}_{\text{water}}$ | 2.5 kgs$^{-1}$ |
| $T_{\text{water,in}}$ | 80 °C |

| Op. Parameters - R245FA | |
|---|---|
| $\dot{m}_{\text{coolant}}$ | 0.45 - 0.6 kgs$^{-1}$ |
| $T_{\text{comp,in}}$ | 80 °C |

The second validation step entails reproducing the cooling enhancement of a VCS system. For this purpose, the numerical model used by Reichler and shown in Figure 4.13 is used. The model has R245FA refrigerant input at 80 °C and variable mass flow. The refrigerant is pressurized by a compressor with efficiency $\eta_{\text{comp}} = 0.6$ and reaches the condenser inlet temperatures as reported in Table 4.4. The inlet temperature is dependent on the compressor pressure ratio. The saturation temperature is also reported, this is the temperature that the refrigerant reaches after it is desuperheated in the initial section of the heat exchanger.

The model used in the present work differs from the one used in Ref. [25] in two ways. The first is that the model in the present work was developed for design purposes of desuperheating and condensing phases. As such, it is unable to accurately predict the heat transfer rate when the refrigerant condenses completely and a large part of the heat exchanger is filled with subcooled liquid. It is expected that in this situation, an overestimation of the heat exchanger duty occurs, as the heat transfer coefficient and the $\epsilon - NTU$ relation for condensation are higher than for subcooling.

The second difference is that the condenser used by Reichler utilizes a multi-pass configuration with varying amounts of parallel channels per pass. This strategy ensures that the flow velocity in the tubes remains high even with a decreasing density during condensation. When the condensation is incomplete, this will result in a higher heat exchanger duty for the model of Reichler than the one used in the present work. An example schematic of a multipass condenser is given in Figure 4.12.

Finally, in this simplified analysis, only the compressor and condenser are considered as shown in Figure 4.13.

Table 4.4

| $PR_{comp}$ | $T_{cond,in}$ | $T_{cond,sat}$ |
|---|---|---|
| 1.1 | 89 °C | 84 °C |
| 1.3 | 96.5 °C | 91 °C |
| 1.5 | 103 °C | 97 °C |

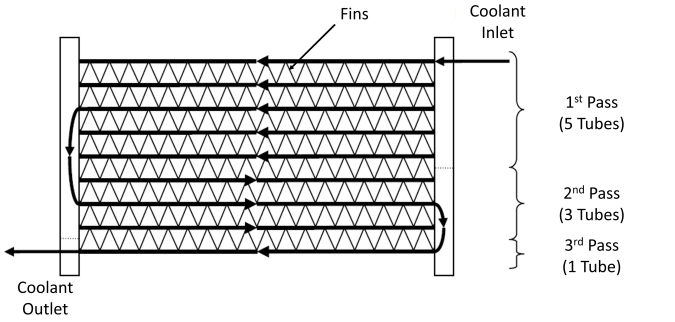


Figure 4.12: Multi-pass condenser example reproduced from Ref. [25].

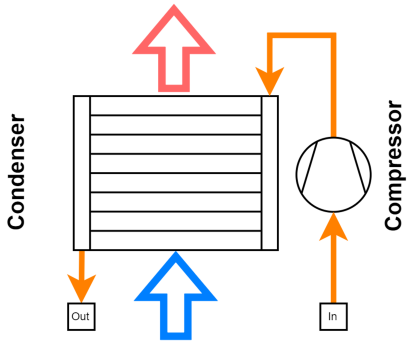


Figure 4.13: Numerical model of compressor and condenser used in Ref. [25].

In Figure 4.14, the condenser duty and compressor power as found by Reichler are compared with the model presented in this work. As can be seen, the compressor power is in perfect agreement with Reichler while the condenser duty is off. More precisely, the heat transferred by the condenser is overestimated at low coolant mass flows and underestimated at high coolant mass flows by the present model. This is true for all compressor pressure ratios. The difference is expected, given the limitations of the present model in simulating off design subcooled outlet conditions and multiple passes.

To quantify the cooling enhancement offered by a VCS system, Reichler introduces the effective cooling duty parameter $\dot{Q}_{eff}$, defined as

$$\dot{Q}_{eff} = \dot{Q}_{cond} - \dot{Q}_{stack,extra} - W_{comp}. \tag{4.2}$$

The compressor power added to the coolant, and the additional thermal energy released by the fuel cell when higher power demand is needed to drive the compressor, are subtracted from the condenser duty. The resulting effective duty takes into account the price that is paid for the enhancement and is reported in Figure 4.15. As can be seen, there is an optimal compressor power, and thus coolant mass flow, for each pressure ratio, that results in the highest effective cooling duty. This trend is also reproduced by the present model, although due to limitations, the effective heat duty is lower as is the optimal compressor power.

The findings, that an enhancement of cooling duty is achievable when employing vapor compression systems as a means to cool fuel cells, are thus confirmed. This enhancement comes at a cost. For an effective cooling duty of 70 kW, an additional 6 kW of power needs to be produced by the fuel cell, and the respective waste thermal energy needs to be rejected by the condenser.

Another strategy would be to act on the air side. In Figure 4.11, it can be seen how an increase in air mass flow to reach a cooling duty of 70 kW roughly entails a fan power of 1.2 kW. Although the fan model is very simplistic and no efficiency is used, it seems that increasing cooling duty by acting on the air side could be less expensive, in terms of extra power loss, than using a compressor on the coolant side. Given that it is not clear if a VCS system might be the right solution to achieve better cooling performance in vehicles, it is even more interesting to explore its application in airplanes.

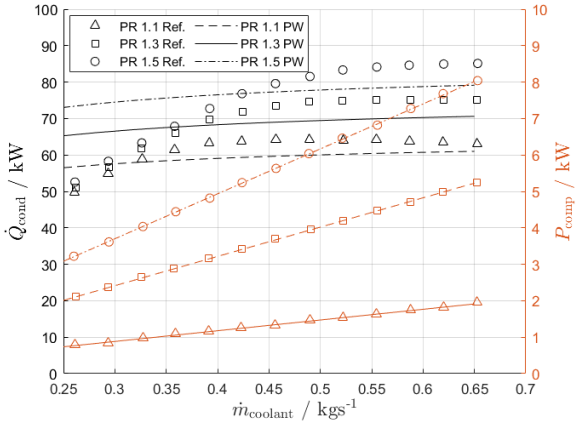


Figure 4.14: Condenser duty and compressor power comparison of Ref. [25]. PW = Present Work.

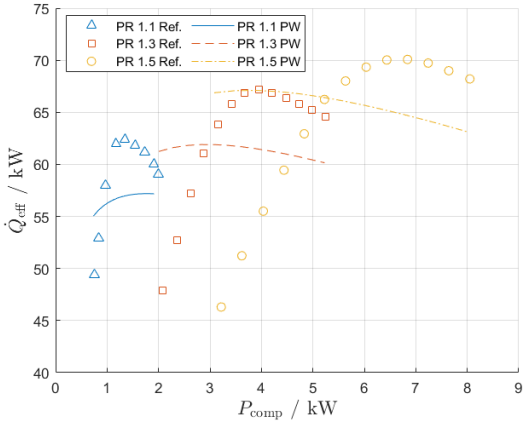


Figure 4.15: Effective cooling duty comparison of Ref. [25]. PW = Present Work.

# 5

# RESULTS

## 5.1. FUEL CELL COOLING CHANNEL ANALYSIS

The fuel cell cooling channels are analyzed to highlight the interaction between the cooling fluid and channel geometry. The cooling channels are first analyzed from a high-level perspective, in which the average conditions in the cooling channels are calculated. This allows for exploring different channel geometries and visualizing the design space easily. Additionally, a single-channel geometry is discussed in more detail and the axial evolution of different physical quantities is shown. This allows for highlighting the peculiarities of the flow boiling phenomenon.

### 5.1.1. 0D GEOMETRICAL DESIGN SPACE

The cooling channel geometries explored are combinations of $H_{\text{ch}}$ and $W_{\text{ch}}$ between 0.5 and 1.5 mm. From the design specifications of a single fuel cell module in section 3.12 the geometrical and thermal conditions in Table 5.1. In the same table, the resulting conditions for a single channel with dimensions 0.75 mm by 0.75 mm are presented as well.

Table 5.1: Resulting geometrical and thermal conditions for a single cell. Conditions for a single 0.75 m by 0.75 m channel are included.

| Results - Cell | |
|---|---|
| $N_{\text{cells}}$ | 357 |
| $A_{\text{cell}}$ | 1600 cm2 |
| $W_{\text{cell}}$ | 200 mm |
| $L_{\text{cell}}$ | 800 mm |
| $\dot{Q}_{\text{cell}}$ | 1365 W |

| Results - 0.75x0.75 mm Channel | |
|---|---|
| $N_{\text{ch}}$ | 133 |
| $D_h$ | 0.75 mm |
| $A_{\text{ch,walls}}$ | 24 cm2 |
| $q_{\text{ch}}$ | 4278 W/m2 |

The resulting channel heat flux is shown in Figure 5.1. It is relatively low compared to micro- and minichannel flow boiling applications where heat fluxes can reach orders of magnitude above 100 $\text{kW m}^{-2}$, but it is in the range expected for fuel cells and comparable to Ref. [27]. The higher heat fluxes reported in Ref. [27] are due to the choice of very wide and shallow channels ($W_{\text{ch}}$ up to 8 mm and depth down to 0.421 mm) which also in this work are related to higher heat fluxes

#### REFERENCE: SINGLE-PHASE ETHYL-GLYCOL WATER

As reference coolant for conventional single-phase liquid cooling an ethyl-glycol water mixture of 50% concentration (EGW50) is used. The constraint to determine the mass flow rate needed to cool the fuel cell stack is based on the allowed temperature difference, which is set to 10 K. The inlet temperature is set to 70 °C which results in a mass flow rate to cool the whole stack of 14.04 $\text{kg s}^{-1}$. The resulting mass flux $G$ for each channel geometry is given in Figure 5.2. As expected it is dependent only on the channel height as the overall portion of cell area that is covered directly by a cooling channel is always constant (50 %) due to the uniform channel spacing.

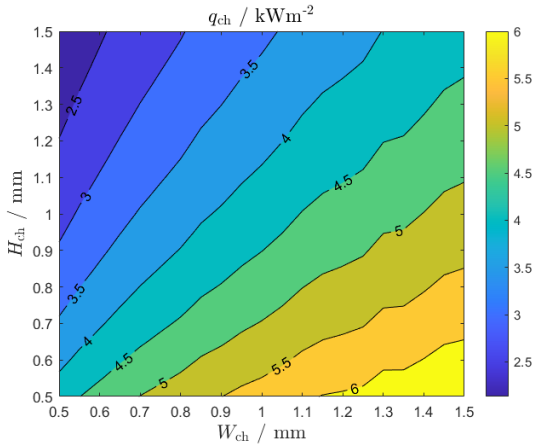


Figure 5.1: Cooling channel heat flux for different geometries.

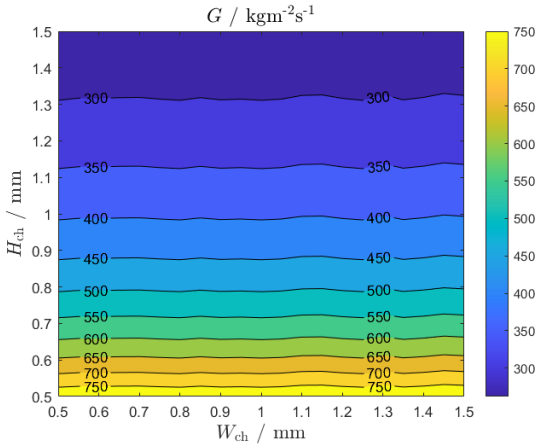


Figure 5.2: Mass flux of EGW50 for different geometries.

The heat transfer coefficient for the single-phase case is the most important quantity that serves as a reference for novel concepts. The heat transfer coefficient, shown in Figure 5.3 with values ranging from 1000 to 2800 $\mathrm{W\,m^{-2}\,K^{-1}}$ over the whole design space with a value of around 1500 $\mathrm{W\,m^{-2}\,K^{-1}}$ at the 1x1 mm channel. The flow is laminar with $Re$ below 500 (Figure 5.4).

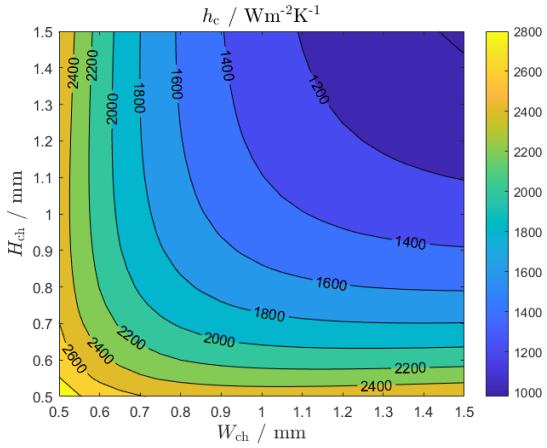


Figure 5.3: Heat transfer coefficient of EGW50 for different geometries.

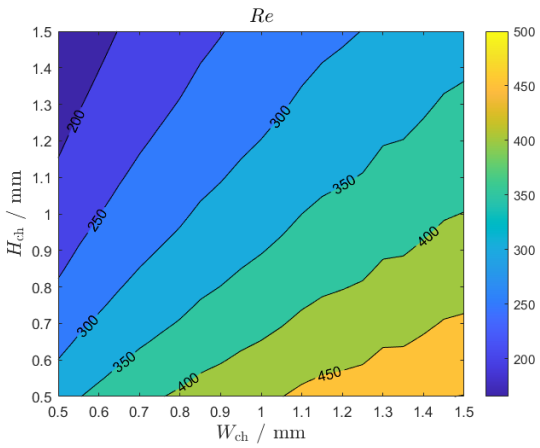


Figure 5.4: Reynolds number of EGW50 for different geometries.

The maximum cooling channel wall temperature can be found at the outlet due to the temperature increase of the coolant. The heat transfer coefficient influences the wall temperature together with the heat flux as in Equation 3.52. The maximum temperature encountered in the whole design space is 84 °C as shown in Figure 5.5. As the heat transfer coefficient for the laminar flow of EGW is constant, the wall temperature at the inlet is equal to the wall at the outlet minus 10 K. The pressure drop of the coolant (Figure 5.6) is primarily a function of hydraulic diameter and mass flux thus channels with lower height are negatively affected and have a larger pressure drop.

### TWO-PHASE METHANOL

An alternative to single-phase cooling with EGW is flow boiling with Methanol. Methanol has a high latent heat of evaporation resulting in only 0.57 $\mathrm{kg\,s^{-1}}$ need to cool the stack with an outlet vapour quality of 0.8. This already points to potential weight savings in piping and coolant mass. The inlet temperature of methanol is set at 80 °C and a more detailed explanation for this choice is given in subsection 5.1.2. Due to the low mass flow rate requirement, the mass flux in the cooling channels is low between 10 and 32 $\mathrm{kg\,s^{-1}\,m^{-2}}$ (Figure 5.7). The two-phase boiling heat transfer coefficient is slightly higher than the one of EGW with an average of 2000 $\mathrm{W\,m^{-2}\,K^{-1}}$ at 1x1 mm. In Figure 5.8 only the heat transfer coefficient at the arithmetic mean vapour quality of 0.4 is shown as the development of $x_{vq}$ is linear.

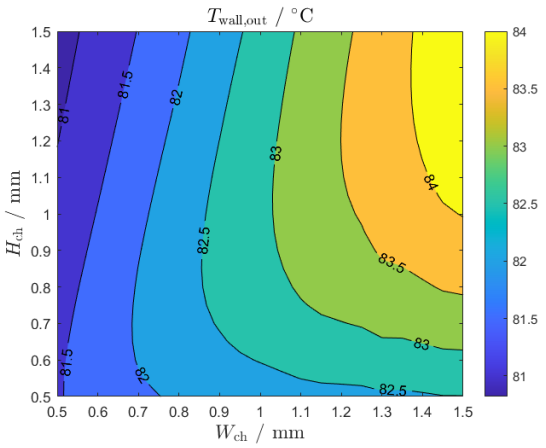


Figure 5.5: Outlet wall temperature of EGW50 for different geometries.

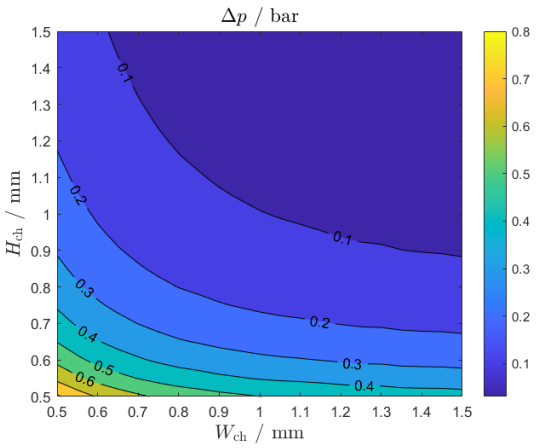


Figure 5.6: Pressure drop of EGW50 for different geometries.

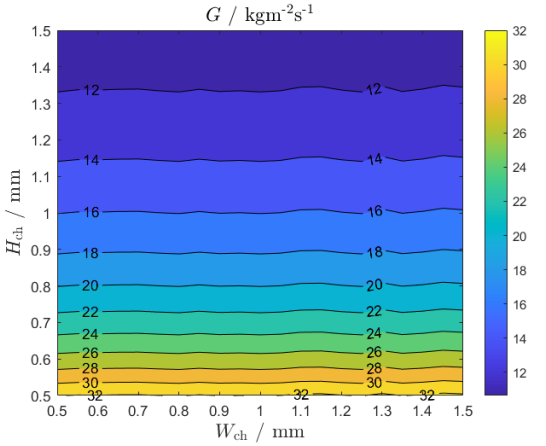


Figure 5.7: Mass flux of methanol for different geometries.

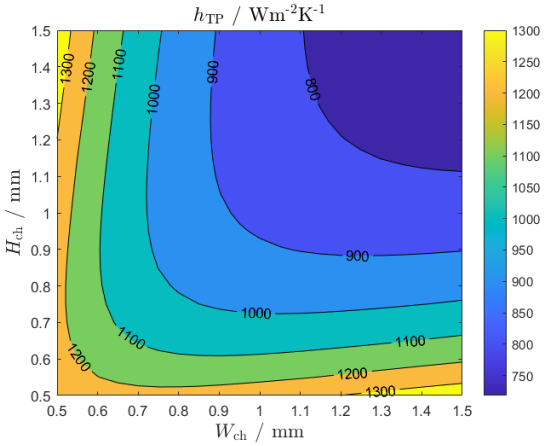


Figure 5.8: Heat transfer coefficient of methanol at $x_{vq}$ = 0.4 for different geometries.

The Reynolds number of methanol shown in Figure 5.13 is lower than 100 in the whole design space meaning that nucleate boiling is the dominant heat transfer mechanism.

The nucleate boiling two-phase heat transfer coefficient is based on the single-phase liquid-only heat transfer coefficient $h_{c,LO}$, and primarily on the boiling number Bo. As only a single value of $x_{vq}$ is looked at in this preliminary analysis, the influence of the convective number Co on the heat transfer coefficient is not apparent. A 1D analysis of the channel shows the impact of Co and is discussed in subsection 5.1.2.

For methanol, $h_{c,LO}$, shown in Figure 5.9, is lower than water in the laminar regime due to the lower thermal conductivity (0.2 vs 0.6 $Wm^{-1}K^{-1}$). The boiling number is a function of $q_{ch}$, $h_{lv}$ and $G$. As $q_{ch}$ and $h_{lv}$ are constants in this analysis, only G influences the boiling number and this is reflected in its trend as seen in Figure 5.10. Interestingly, as the mass flow rate is fixed for a given heat load and exit vapour quality, $G$ is influenced purely by the geometry of the duct. Thus, for nucleate boiling-dominated flows, $Bo$ is a function of geometry only. It is apparent that the influence of $h_{c,LO}$ is dominating the two-phase heat transfer coefficient as higher $h_{TP}$ are reached at smaller channel cross-section despite the decreasing $Bo$.

Additionally, from the trends presented in Ref. [80] and shown in Figure 3.6, it is expected that $h_{TP,NBD}$ decreases with increasing vapour quality. This might lead to the temperature not being uniform and increasing at the outlet. Figure 5.11 and Figure 5.12 show that indeed the wall temperature tends to increase at the outlet due to a decreasing heat transfer coefficient. In this preliminary channel design exploration, the effect of pressure drop on the saturation temperature is not taken into account, thus the bulk flow is isothermal and the rise in wall temperature can be attributed solely to the changing heat transfer coefficient. In subsec-

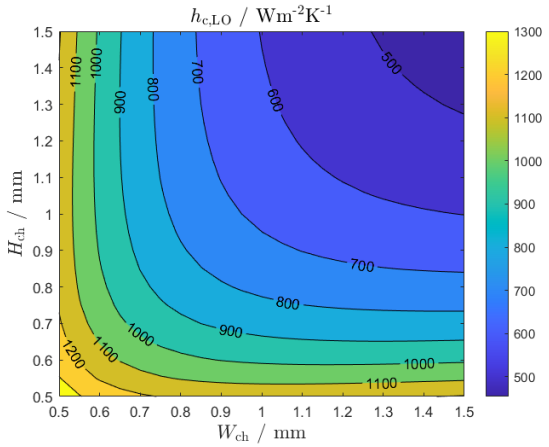


Figure 5.9: Liquid-only heat transfer coefficient of methanol for different geometries.

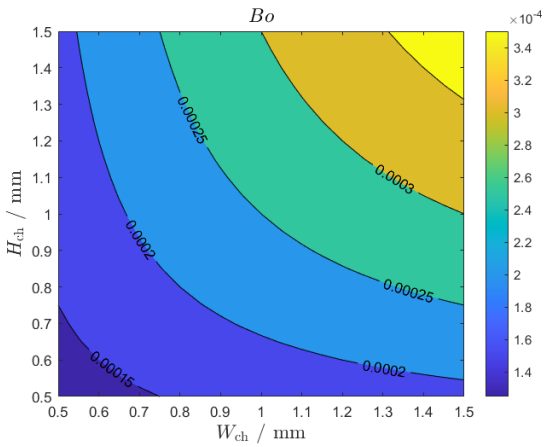


Figure 5.10: Boiling number of methanol for different geometries.

tion 5.1.2 the effect of the pressure gradient due to frictional losses on the saturation temperature is taken into account and its effects are highlighted. The pressure drop calculated with the pressure gradient evaluated at the average vapour quality of 0.4 is shown in Figure 5.14 and it shows that despite the much lower mass flow, the pressure drop is comparable to the EGW case. The two phase multiplier calculated with the Firedel correlation [86] increases the liquid-only pressure drop by two orders of magnitude as it lies between 100 and 116 over the whole design space. This is attributed to the specific volume change from liquid to vapour that for methanol is a factor of 345.

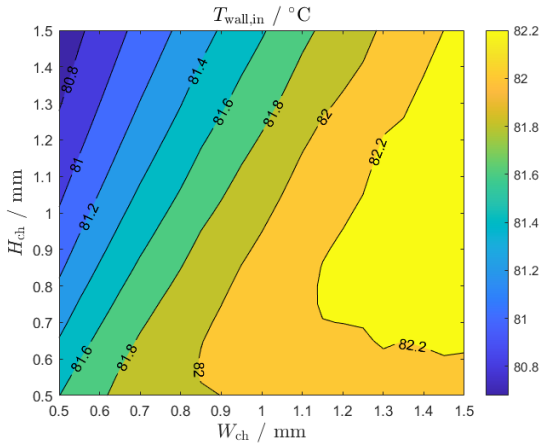


Figure 5.11: Wall temperature at cooling channel inlet, operating with methanol, for different geometries.

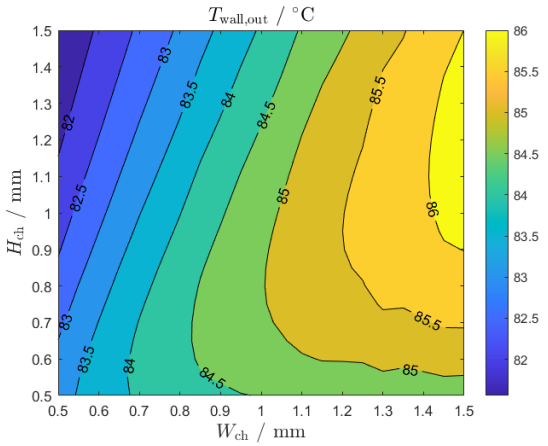


Figure 5.12: Wall temperature at cooling channel outlet, operating with methanol, for different geometries.

The range of possible inlet and outlet conditions of the coolant to ensure good boiling behaviour is limited by the onset of nucleate boiling and dry-out conditions. At the inlet, the flow might enter in subcooled liquid state, especially in pumped multi-phase systems. As Figure 5.9 shows, the heat transfer coefficient for only the liquid without influence of boiling is less than half of the one encountered in boiling conditions. Thus, hot spots might arise at the inlet if boiling is not occurring. Due to the thermal boundary layer that develops when the liquid is in contact with the wall, it is possible that the conditions for nucleation of bubbles exist in the boundary layer before the bulk flow has reached the saturation temperature. The onset of nucleate boiling can thus happen in subcooled liquids and the bulk flow temperature at which this happens is calculated with Equation 3.60 and Equation 3.61. As Figure 5.15 shows, the flow can be subcooled between 2 and 8 K. This will be shown to play an important role for system level design in section 5.2.

Another important limiting factor is the vapour quality at dry-out incipience. In fact, when dry-out occurs, the heat transfer coefficient is reduced dramatically and hot spots can occur. The estimated DI vapour quality

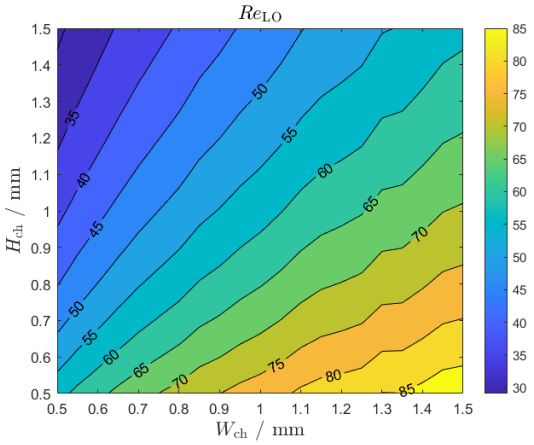


Figure 5.13: Liquid only Reynolds number of methanol for different geometries.

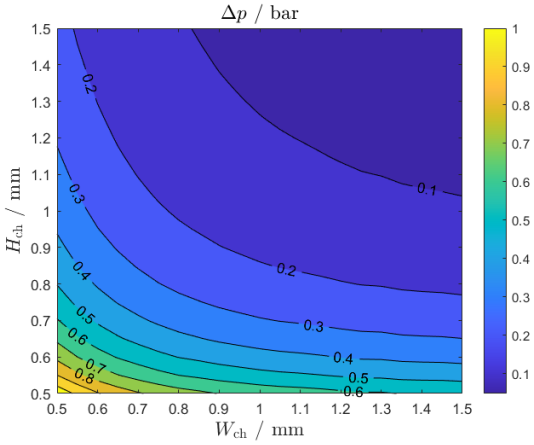


Figure 5.14: Pressure drop of methanol averaged at $x_{vq} = 0.4$ for different geometries.

is shown in Figure 5.16 and it is clear that 0.8 is too high for an outlet vapour quality. For methanol, $x_{vq,out}$ of 0.7 will be used in subsequent simulations.

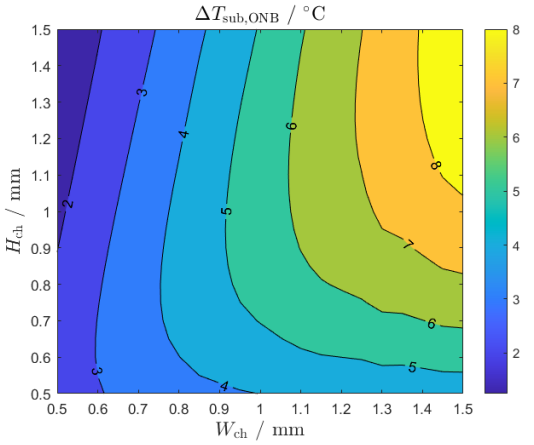


Figure 5.15: Possible degree of subcooling at the onset of nucleate boiling of methanol for different geometries.

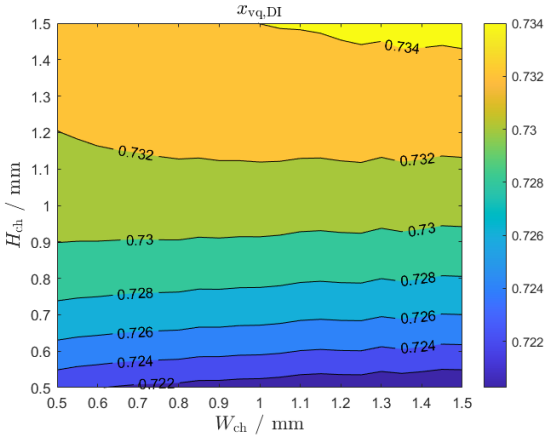


Figure 5.16: Vapour quality at dryout incipience of methanol for different geometries.

### TWO-PHASE R1233ZDE

Another fluid that could be used in the flow boiling cooling of fuel cells is R1233ZDE. This fluid is characterized by a lower latent heat of evaporation and thus has a higher mass flow requirement to cool the fuel cell stack. With 3.8 $kg s^{-1}$ it has a lower mass flow rate requirement than water for an outlet vapour quality of 0.8. The inlet temperature used for R1233ZDE is 77 °C and lower than methanol as it has a lower heat transfer coefficient. The mass flux is thus higher reaching 200 $kg s^{-1} m^{-2}$ at low channel heights (see Figure 5.17). The resulting heat transfer coefficient in Figure 5.18, is lower than both water and methanol reaching only 1000 $W m^{-2} K^{-1}$ for a 1x1 mm channel. This is because the boiling number remains unchanged for a given geometry and the liquid-only heat transfer coefficient is lower due to the lower thermal conductivity of R1233ZDE which is 0.0679 $W m^{-1} K^{-1}$.

The Reynolds number, shown in Figure 5.23, for the whole flow taken as liquid is in the laminar region between 500 and 900 and is thus outside the nucleate boiling dominated regime. This enhances the two-phase heat transfer coefficient but not significantly. This is because the ratio of vapour to liquid density, which influences the convective number Co, is relatively high. In the correlation by Kandlikar [71], Co is to a negative power, meaning low values result in higher $h_{TP}$. Low Co values are proportional to low $\rho_v/\rho_l$ values. The reason being that when the liquid changes phase, a vapour that has a relatively low density will occupy more volume and thus will flow faster in the channel, enhancing convection and thus convective flow boiling.

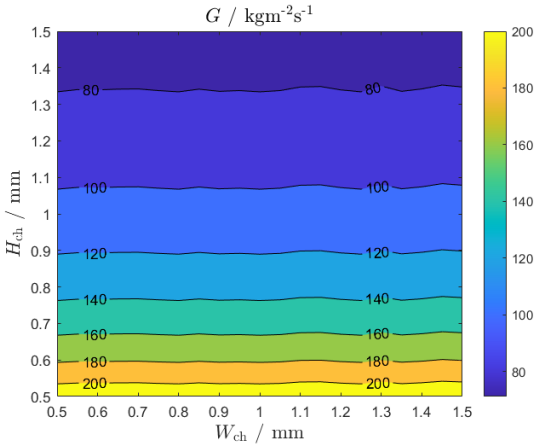


Figure 5.17: Mass flux of R1233ZDE for different geometries.

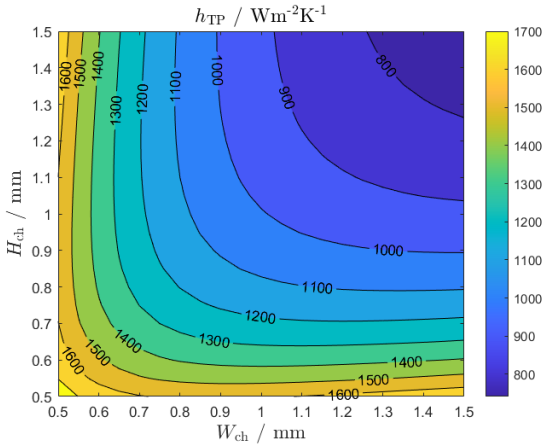


Figure 5.18: Heat transfer coefficient of R1233ZDE at $x_{vq} = 0.4$ for different geometries.

R1233ZDE has $\rho_v/\rho_l$ ratio of one order of magnitude higher than methanol (0.0287 vs 0.0029) and thus the enhancement of $h_{TP}$ by convection is smaller.

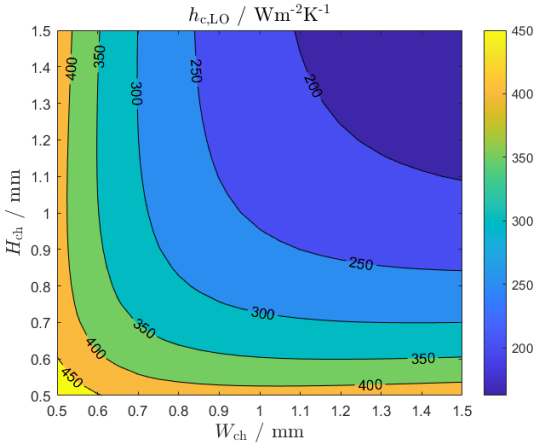


Figure 5.19: Liquid-only heat transfer coefficient of R1233ZDE for different geometries.

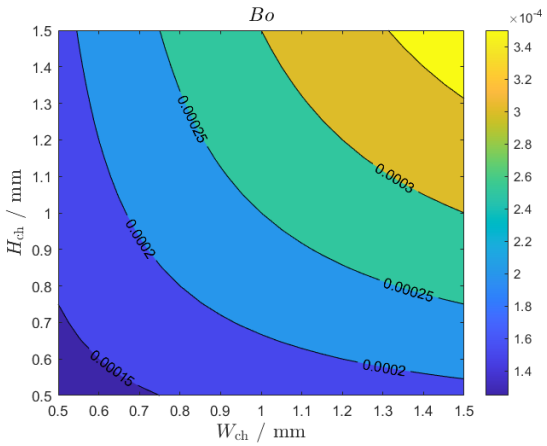


Figure 5.20: Boiling number of R1233ZDE for different geometries.

As the flow regime is convective, the heat transfer coefficient tends to increase with vapour quality. This is reflected in the wall temperature, which decreases by 1 to 2 K.

The degree of subcooling at which nucleation occurs is very high for R1233ZDE. This characteristic of the fluid can be attributed to the lower surface tension, which determines the overpressure inside the bubble for nucleation to occur. In fact R1233ZDE has a surface tension which is an order of magnitude lower than methanol (0.0081 vs 0.0174 $\mathrm{N\,m^{-1}}$). A high allowable degree of subcooling at the inlet allows for easier design of pumped multi-phase systems as will be explained in section 5.2.

Finally, the vapour quality at dry-out incipience is slightly higher than methanol and allows to keep 0.8 as design $x_{vq,out}$.

The pressure drop of R1233ZDE is approximately half of that of methanol over the design space. Despite the larger mass flux of R1233ZDE and the higher liquid-only pressure gradient, the overall pressure drop of the two-phase flow is lower. For the same reason of the lesser enhancement of convective boiling, also in this case the lower pressure drop is due to the small difference between the density of the vapour and liquid phases. In fact, the two-phase multiplier of R1233ZDE is only between 16 and 18 over the design space.

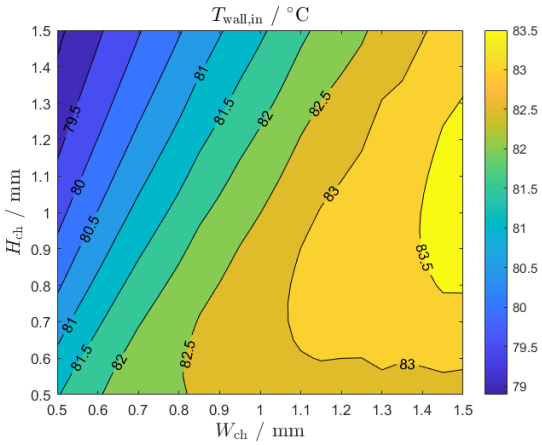


Figure 5.21: Inlet wall temperature of cooling channel operating with R1233ZDE for different geometries.

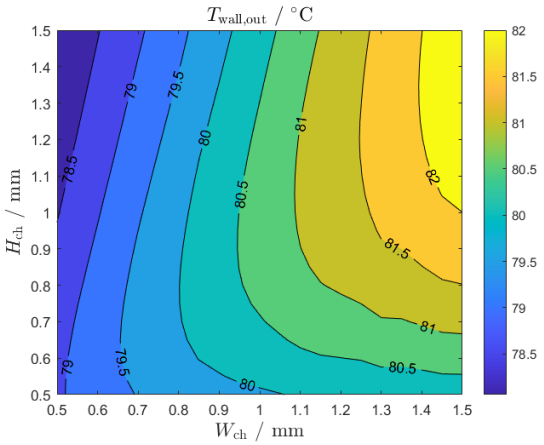


Figure 5.22: Outlet wall temperature of cooling channel operating with R1233ZDE for different geometries.

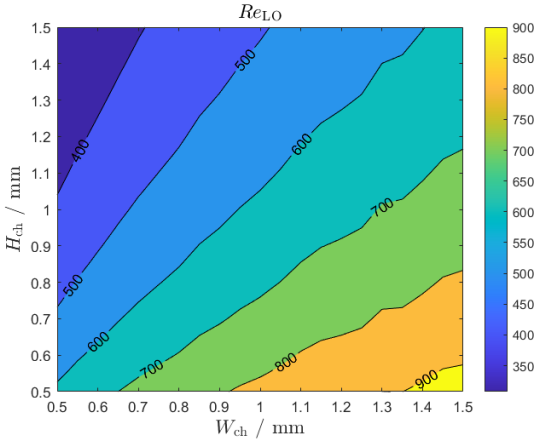


Figure 5.23: Liquid only Reynolds number of R1233ZDE for different geometries.

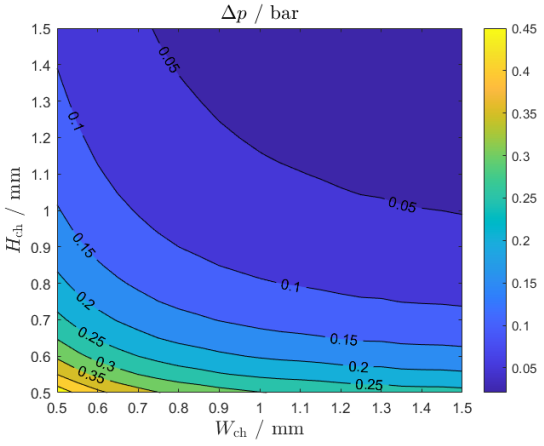


Figure 5.24: Pressure drop of R1233ZDE averaged at $x_{\text{vq}} = 0.4$ for different geometries.

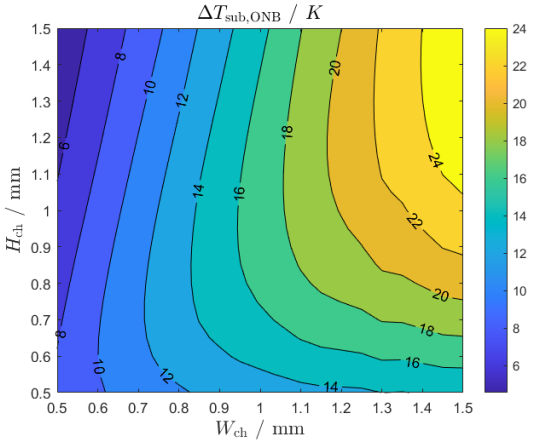


Figure 5.25: Possible degree of subcooling at the onset of nucleate boiling of R1233ZDE for different geometries.

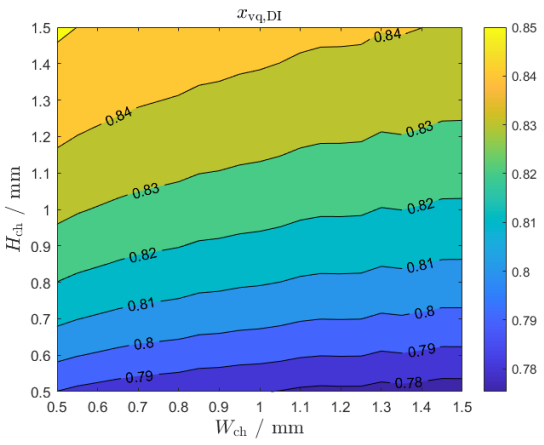


Figure 5.26: Vapour quality at dryout incipience of R1233ZDE for different geometries.

### 5.1.2. 1D AXIAL EVOLUTION

The square channel of 0.75x0.75 mm dimensions is taken as a reference for a more detailed analysis. In this 1D analysis, the effect of the frictional pressure gradient is taken into account to show how temperature gradients in the channel wall are present in flow boiling.

#### REFERENCE: SINGLE-PHASE ETHYL-GLYCOL WATER

The axial evolution of wall temperature and fluid temperature of ethyl-glycol water is linear. The $\beta$ parameter is found to be 0.035, thus axial conduction effects in the wall can be neglected. The pressure gradient does not affect the liquid temperature, and it affects the thermal conductivity only slightly with a 0.85% increase for a $\Delta T$ of 10 K. This results in an almost constant temperature offset between the bulk wall and the wall as shown in Figure 5.27. The pressure along the channel together with the slightly increasing $h_c$ is shown in Figure 5.28. An inlet pressure of 1.5 bar is used in this analysis to avoid sub-atmospheric pressures at the channel outlet but does not influence the results as for incompressible fluids all thermodynamic or transport properties are a function of temperature only. The temperature gradient that is typical of cooling based on sensible enthalpy is a feature that helps evaporate the produced liquid water in the gas channels and thus reduces the overall cooling duty.

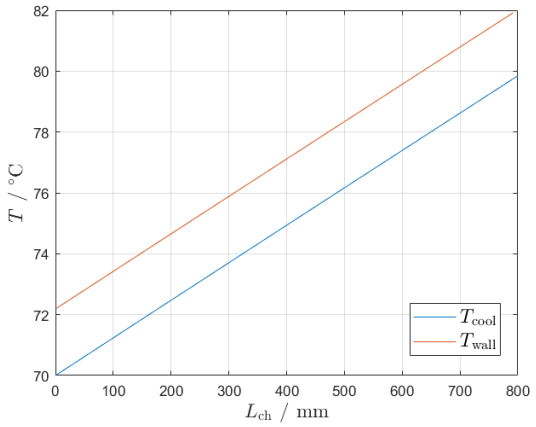


Figure 5.27: Wall and coolant temperature evolution of EGW 50 in 0.75x0.75 mm channel.

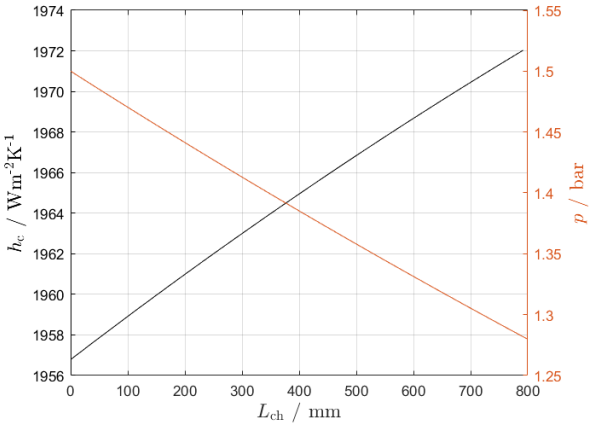


Figure 5.28: Heat transfer coefficient and pressure evolution of EGW 50 in 0.75x0.75 mm channel.

#### TWO PHASE METHANOL

The wall temperature evolution of methanol is influenced by both the varying heat transfer coefficient and the reduction in saturation temperature due to the frictional pressure drop. The effect of uncertainty on the heat transfer coefficient due to the large error bounds that empirical two-phase heat transfer coefficient correlations have is highlighted with uncertainty bounds of +/- 50%. In Figure 5.29 the wall temperature evolution is shown. $T_{wall}$ can vary between 3 and 7 K from inlet to outlet. The temperature of the saturated liquid decreases by 6 K as the pressure drops from 1.81 to 1.44bar, a decrease of almost 21%. Although the saturation temperature decreases by an amount comparable to the EGW case (10 K), the heat transfer coefficient is low in the nucleate boiling regime and the temperature of the wall does not follow the saturation temperature.

The effect of decreasing the vapour quality at the outlet is shown in Figure 5.30. As the available latent enthalpy of evaporation decreases due to the $x_{vq,out}$ constraint, the mass flow required increases and the liquid-only Reynolds number surpasses 100 entering the convective flow boiling regime. The pressure drop is increased to almost 30% with the outlet pressure reaching 1.3 bar and the saturation temperature 70 K. The heat transfer coefficient is also enhanced and the wall temperature difference is decreased. In this condition both the wall and coolant have a temperature gradient of around 10 K.

The heat transfer coefficient for the $x_{vq,out} = 0.7$ and $x_{vq,out} = 0.35$ cases is shown in Figure 5.31. The effect of convective boiling is clearly seen in the $x_{vq,out} = 0.35$ case as the heat transfer coefficient rises along the channel length with increasing vapour quality. The lower $h_{TP}$ at the entrance of the channel for $x_{vq,out} = 0.35$ is due to the entrance still being dominated by nucleate boiling. In this region, the higher mass flux induced by

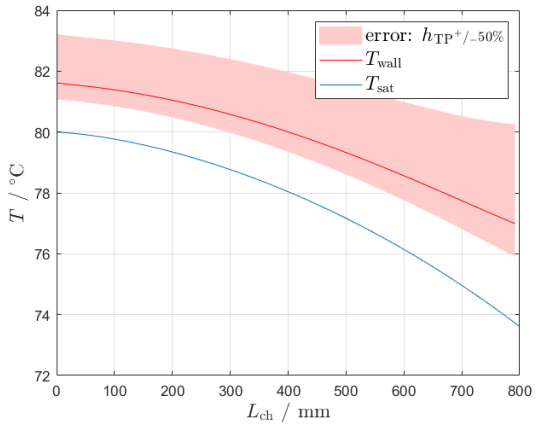


Figure 5.29: Wall and coolant temperature evolution of methanol in 0.75x0.75 mm channel with $x_{vq,out} = 0.7$.

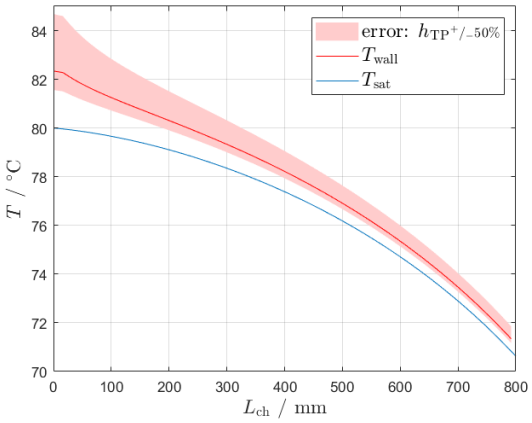


Figure 5.30: Wall and coolant temperature evolution of methanol in 0.75x0.75 mm channel with $x_{vq,out} = 0.35$.

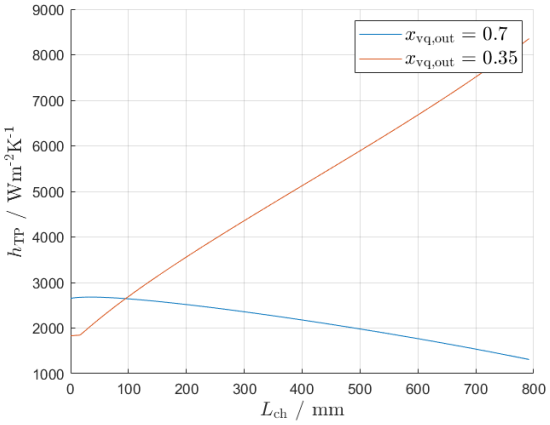


Figure 5.31: Two-phase heat transfer coefficient of methanol at $x_{vq,out} = 0.35$ and $x_{vq,out} = 0.7$.

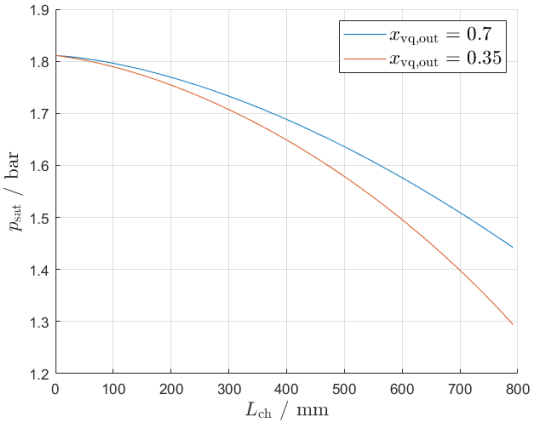


Figure 5.32: Presure drop of methanol at $x_{vq,out} = 0.35$ and $x_{vq,out} = 0.7$.

the higher mass flow rate reduces the boiling number and with it the nucleate boiling heat transfer coefficient. When $h_{TP}$ is high, the effect of its uncertainty on wall temperature is low.

### TWO PHASE R1233ZDE

Comparing the wall temperature of R1233ZDE to methanol two things are apparent. The first is that the pressure drop over the channel does not affect the saturation pressure of the fluid much. The pressure drop of R1233ZDE, shown in Figure 5.36, is both lower in magnitude, ≈ 0.2 bar, and in percentage, -3.3%, than the pressure drop of methanol resulting in a wall temperature change of 3 K for $x_{vq,out} = 0.8$ and 5 K for $x_{vq,out} = 0.4$.

The second aspect is that decreasing the outlet vapour quality does not lead to a better heat transfer coefficient, on the contrary, it reduces it. Figure 5.35 shows that $h_{TP}$ decreases. This is expected as the flow regime is already convective boiling and an increase in mass flux reduces the boiling number leading to lower heat transfer coefficients.

Finally, as $h_{TP}$ is lower than methanol, the effect of the uncertainty on it is higher. Uncertainty on the heat transfer coefficient needs to be reduced as errors in the wall temperature of +6 / -2 K are possible.

In general, R1233ZDE is deemed a valid alternative to methanol for two-phase cooling of fuel cells if flammability is a limiting constraint.

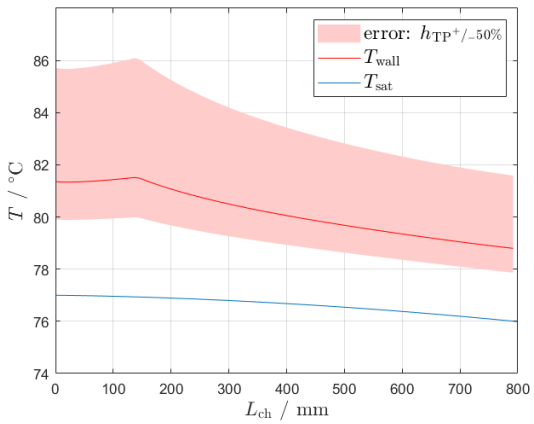


Figure 5.33: Wall and coolant temperature evolution of R1233ZDE in 0.75x0.75 mm channel with $x_{vq,out} = 0.8$.

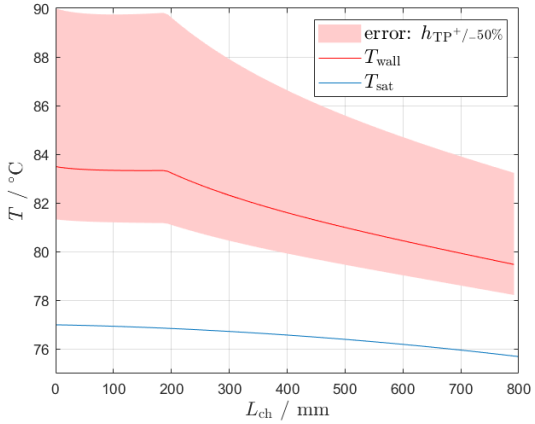


Figure 5.34: Wall and coolant temperature evolution of R1233ZDE in 0.75x0.75 mm channel with $x_{vq,out} = 0.4$.

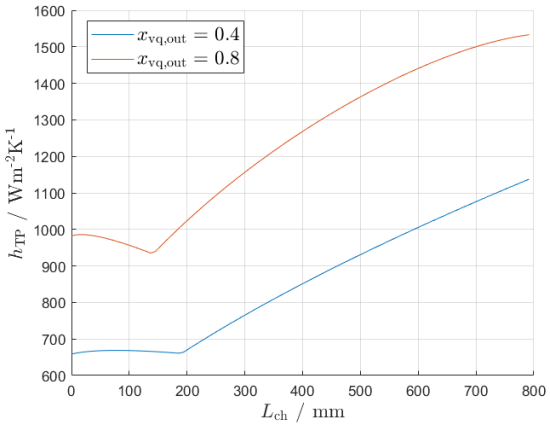


Figure 5.35: Two-phase heat transfer coefficient of R1233ZDE at $x_{vq,out} = 0.4$ and $x_{vq,out} = 0.8$.

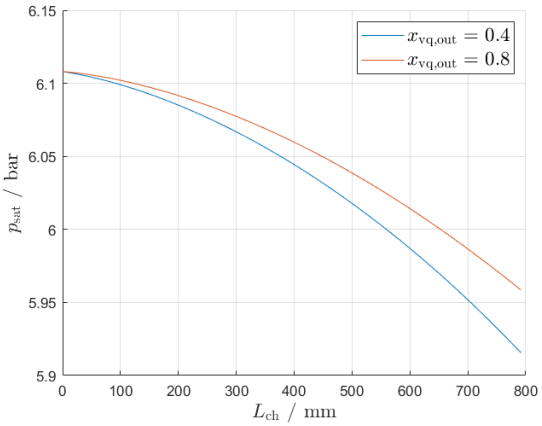


Figure 5.36: Presure drop of R1233ZDE at $x_{vq,out} = 0.4$ and $x_{vq,out} = 0.8$.

## 5.2. 0D THERMAL MANAGEMENT SYSTEM ANALYSIS

The proposed PMP and VCS systems together with the reference case of single-phase EGW cooling are analyzed and compared. All the permutations of the design space spanned by $H_{\text{duct}}$, $W_{\text{duct}}$, $\theta_{\text{HX}}$, and $\epsilon_{\text{HX}}$ are simulated and their performance parameters plotted to form a Pareto front. The solutions on this front are defined based on the maximum total available power and minimum system mass. The system mass is always used as an independent performance parameter even though its contribution to overall power demand is already included in the drag increase due to increased lift. This is done because mass not only has an effect on lift but it also has structural implications that are not considered in this work. In this results section, the VCS systems are differentiated in their name by specifying the design condenser temperature as "T90" for a temperature of 90 °C.

### 5.2.1. OVERALL PERFORMANCE COMPARISON

The overall cooling power penalty is a measure of how much of the available fuel cell power is lost to the cooling system. It is inversely proportional to the total power and highlights which system design has power advantages and which one power penalties. A positive value of $P_{\text{penalty}}$ indicates a power loss, and, by convention, a negative penalty indicates a power gain. It is shown in Figure 5.37 for the whole design space while only the non-dominated solutions are displayed in Figure 5.38. Two key aspects are immediately clear. The first one is that methanol systems are the lightest, irrespective of system configuration, with systems using R1233ZDE falling between methanol and EGW. The second aspect is that VCS systems always have a higher power penalty with respect to pumped multi and single-phase systems. The power deficiency of VCS systems is further highlighted in Figure 5.39.

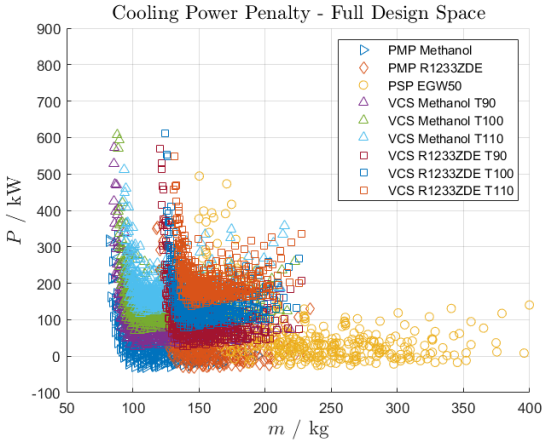


Figure 5.37: Cooling power penalty for all systems spanning the entire design space.

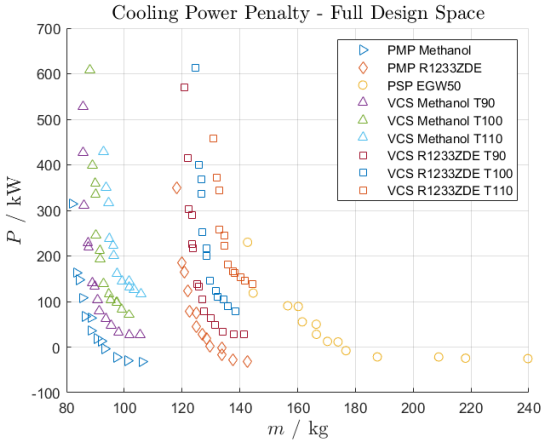


Figure 5.38: Cooling power penalty of non-dominated systems.

To better understand how the weight advantage of methanol arises, Figure 5.41 shows that the differentiating factor is the coolant mass carried in the system, while the mass of the components falls in the same range for all systems considered. The constant nature of coolant weight for the phase-change systems is due to the requirement of a fully flooded fuel cell at startup which represents a constant volume of fluid for all systems and is independent of system volume. The coolant mass for water changes according to the system volume.

Additionally, the drag expressed in terms of drag power, (negative = thrust), shows no significant difference between the VCS and PMP systems (Figure 5.40). This shows that most of the power penalty of VCS systems comes from the compressor and no significant drag reduction due to more compact heat exchangers or higher heat transfer temperatures is present.

Finally, the ram air duct efficiency is shown in Figure 5.42 compared to the drag power. The efficiency is positive in some cases, indicating that some ram air duct designs are able to generate thrust from the core flow which results in overall positive thrust (quadrant II). Some of the designs that have a positive efficiency produce more drag than thrust (quadrant I) indicating that aerodynamic effects external to the core flow

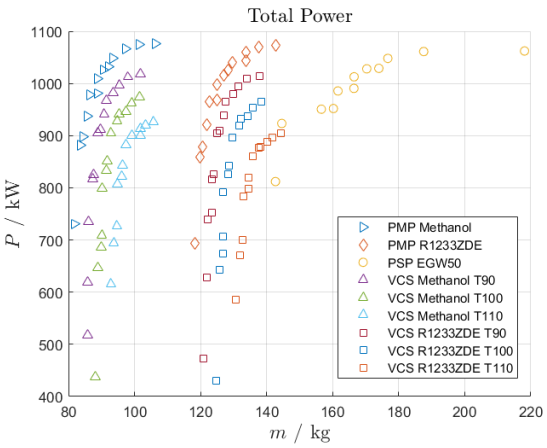


Figure 5.39: Total available propulsion system power. Non-dominated solutions.

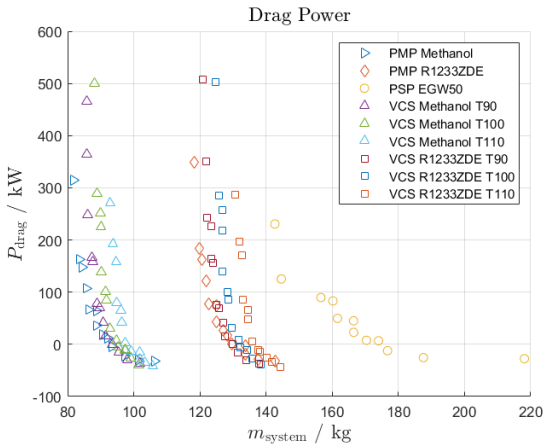


Figure 5.40: Drag induced power loss of non-dominated systems.

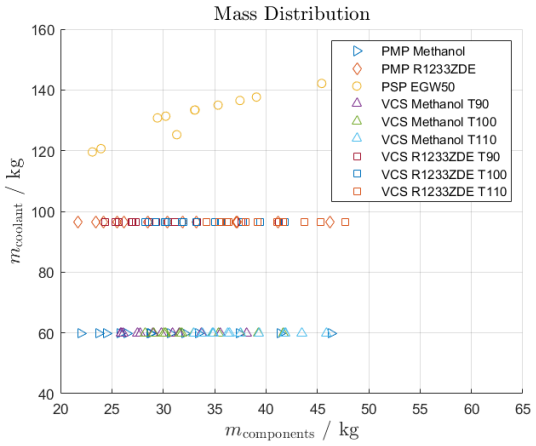


Figure 5.41: Coolant and components mass for non-dominated solutions.

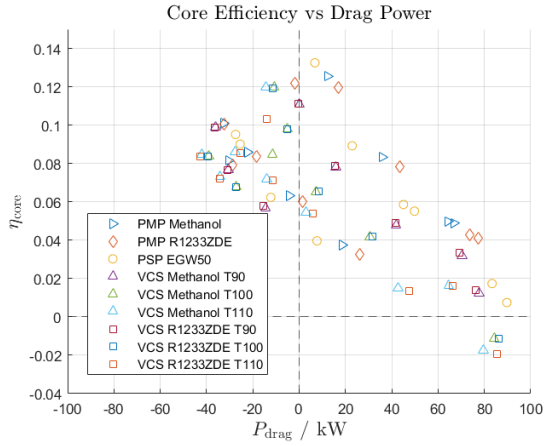


Figure 5.42: Core efficiency and drag power for non-dominated solutions.

offset the core thrust and should be investigated. Designs falling in quadrant IV have negative efficiencies meaning more drag is generated by the core flow than thrust. This happens when the pressure drop in the main heat exchanger offsets the effect of the added thermal energy to the core flow.

### 5.2.2. RAM AIR DUCT DESIGN SPACE

The ram air duct design space can be better visualized when plotting relevant performance parameters of the best-performing systems against $H_{\text{duct}}$ and $W_{\text{duct}}$. In this case, for each combination of $H_{\text{duct}}$ and $W_{\text{duct}}$, always the system with the highest total power is shown. The trends of total power are similar for all systems. A clear maximum is not present in the explored design space. For any duct width, the maximum total power is always reached at a duct height of 0.75 m. For the VCS systems, this maximum shifts to 1 m duct height at $W_{\text{duct}}$ = 1.5 m. As expected from the Pareto front analysis, the VCS systems have lower total power the higher the condenser temperature is.

#### EXTERNAL AND INTERNAL FORCES

Although the total available power of VCS systems is low, due to the power absorbed by the compressor, the net thrust they produce from the ram air duct core flow, is higher than for conventional or PMP systems. The net force of the system is shown in Figure A.1. As the trends are similar between all the systems, to simplify the investigation of the relationship between the duct geometry and the net thrust, the VCS with methanol and a condenser temperature of 100 °C is used as example.

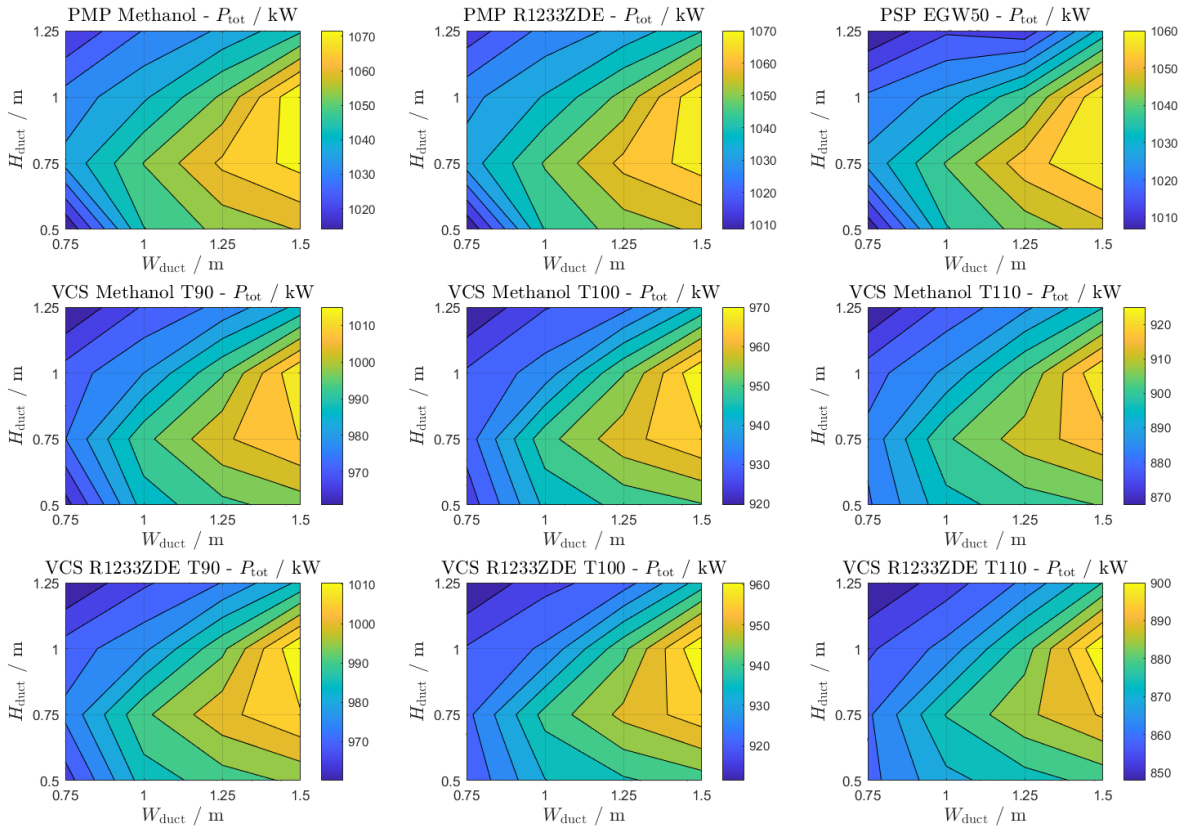


Figure 5.43: Maximum total power of all systems with different duct designs.

The net force of the ram air duct is a balance between internal and external forces. The most prominent external forces are the drag forces developed by the scoop inlet, represented by $C_{Df,full}$, and the spilled air around the inlet, represented by $C_{Dsp}$. Their combined effect is plotted in Figure 5.44. For square scoop inlets, this force is proportional to the inlet aspect ratio, as a slender inlet allows non-ingested air to divert more easily around it at both partial and full mass flow. Additionally, spillage drag is inversely proportional to the mass flow ratio $\dot{m}/\dot{m}_0$ of the inlet, shown in Figure 5.45. The inlet area is determined by the diffuser area ratio. At low duct heights, the diffuser is able to match the required free stream area well, resulting in high mass flow ratios. For high duct heights, the diffuser area ratio is limited by the diffuser half angle and the inlet area remains larger than the ingested stream tube area in free stream conditions resulting in low mass flow ratios.

The internal force that balances the external drag is the thrust produced by the core flow through the ram air duct. The highest core flow thrust is achieved at the highest core efficiency, shown in Figure 5.46. The highest efficiency is reached when thermal energy is added to the core flow at the highest pressure. Additionally, a high core efficiency is achieved when the pressure drop over the main heat exchanger is low. Both these conditions are reached for duct designs that maximize cross-sectional area. A large cross-sectional area means a high area ratio between the stream tube area in the free stream and the heat exchanger frontal area. In incompressible flow, the area ratio is directly related to the pressure ratio and thus higher pressures in front of the main heat exchanger are reached at larger cross-sectional areas.

The ducts with the highest core efficiency coincide with the ducts with higher drag, thus the optimum is found at a balance between the two. This balance is found when most of the area ratio is taken up by the diffuser without relying on external pre-compression. The diffusers with the highest area ratio are found at the duct height at which their angle becomes limiting. At larger duct heights, the limited diffuser angle reduces the area ratio while at lower heights, a lower area ratio is needed to match the stream tube area. This

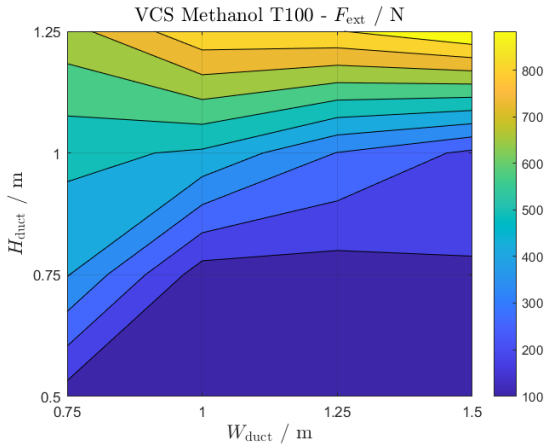


Figure 5.44: External forces on scoop inlet for different duct geometries.

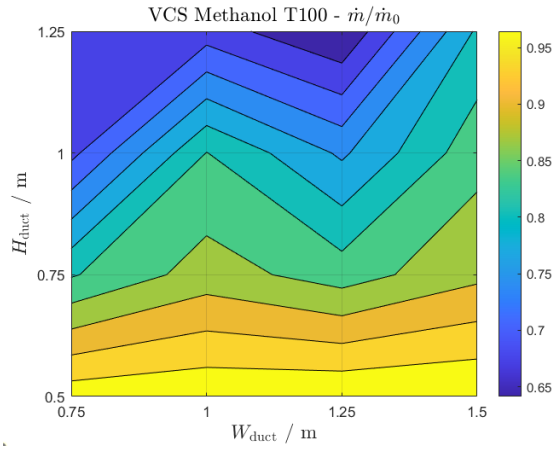


Figure 5.45: Mass flow ratio of scoop inlet for different duct geometries.

region is found at $H_{duct}$ 0.75 m as shown in Figure 5.47.

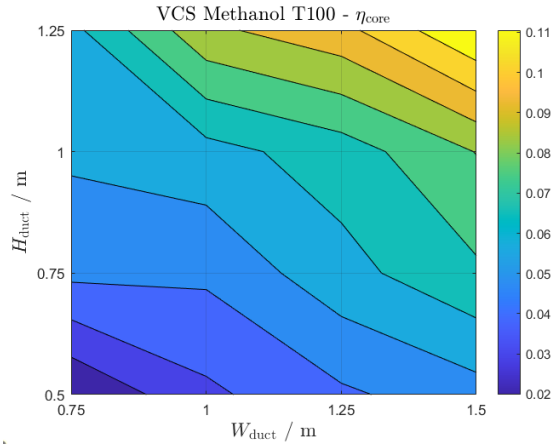


Figure 5.46: Core efficiency for different duct geometries.

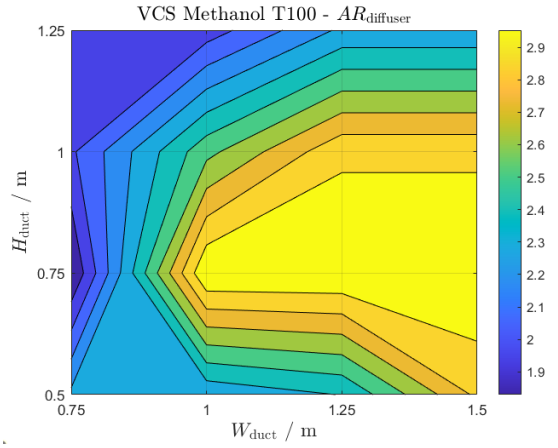


Figure 5.47: Diffuser area ratio for different duct geometries.

Additional figures of $F_{external}$, $\dot{m}/\dot{m}_0$, $\eta_{core}$ and $AR_{diffuser}$, for all the systems can be found in Appendix A.

### PRESSURE DROP EFFECTS ON SUBCOOLING

The cooling channel analysis in section 5.1 shows that the allowable subcooling degree for the onset of nucleate boiling differs between methanol and R1233ZDE. In PMP systems the frictional pressure drop lowers the saturation temperature in the condenser, and consequently the temperature at the pump outlet. This results in a subcooled liquid entering the fuel cell as shown in Figure 5.48. The subcooling is inversely proportional to the pressure drop in the main heat exchanger as shown in Figure 5.49. For the PMP system with methanol, the degree of subcooling is lower than the one required for ONB. This might result in hot spots at the fuel cell inlet and needs to be avoided. A possible solution is to use the coolant to cool other parts of the propulsion system, like the high-power electronics, before entering the fuel cell. This would allow using convective heat transfer to bring the coolant closer to saturation conditions.

For the PMP system with R1233ZDE the subcooling is present as well but it lies within the limits of ONB and does not present a problem.

Also for the methanol VCS system at $T_{cond}$ = 90 °C, subcooling is present. This is partly due to the pressure drop in the condenser and partly due to the further subcooling of the coolant in the internal heat exchanger. As this subcooling is determined by the necessary superheating at the compressor inlet, a connection exists between compressor safety margins and subcooling at the fuel cell inlet. In the current configuration, the subcooling is within ONB limits and does not pose a problem.

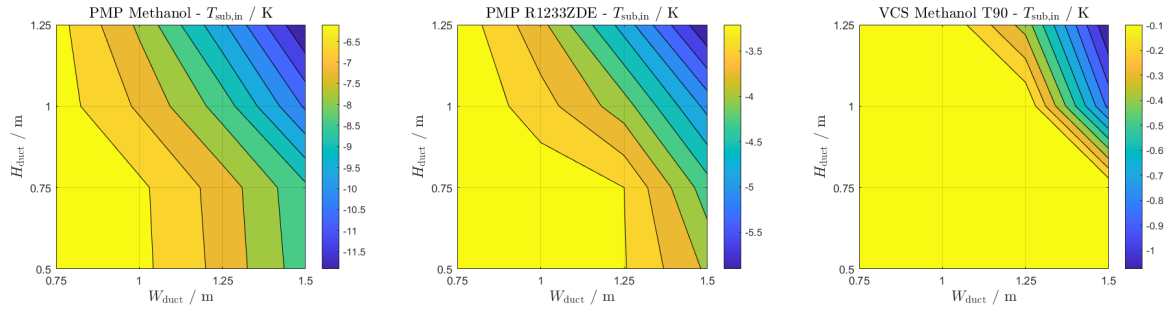


Figure 5.48: Degree of subcooling at fuel cell inlet.

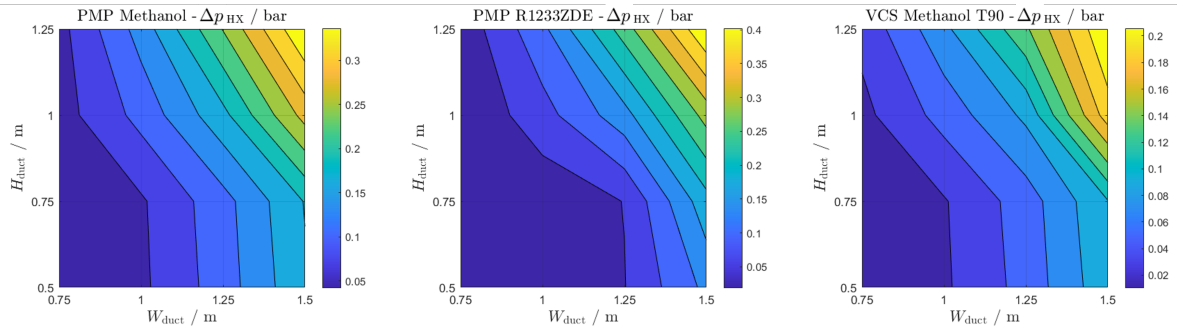


Figure 5.49: Coolant pressure drop in the main heat exchanger.

### 5.2.3. MAIN HEAT EXCHANGER DESIGN SPACE

The variables spanning the main heat exchanger design space are the tilt angle $\theta_{HX}$ at which the heat exchanger resides in the ram air duct and the design effectiveness $\epsilon_{HX}$. The relevant heat exchanger parameters are shown for the duct geometry of $H_{duct}$ = 1 m and $W_{duct}$ = 1.5 m for the systems with highest total power. The blank area in the plots represents part of the design space that is geometrically infeasible as the low tilt angle would result in the heat exchanger taking up more length than the one available.

The total power is visualized for all systems in Figure 5.50. The optimum is between 25 and 30 degrees tilt for all systems. This is on the edge of the heat exchanger core stall margin as found in Refs. [99, 111]. As the pressure drop due to angled inflow is not modelled in this work, further research should be done to capture the effects of angled inflow as it is relevant for ram air cooling of fuel cells and possibly other systems. In terms of effectiveness, the optimal range is between 0.4 and 0.5 for PMP and conventional systems but shifts to lower values for VCS systems. The shift is proportional to the condenser temperature.

This trend can be explained by looking at the methanol VCS systems as an example. Again, the optimal heat exchanger configuration is a balance between different forces at play. The parameters that influence the balance are the duct mass flow ratio, the diffuser area ratio, and the heat exchanger pressure drop.

The optimal ram air duct has a mass flow ratio, which influences the external aerodynamic forces, as close to one as possible. The mass flow ratio is shown in Figure 5.51 and tends to decrease with higher condenser temperatures. This is expected as at constant effectiveness, a higher condenser temperature results in a lower air mass flow needed to reject the thermal energy. Lower mass flow requirements would result in lower mass flow ratios. Thus, to compensate, the optimal design naturally falls towards lower effectiveness for higher condenser temperatures.

The optimal design does not coincide with the highest mass flow ratio as the pressure drop over the heat exchanger rises with the mass flow ratio as shown in Figure 5.52.

Finally, Figure 5.53 highlights the interaction between the diffuser area ratio and heat exchanger tilt angle. As the tilt angle decreases, more duct length is taken up by the heat exchanger. With a lower length available to slow down the flow, the diffuser area ratio decreases. Additionally, when the effectiveness is sufficiently low, the limited diffuser aspect ratio does not constrain the design anymore as a larger stream tube area is

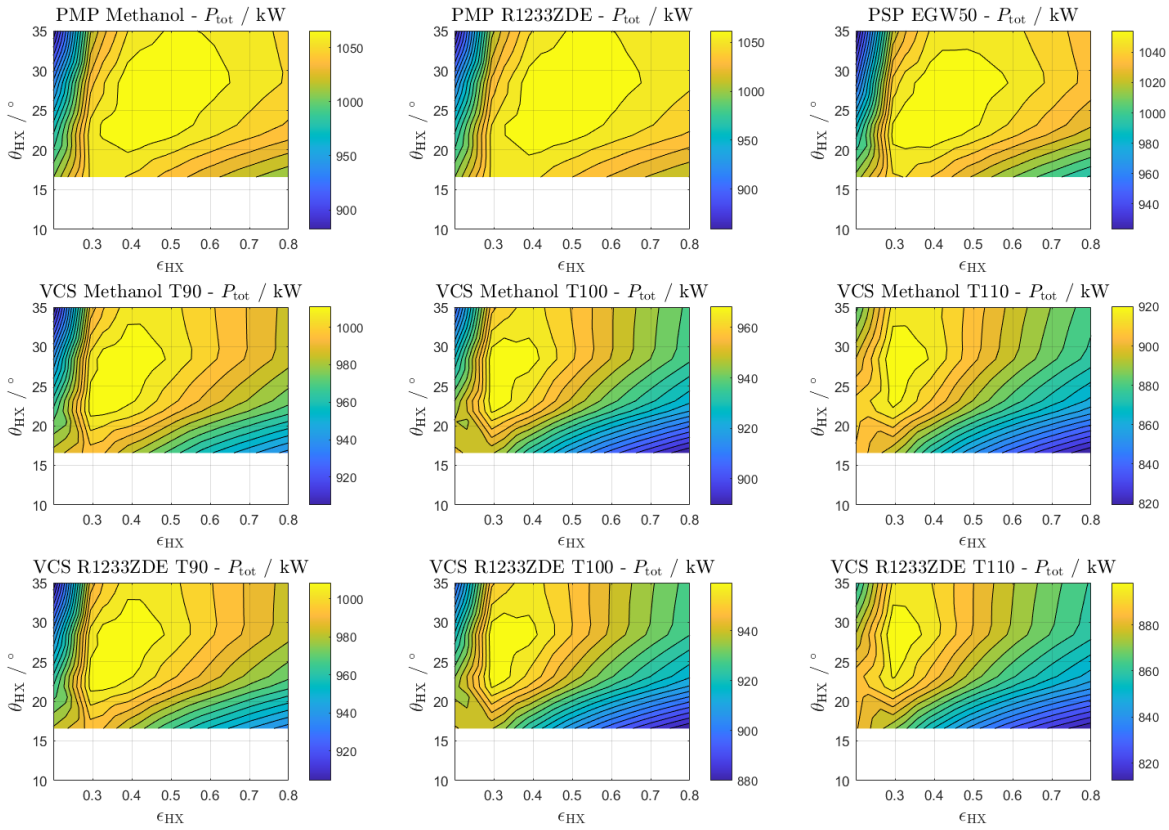


Figure 5.50: Maximum total power of all systems with different heat exchanger designs.

ingested. The optimal design falls again at the border of diffuser-limited geometries.

The thickness of the main heat exchanger, shown in Figure 5.54, depends on several factors. From an air-side perspective, a higher airspeed, related to lower effectiveness, results in higher heat transfer coefficients and as such thinner HX cores. Additionally, as the available installation area increases with decreasing tilt angle, the thickness decreases. The coolant properties are also influencing the heat exchanger design. Fluids that are condensing, like in PMP systems, have higher heat transfer coefficients and result in slightly thinner cores than single-phase EGW systems. Furthermore, if the saturation temperature in the condensing heat exchanger is increased through the use of VCS systems, the heat exchanger thickness is reduced.

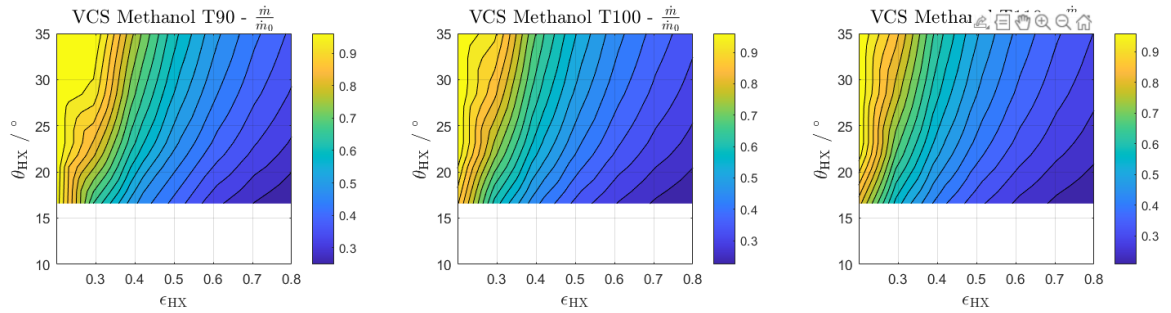


Figure 5.51: Mass flow ratio for different heat exchanger designs.

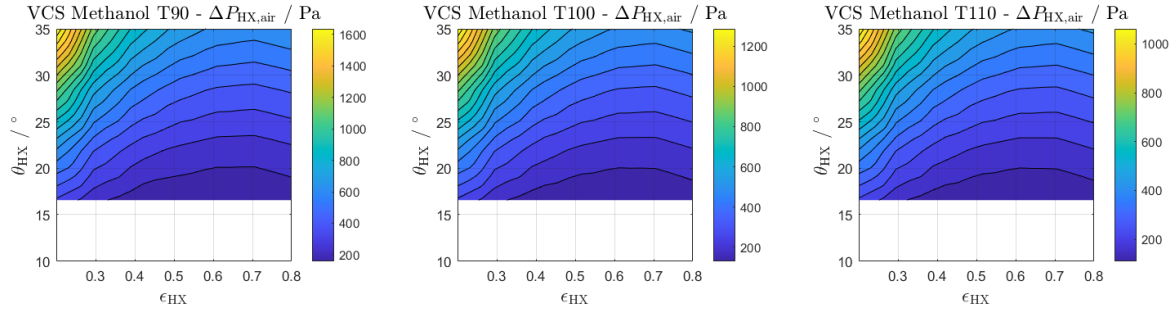


Figure 5.52: Heat exchanger air pressure drop for different heat exchanger designs.

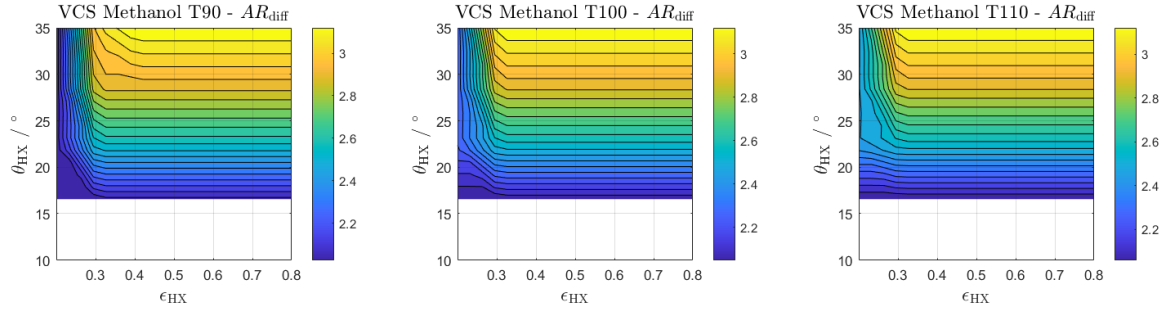


Figure 5.53: Diffuser area ratio for different heat exchanger designs.

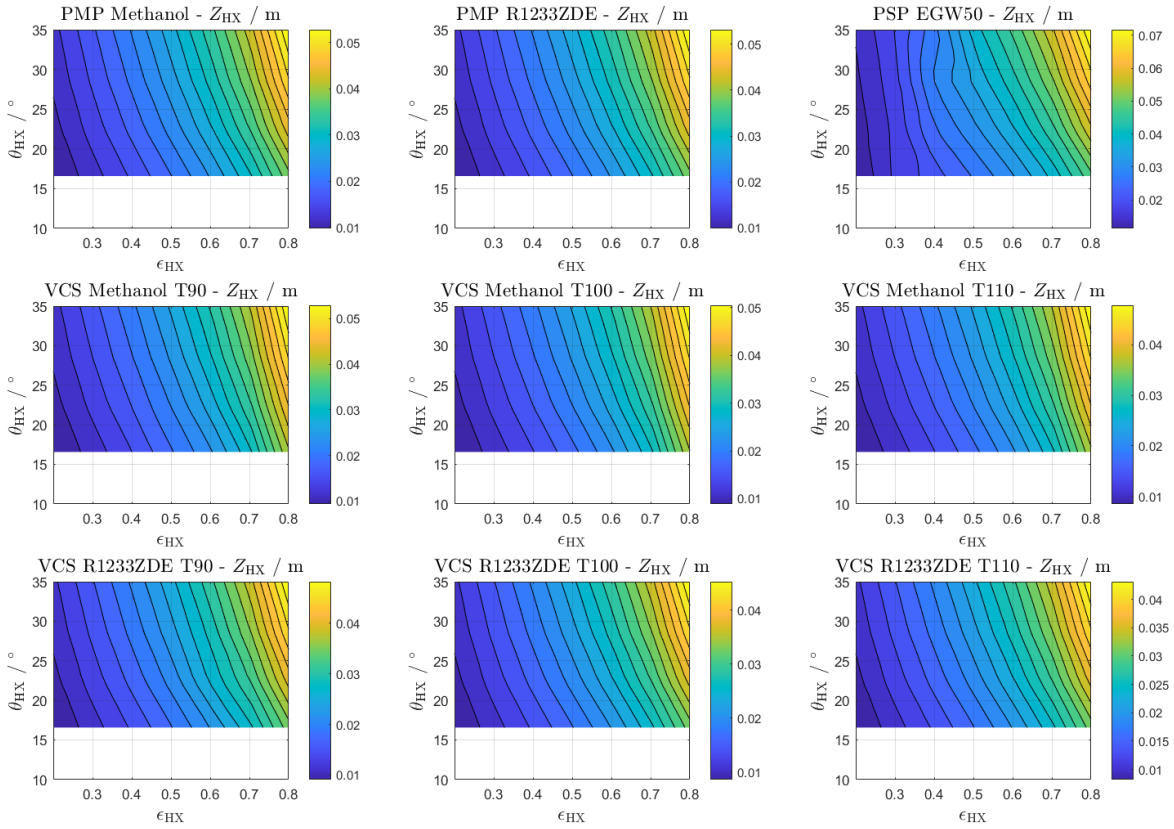


Figure 5.54: Main heat exchanger core thickness.

### 5.2.4. SYSTEM POWER AND MASS BREAKDOWN

A system mass breakdown is given for the systems designed with $H_{\text{duct}}$ = 1m and $W_{\text{duct}}$ = 1.5m in Table 5.2. The respective best-performing heat exchanger tilt angle and effectiveness are stated in the table. The fuel cell power is a constant for all systems, as it comes directly from the design specifications. In the table, the negative contributions to overall power are in parentheses, while the positive contributions are not. To maintain the convention of drag power, thrust power is used in this table instead. The pump power is low for all systems with the single-phase system having the highest power at 3 kW. For the systems in which the pump is only used to recirculate the small portion of liquid coolant that does not evaporate in the fuel cell, the pumping power is negligible. More significant is the compressor power. As expected from preliminary analysis, methanol needs a lower compressor power to reach the pressure level that results in the same saturation temperature of R1233ZDE. The compressor power increase with condenser saturation temperature with each 10 K addition resulting in power consumption increases well above 50 kW for all VCS systems. The large power requirements of the compressor offset the produced thrust of the ram air duct and result in a less powerful system overall.

The contribution of the ram air duct thrust offsets the system power demand for PMP and PSP architectures. For VCS systems, although the thrust is higher, it is not large enough to offset the compressor power, resulting in an overall decrease in total available power. The weight power is intended as the added induced drag power loss due to increase lift generation, needed to support the system weight. Methanol systems have the least added induced drag and thus the lowest power loss attributed to weight. Although the compressor produces significant power, and as such is heavy, the reduced pipe cross-section and heat exchanger weight keep the system weight low. R1233ZDE is in between methanol and EGW50 in terms of weight-induced power losses.

A mass breakdown detailing the contribution of each component is presented in Table 5.3. The first biggest contribution to system mass is the coolant weight. Two-phase systems have the advantage that most of the cooling system volume is filled with vapour instead of liquid, reducing the coolant charge needed to fill the system. The second biggest contributor to system weight is the main heat exchanger. The PSP system has the highest weight, followed by PMP systems. VCS systems have the lowest heat exchanger mass, but the gains in this area are offset buy the higher weight of the compressor. This results in only slight mass advantages w.r.t their pumped counterpart. From this mass breakdown it is apparent that the pump mass is underestimated. This underestimation comes from the fact that the weight of the electric motor and driver are based on reference figures for motors with propulsion applications in mind. This figure does not scale appropriately at low powers and in future work, a better estimation for pump mass should be implemented.

Table 5.2: System power breakdown for systems designed at $H_{duct}$ = 1m and $W_{duct}$ = 1.5m.

| | PMP Methanol | PMP R1233ZDE | PSP EGW50 |
|---|---|---|---|
| $\epsilon_{HX}$ | 0.4 | 0.4 | 0.4 |
| $\theta_{HX}$ / ° | 22.5 | 22.5 | 22.5 |
| $P_{FC}$ / W | 1,050,000 | 1,050,000 | 1,050,000 |
| $P_{pump}$ / W | (156) | (731) | (3,013) |
| $P_{comp}$ / W | - | - | - |
| $P_{net}$ / W | 1,049,844 | 1,049,269 | 1,046,987 |
| $P_{thrust}$ / W | 32,554 | 32,241 | 27,458 |
| $P_{weight}$ / W | (5,946) | (7,990) | (12,210) |
| $P_{tot}$ / W | 1,076,452 | 1,073,520 | 1,062,236 |

| | VCS Methanol T90 | VCS Methanol T100 | VCS Methanol T110 |
|---|---|---|---|
| $\epsilon_{HX}$ | 0.3 | 0.3 | 0.3 |
| $\theta_{HX}$ / ° | 22.5 | 28.7 | 28.7 |
| $P_{FC}$ / W | 1,050,000 | 1,050,000 | 1,050,000 |
| $P_{pump}$ / W | (21) | (23) | (25) |
| $P_{comp}$ / W | (62,977) | (109,671) | (159,311) |
| $P_{net}$ / W | 987,001 | 940,306 | 890,665 |
| $P_{thrust}$ / W | 36,190 | 38,978 | 42,164 |
| $P_{weight}$ / W | (5,696) | (5,687) | (5,920) |
| $P_{tot}$ / W | 1,017,495 | 973,596 | 926,909 |

| | VCS R1233ZDE T90 | VCS R1233ZDE T100 | VCS R1233ZDE T110 |
|---|---|---|---|
| $\epsilon_{HX}$ | 0.3 | 0.3 | 0.3 |
| $\theta_{HX}$ / ° | 22.5 | 28.7 | 28.7 |
| $P_{FC}$ / W | 1,050,000 | 1,050,000 | 1,050,000 |
| $P_{pump}$ / W | (44) | (58) | (82) |
| $P_{comp}$ / W | (64,148) | (116,957) | (180,348) |
| $P_{net}$ / W | 985,808 | 932,985 | 869,570 |
| $P_{thrust}$ / W | 36,479 | 39,365 | 42,805 |
| $P_{weight}$ / W | (7,713) | (7,747) | (8,076) |
| $P_{tot}$ / W | 1,014,575 | 964,603 | 904,299 |

Table 5.3: System mass breakdown for systems designed at $H_{duct}$ = 1m and $W_{duct}$ = 1.5m.

| | PMP Methanol | PMP R1233ZDE | PSP EGW50 |
|---|---|---|---|
| $m_{cool}$ / kg | 59.9 | 96.5 | 154.8 |
| $m_{pump}$ / kg | 0.0173 | 0.0812 | 0.3347 |
| $m_{comp}$ / kg | 0.0 | 0.0 | 0.0 |
| $m_{HX}$ / kg | 42.6 | 42.9 | 58.7 |
| $m_{pipes}$ / kg | 3.8 | 3.2 | 4.3 |
| $m_{tot}$ / kg | 106.2 | 142.7 | 218.1 |

| | VCS Methanol T90 | VCS Methanol T100 | VCS Methanol T110 |
|---|---|---|---|
| $m_{cool}$ / kg | 59.9 | 59.9 | 59.9 |
| $m_{pump}$ / kg | 0.0024 | 0.0025 | 0.0027 |
| $m_{comp}$ / kg | 7.0 | 12.2 | 17.7 |
| $m_{HX}$ / kg | 32.1 | 27.0 | 25.8 |
| $m_{pipes}$ / kg | 2.8 | 2.5 | 2.3 |
| $m_{tot}$ / kg | 101.8 | 101.6 | 105.7 |

| | VCS R1233ZDE T90 | VCS R1233ZDE T100 | VCS R1233ZDE T110 |
|---|---|---|---|
| $m_{cool}$ / kg | 96.5 | 96.5 | 96.5 |
| $m_{pump}$ / kg | 0.0049 | 0.0065 | 0.0091 |
| $m_{comp}$ / kg | 7.1 | 13.0 | 20.0 |
| $m_{HX}$ / kg | 31.1 | 26.0 | 24.8 |
| $m_{pipes}$ / kg | 3.0 | 2.9 | 2.9 |
| $m_{tot}$ / kg | 137.8 | 138.4 | 144.3 |

# 6

# CONCLUSIONS AND RECOMMENDATIONS

## 6.1. CONCLUSIONS

In this thesis, preliminary design methods for single and multi-phase thermal management systems for fuel cell in aircraft applications are presented. The models of the relevant components are described and verified while their accuracy is validated against experimental and numerical research. The methods are applied to a preliminary design case study involving three different cooling system configurations for a megawatt-class propulsion system. As such, a model for the preliminary design of the thermal management system of a fuel cell-powered aeroengine has been obtained and qualitatively evaluated and validated. The model gives insights into critical design parameters and physical phenomena spanning all system levels.

Through the method of coolant selection, two valid coolant alternatives to ethyl-glycol water to be used in flow boiling have been selected: Methanol and R1233ZDE. The figures of merit on pump power and heat transfer coefficient correctly identify the differences between the two coolants. Furthermore, the simple system analysis correctly identifies coolants with high and low compressor powers for VCS systems. Coolants with low saturation pressures at operational temperatures induce sub-atmospheric pressures when the system is off and in thermal equilibrium with ambient air which can pose a threat of contamination of the coolant with ambient air through leaks in the system. Finally, constraints on flammability are relaxed for research purposes allowing a promising coolant like Methanol to be investigated further.

For coolants of which the boiling heat transfer coefficient is higher than the reference ethyl-glycol water case, like Methanol, the uncertainty in predicting the correct heat transfer coefficient does not pose a limitation on system design. Conversely, for coolants that have a low boiling heat transfer coefficient, like R1233ZDE, the uncertainty in wall temperature can be as high as 10 K and poses a limitation to system design. If the encountered flow boiling regime is nucleate boiling, an increase in mass flux through the cooling channels can improve the heat transfer coefficient. On the contrary, in convective boiling, the outlet vapour quality should be maximised, thus decreasing the coolant mass flux, to increase the heat transfer coefficient. The vapour quality at dry-out incipience limits the vapour quality at the outlet as a reduction in heat transfer coefficient with subsequent high wall temperatures can be expected after dry-out.

In general, the heat transfer coefficient of low Reynolds number flows encountered in fuel cell cooling channels, is still dominated by the laminar liquid-only convection characteristics of the fluid, thus a high thermal conductivity is a major driver of heat transfer coefficient. The enhancement of heat transfer coefficient due to boiling is generally low as the low wall heat fluxes, result in low boiling numbers. The ratio of liquid to vapour density of the coolant is another driving factor. A large difference between the two densities increases the heat transfer coefficient but also induces higher pressure losses.

From a system architecture perspective, the use of vapour compression systems does not show advantages in decreasing system weight or total available power with respect to pumped multi-phase or single-phase systems. The main reason for this, is that the large compressor power outweighs the reduction in heat exchanger pressure drop. Of the configurations analyzed, the ones utilizing flow boiling resulted in the lowest system weight. The main factor is the lower coolant charge needed as most of the internal volume of the

system is filled with a vapour and not a dense liquid. Pumped multi-phase systems that have high pressure drops, relative to the operational saturation pressure, are subject to high degrees of subcooling at the fuel cell inlet. The degree of subcooling can be well below the allowed subcooling for the onset of nucleate boiling. Fluids with a high surface tension have a low allowed subcooling for onset of nucleate boiling and are most at risk of having a portion of the cooling channel in which boiling does not take place.

The optimal ram air duct design is driven by a balance of internal and external forces. On one hand, a large duct cross-section leads to high core efficiencies due to the increased pressure ratio and decreased heat exchanger pressure drop. On the other hand, a small duct cross-section decreases spillage and inlet drag. The limited diffuser area ratio is identified as being a driving design aspect. Air can diffuse both before entering the inlet, causing spillage, or inside the duct. The optimal diffuser design coincides with the duct geometry that allows for most of the diffusion to happen in the diffuser and not before the inlet.

From a heat exchanger design perspective, the tilt angle influences the available diffuser length, and thus its area ratio, and the heat exchanger core pressure drop. The optimum tilt angle lies where these two aspects balance each other resulting in a high core efficiency. Additionally, the optimal effectiveness is depending on the coolant inlet temperature. High operating temperatures found in VCS systems result in lower effectiveness. This allows to keep the mass flow through the system high, increasing the mass flow ratio of the inlet and reducing external drag forces.

## 6.2. RECOMMENDATIONS

Although the methods and models presented are able to give many insights into preliminary thermal management design, limitations must be addressed. Additionally, areas that need further research to support detailed design are also identified.

When using flow boiling as means of heat transfer, experiments should be used to decrease the uncertainty of heat transfer coefficient prediction. Fluid-surface interactions, which affect both heat transfer and dry-out, need to be evaluated. Additionally, the potential flow instability that arises from the pressure fluctuations generated by the boiling process and the interactions over parallel cooling channels needs to be investigated.

The temperature gradient of the air at the cathode has been identified as a relevant parameter to consider when designing thermal management. The trade-off between temperature uniformity over the whole membrane and water management needs to be researched in more detail to understand to what degree temperature gradients in the fuel cell cooling channels are needed. If temperature gradients are found to be a driving requirement of fuel cell cooling system performance, the use of multi-component coolant mixtures should be investigated. Zeotropic mixtures that are composed of fluids with different boiling points naturally undergo a temperature change during the boiling process at constant pressure. This phenomenon would eliminate the need of inducing additional pressure drops on the boiling fluid to change saturation pressure and would result in power saving at the system level.

At the system level, a more detailed weight analysis should be performed to verify that PMP systems have a substantial weight advantage in comparison to conventional PSP systems. A model for low-power pumps is needed and additional subsystems like secondary thermal management of components should be included. At the moment, a single pipe is assumed to run from the fuel cell assembly to the main heat exchanger but in reality, it is expected that multiple parallel lines could be used or that joints and splitters be implemented to distribute the coolant to the fuel cell stacks. This additional complexity should be modelled once a preliminary 3D model of the component placement in the nacelle is available. In this respect, for all configurations, snowball effects should be taken into account to adapt the fuel cell size to the power requirement of the thermal management system. For this purpose, a detailed fuel cell sizing system should be developed.

VCS systems are limited by the compressor power requirement and the estimation of compressor efficiency is key to ensure that modelling is accurate and power savings are maximized. 1D and 3D modelling of this component are required to move to a more detailed level of system design. Additionally, dynamic simulations are required to verify that the system can operate at start-up and shutdown and handle load changes throughout the mission profile of the reference aircraft.

The aerodynamic analysis is limited at the preliminary design level. Only trends and relevant parameters

are identified but 3D modelling of the main ram air duct should be performed to characterize the internal and external flows. Especially the interaction of the propeller wake with the inlet and duct fairing should be the focus of research efforts as the effects on spillage drag might be significant. Additionally, the induced swirl in the propeller wash should be known when detailing the duct geometry. Finally, an off-design analysis in cruise conditions is needed to rate the drag or thrust generated by the system and determine the impact on fuel burn.

# A

# Additional Results Figures

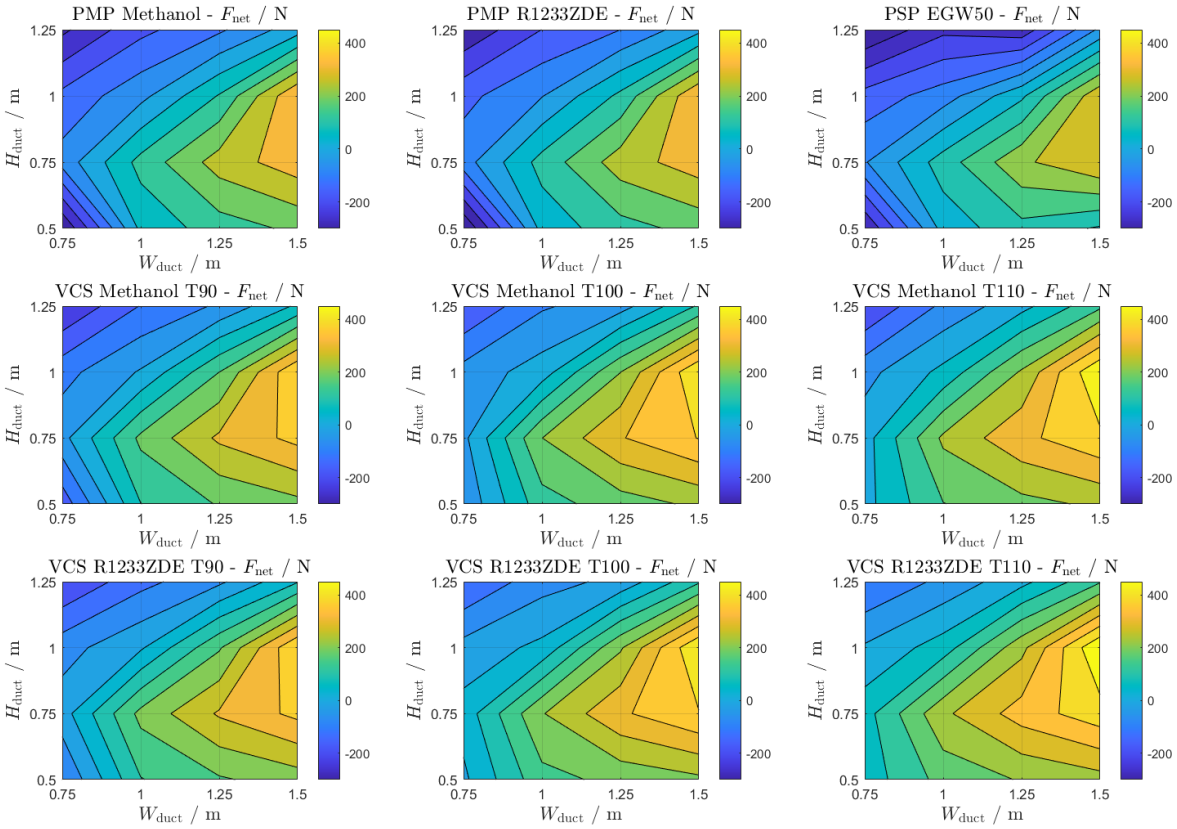


Figure A.1: Net thrust for different duct geometries of all systems.

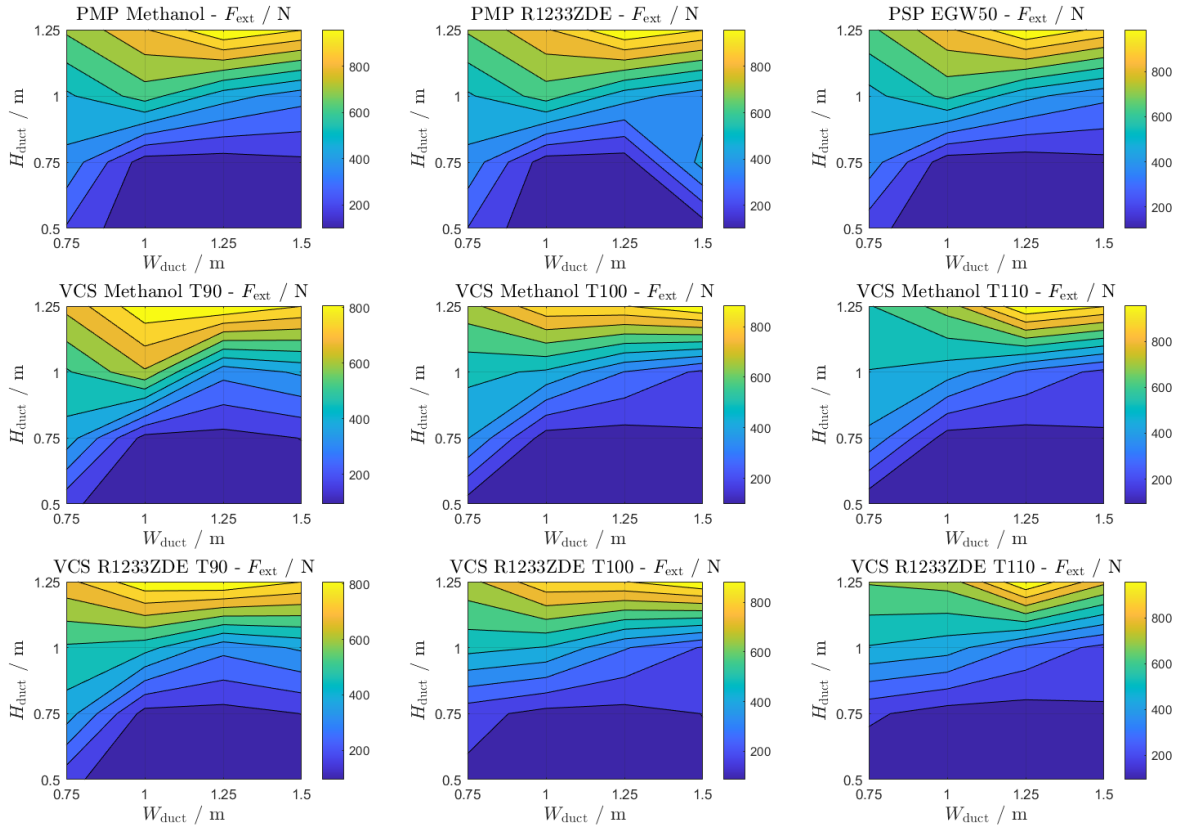


Figure A.2: External forces on scoop inlet for different duct geometries of all systems.

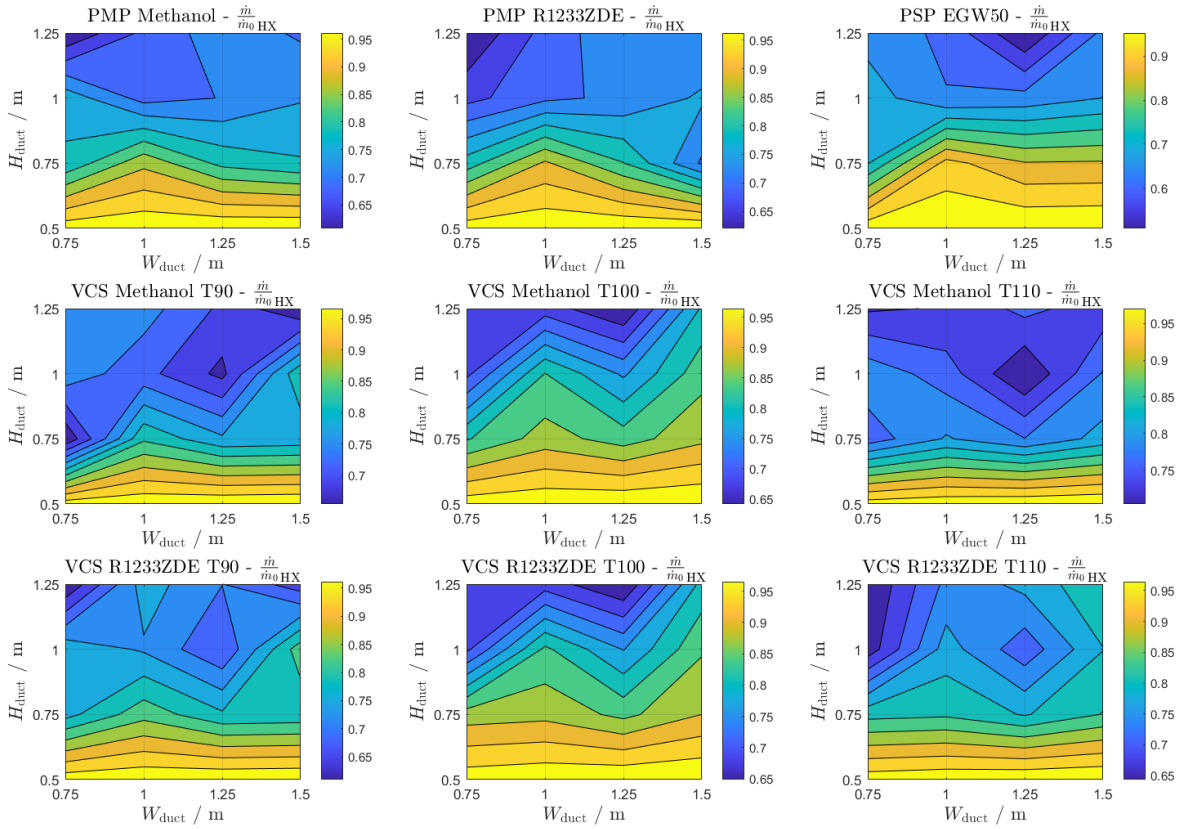


Figure A.3: Inlet mass flow ratio for different duct geometries of all systems.

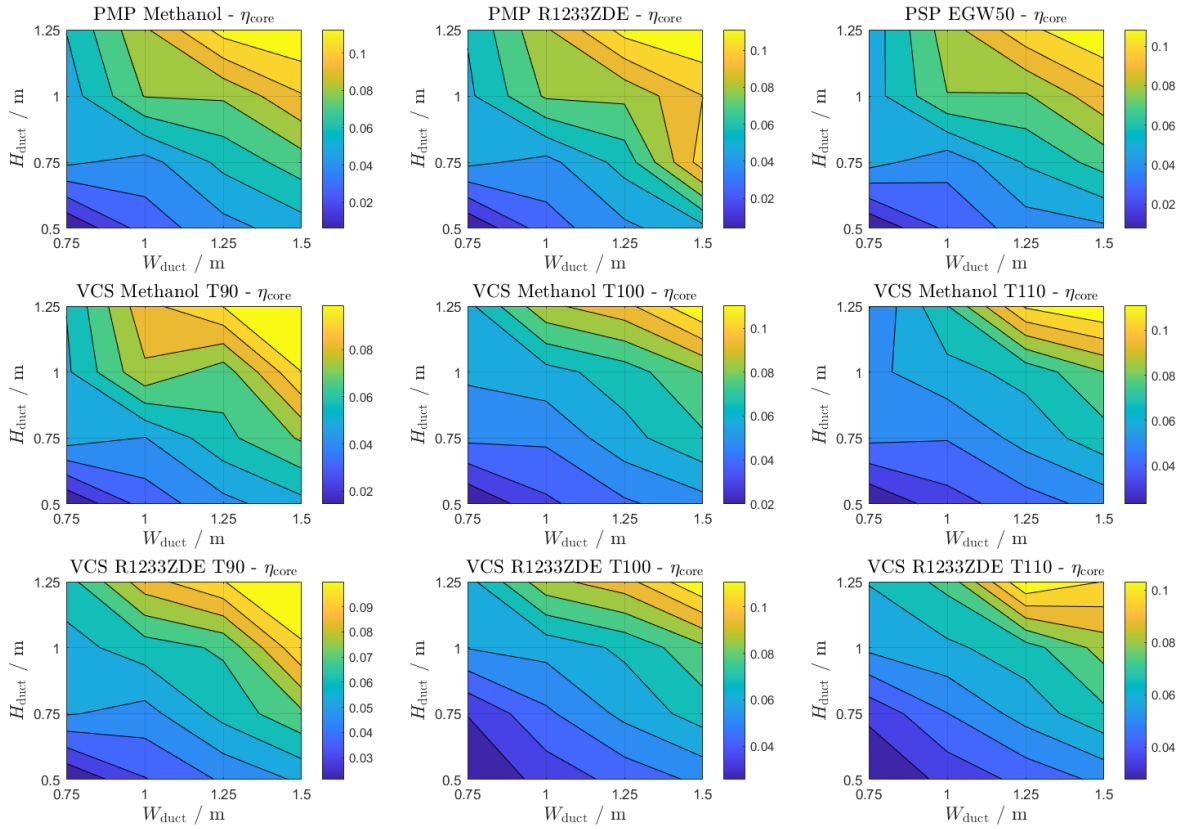


Figure A.4: Core efficiency for different duct geometries of all systems.

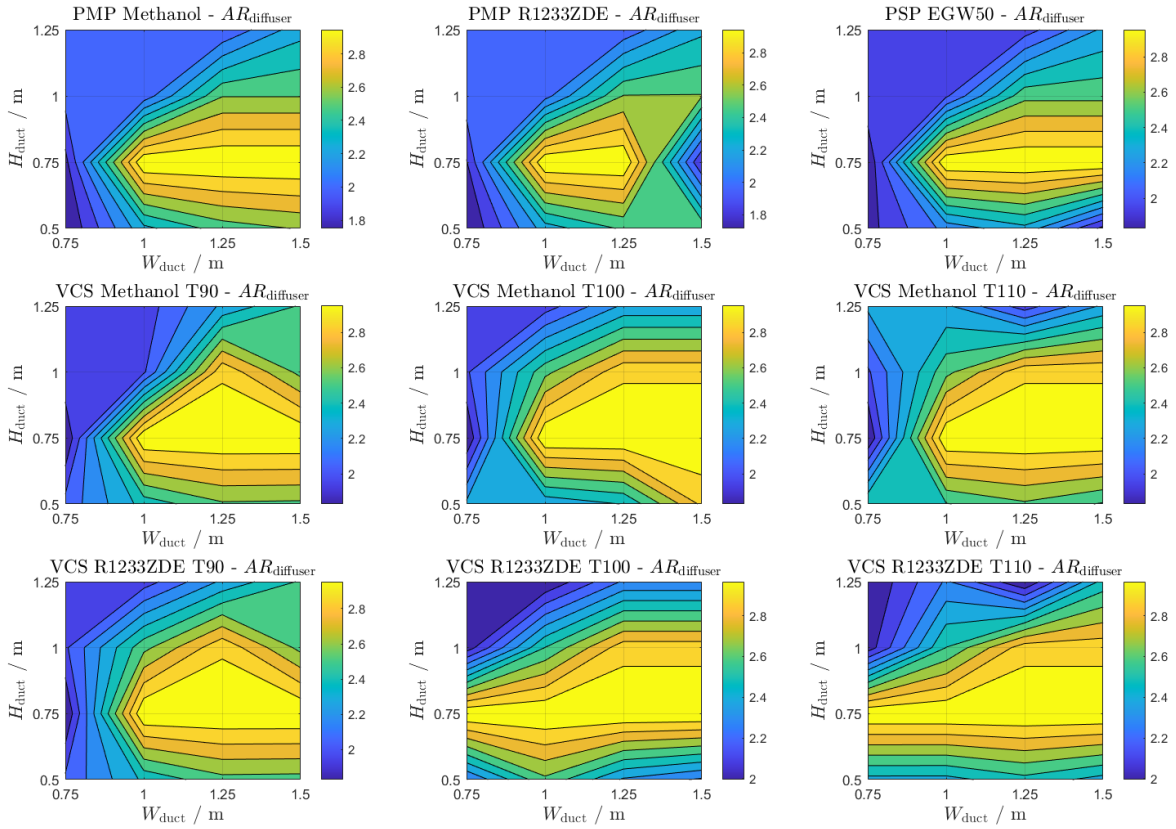


Figure A.5: Diffuser area ratio for different duct geometries of all systems.

# B

# Aircraft Dimensions

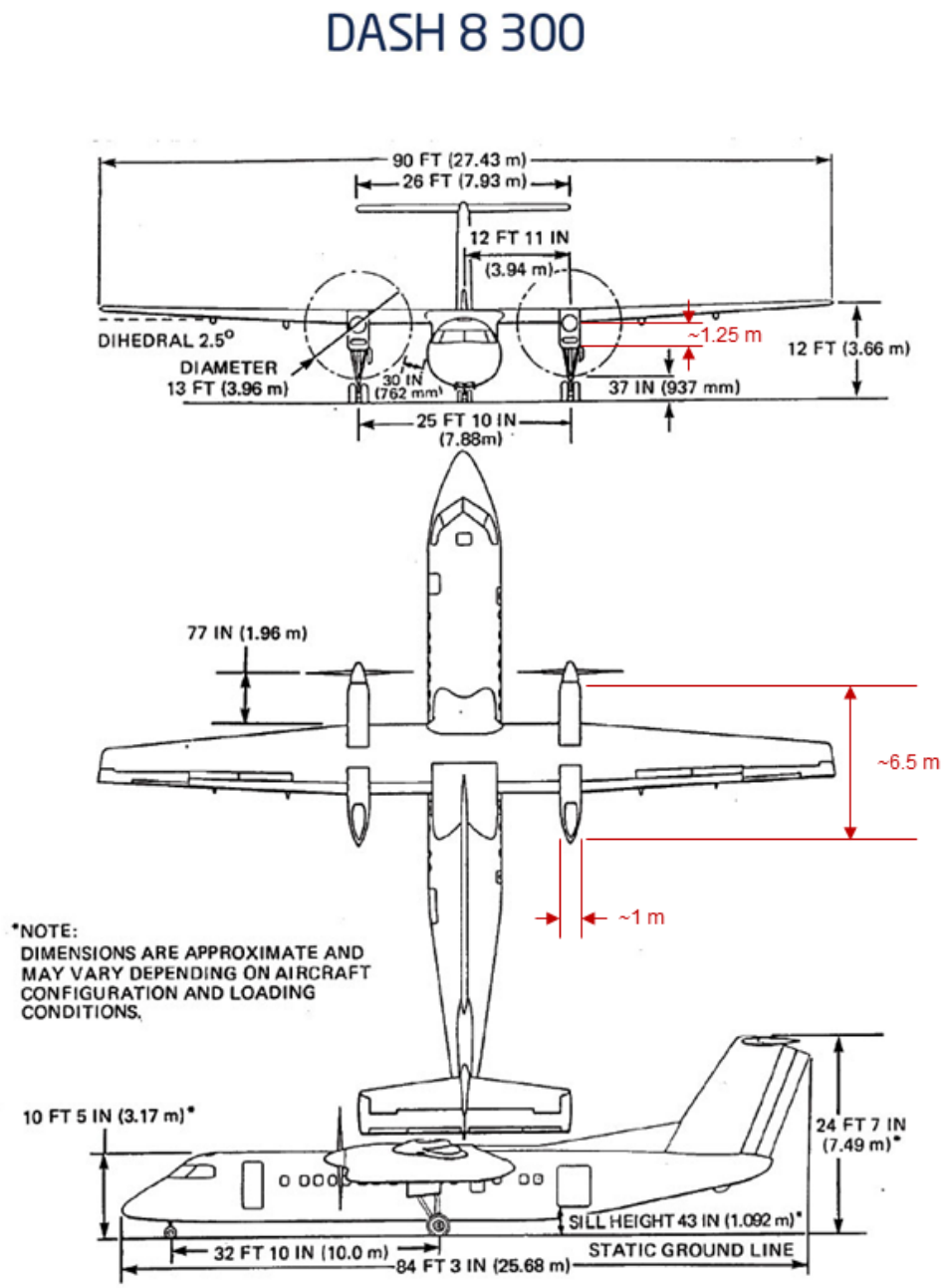


Figure B.1: Dash-8 Q300 dimensions [112]

# BIBLIOGRAPHY


[1] European Commission, *Flightpath 2050 Europe's Vision for Aviation,* (2011), 10.2777/50266.

[2] A. K. Sehra and W. Whitlow, *Propulsion and power for 21st century aviation,* Progress in Aerospace Sciences **40**, 199 (2004).

[3] R. C. Bolam, Y. Vagapov, and A. Anuchin, *Review of Electrically Powered Propulsion for Aircraft,* in *2018 53rd International Universities Power Engineering Conference (UPEC)* (IEEE, 2018) pp. 1–6.

[4] A. Baroutaji, T. Wilberforce, M. Ramadan, and A. G. Olabi, *Comprehensive investigation on hydrogen and fuel cell technology in the aviation and aerospace sectors,* Renewable and Sustainable Energy Reviews **106**, 31 (2019).

[5] F. Yin, A. Gangoli Rao, A. Bhat, and M. Chen, *Performance assessment of a multi-fuel hybrid engine for future aircraft,* Aerospace Science and Technology **77**, 217 (2018).

[6] Airbus, *The ZEROe demonstrator has arrived,* (2022).

[7] A. G. Olabi, T. Wilberforce, and M. A. Abdelkareem, *Fuel cell application in the automotive industry and future perspective,* Energy **214** (2021), 10.1016/J.ENERGY.2020.118955.

[8] I. S. Mehdi, *Application of Solid Oxide Fuel Cells to Aircraft,* ECS Proceedings Volumes **2005-07**, 249 (2005).

[9] V. Venkataraman, *Solid Oxide Fuel Cell Systems and Their Potential Applications in the Aviation Industry and Beyond,* (2022) pp. 171–196.

[10] M. Pundt, M. Kirchner, T. Stremlau, and G. Märker, *Integrating a fuel cell system into a vehicle,* ATZ worldwide 2018 120:2 **120**, 38 (2018).

[11] A. Datta, A. Gessow, and R. Center, *PEM Fuel Cell MODEL for Conceptual Design of Hydrogen eVTOL Aircraft*, Tech. Rep. (2021).

[12] S. Nicolay, S. Karpuk, Y. Liu, and A. Elham, *Conceptual design and optimization of a general aviation aircraft with fuel cells and hydrogen,* International Journal of Hydrogen Energy **46** (2021), 10.1016/j.ijhydene.2021.07.127.

[13] T. Kadyk, C. Winnefeld, R. Hanke-Rauschenbach, and U. Krewer, *Analysis and Design of Fuel Cell Systems for Aviation,* Energies **11** (2018), 10.3390/en11020375.

[14] J. Gao, M. Li, Y. Hu, H. Chen, and Y. Ma, *Challenges and developments of automotive fuel cell hybrid power system and control,* Science China Information Sciences 2019 62:5 **62**, 1 (2019).

[15] D. Kozulovic, *Heat Release of Fuel Cell Powered Aircraft,* in *Proceedings of Global Power and Propulsion Society* (2020).

[16] A. Scott White, E. Waddington, J. M. Merret, P. J. Ansell, E. M. Greitzer, D. K. Hall, S. White, E. Waddington, J. Merret, P. Ansell, E. Greitzer, and D. Hall, *System-level utilization of low-grade, mw-scale thermal loads for electric aircraft,* AIAA AVIATION 2022 Forum (2022), 10.2514/6.2022-3291.

[17] D. N. Ozen, B. Timurkutluk, and K. Altinisik, *Effects of operation temperature and reactant gas humidity levels on performance of PEM fuel cells,* Renewable and Sustainable Energy Reviews **59**, 1298 (2016).

[18] H. Kellermann, M. Lüdemann, M. Pohl, and M. Hornung, *Design and Optimization of Ram Air–Based Thermal Management Systems for Hybrid-Electric Aircraft,* Aerospace **8**, 3 (2020).

[19] J. W. Chapman, S. L. Schnulo, and M. P. Nitzsche, *Development of a Thermal Management System for Electrified Aircraft,* in *AIAA Scitech 2020 Forum* (American Institute of Aeronautics and Astronautics, Reston, Virginia, 2020).

[20] Q. Chen, G. Zhang, X. Zhang, C. Sun, K. Jiao, and Y. Wang, *Thermal management of polymer electrolyte membrane fuel cells: A review of cooling methods, material properties, and durability,* Applied Energy **286**, 116496 (2021).

[21] G. Zhang and S. G. Kandlikar, *A critical review of cooling techniques in proton exchange membrane fuel cell stacks,* International Journal of Hydrogen Energy **37**, 2412 (2012).

[22] F. Barbir, *PEM Fuel Cells* (Elsevier, 2005).

[23] J. Larminie and A. Dicks, *Fuel Cell Systems Explained* (John Wiley & Sons, Ltd., West Sussex, England, 2003).

[24] A. Fly and R. Thring, *A comparison of evaporative and liquid cooling methods for fuel cell vehicles,* International Journal of Hydrogen Energy **41**, 14217 (2016).

[25] M. Reichler, *Theoretische Untersuchungen zur Kühlleistungssteigerung durch innovative Kühlsysteme für Brennstoffzellen- Elektrofahrzeuge*, Ph.D. thesis, Universität Stuttgart, Stuttgart (2009).

[26] E. J. Choi, J. Y. Park, and M. S. Kim, *A comparison of temperature distribution in PEMFC with single-phase water cooling and two-phase HFE-7100 cooling methods by numerical study,* International Journal of Hydrogen Energy **43**, 13406 (2018).

[27] U. Soupremanien, S. Le Person, M. Favre-Marinet, and Y. Bultel, *Tools for designing the cooling system of a proton exchange membrane fuel cell,* Applied Thermal Engineering **40**, 161 (2012).

[28] P. T. Garrity, J. F. Klausner, and R. Mei, *A flow boiling microchannel evaporator plate for fuel cell thermal management,* Heat Transfer Engineering **28**, 877 (2007).

[29] E. J. Choi, J. Y. Park, and M. S. Kim, *Two-phase cooling using HFE-7100 for polymer electrolyte membrane fuel cell application,* Applied Thermal Engineering **148**, 868 (2019).

[30] G. Romeo, F. Borello, G. Correa, and E. Cestino, *ENFICA-FC: Design of transport aircraft powered by fuel cell & flight test of zero emission 2-seater aircraft powered by fuel cells fueled by hydrogen,* International Journal of Hydrogen Energy **38**, 469 (2013).

[31] *Hydrogen fuel cells, explained | Airbus,* .

[32] *DLR and MTU Aero Engines study fuel cell propulsion system for aviation - MTU Aero Engines,* .

[33] *H2Fly powers ahead with flight-test campaign | News | Flight Global,* .

[34] C. Winnefeld, T. Kadyk, B. Bensmann, U. Krewer, and R. Hanke-Rauschenbach, *Modelling and Designing Cryogenic Hydrogen Tanks for Future Aircraft Applications,* Energies **11**, 105 (2018).

[35] Z. Xia, B. Wang, Z. Yang, K. Wu, Q. Du, and K. Jiao, *Effect of operating conditions on performance of proton exchange membrane fuel cell with anode recirculation,* Energy Procedia **158**, 1829 (2019).

[36] Y. Chang, Y. Qin, Y. Yin, J. Zhang, and X. Li, *Humidification strategy for polymer electrolyte membrane fuel cells – A review,* Applied Energy **230**, 643 (2018).

[37] J. B. Lu, G. H. Wei, F. J. Zhu, X. H. Yan, and J. L. Zhang, *Pressure Effect on the PEMFC Performance,* Fuel Cells **19** (2019), 10.1002/fuce.201800135.

[38] F. Michel, H. Fieseler, G. Meyer, and F. Theißen, *On-board equipment for liquid hydrogen vehicles,* International Journal of Hydrogen Energy **23**, 191 (1998).

[39] K. A. Friedrich, J. Kallo, J. Schirmer, and G. Schmitthals, *Fuel Cell Systems for Aircraft Application,* ECS Transactions **25** (2009), 10.1149/1.3210571.

[40] M. Schröder, F. Becker, J. Kallo, and C. Gentner, *Optimal operating conditions of PEM fuel cells in commercial aircraft,* International Journal of Hydrogen Energy **46** (2021), 10.1016/j.ijhydene.2021.07.099.

[41] Y. Wang and C.-Y. Wang, *Ultra large-scale simulation of polymer electrolyte fuel cells,* Journal of Power Sources **153**, 130 (2006).

[42] T. L. Kösters, X. Liu, D. Kožulović, S. Wang, J. Friedrichs, and X. Gao, *Comparison of phase-change-heat-pump cooling and liquid cooling for PEM fuel cells for MW-level aviation propulsion,* International Journal of Hydrogen Energy **47**, 29399 (2022).

[43] A. A. Kulikovsky, *The effect of stoichiometric ratio $\lambda$ on the performance of a polymer electrolyte fuel cell,* Electrochimica Acta **49**, 617 (2004).

[44] A. Fly and R. Thring, *Temperature regulation in an evaporatively cooled proton exchange membrane fuel cell stack,* International Journal of Hydrogen Energy **40**, 11976 (2015).

[45] G. Angelino, *Cicli Termodinamici Inversi: Frigoriferi ed a Pompa di Calore,* .

[46] R. W. Serth, *Process Heat Transfer*, 2nd ed. (Elsevier, 2014).

[47] S. G. Kandlikar, *A General Correlation for Saturated Two-Phase Flow Boiling Heat Transfer Inside Horizontal and Vertical Tubes,* Journal of Heat Transfer **112**, 219 (1990).

[48] S. G. Kandlikar and W. J. Grande, *Evolution of Microchannel Flow Passages–Thermohydraulic Performance and Fabrication Technology,* Heat Transfer Engineering **24**, 3 (2003).

[49] J. R. Thome, *Boiling in microchannels: a review of experiment and theory,* International Journal of Heat and Fluid Flow **25**, 128 (2004).

[50] J. R. Thome and A. Cioncolini, *Flow Boiling in Microchannels,* in *Advances in Heat Transfer*, Vol. 49 (Academic Press, 2017) pp. 157–224.

[51] T. Harirchian and S. V. Garimella, *Flow regime-based modeling of heat transfer and pressure drop in microchannel flow boiling,* International Journal of Heat and Mass Transfer **55**, 1246 (2012).

[52] N. Mao, J. Zhuang, T. He, and M. Song, *A critical review on measures to suppress flow boiling instabilities in microchannels,* 10.1007/s00231-020-03009-2/Published.

[53] R. K. Shah and D. P. Sekuli, *Fundamentals of Heat Exchanger Design* (John Wiley & Sons, Inc., Hoboken, NJ, USA, 2003).

[54] C. M. Invernizzi, *Closed power cycles: Thermodynamic fundamentals and applications,* Lecture Notes in Energy **11** (2013), 10.1007/978-1-4471-5140-1.

[55] G. Angelino and P. Colonna, *Multicomponent Working Fluids For Organic Rankine Cycles (ORCs),* Energy **23**, 449 (1998).

[56] A. Berto, M. Azzolin, S. Bortolin, C. Guzzardi, and D. Del Col, *Measurements and modelling of R455A and R452B flow boiling heat transfer inside channels,* International Journal of Refrigeration **120**, 271 (2020).

[57] H. Deng, M. Rossato, M. Fernandino, and D. Del Col, *A new simplified model for condensation heat transfer of zeotropic mixtures inside horizontal tubes,* Applied Thermal Engineering **153**, 779 (2019).

[58] C. E. Brennen, *Hydrodynamics of Pumps* (Cambridge University Press, 2011).

[59] A. Mannini, *SAINT-PETERSBURG, RUSSIA The Environmental Control System for a Modem Helicopter: a Blend of New Technologies*, Tech. Rep.

[60] J. Schiffmann and D. Favrat, *Experimental investigation of a direct driven radial compressor for domestic heat pumps,* International Journal of Refrigeration **32**, 1918 (2009).

[61] J. Schiffmann and D. Favrat, *Design, experimental investigation and multi-objective optimization of a small-scale radial compressor for heat pump applications,* Energy **35**, 436 (2010).

[62] A. Giuffre, F. Ascione, C. De Servi, and M. Pini, *Data-driven modeling of high-speed centrifugal compressors for aircraft environmental control system,* (2022).

[63] J. Dong, Y. Lin, S. Deng, C. Shen, and Z. Zhang, *Experimental investigation of an integrated cooling system driven by both liquid refrigerant pump and vapor compressor,* Energy and Buildings **154**, 560 (2017).

[64] A. S. Merino, J. Hugon, Y. Cailloce, F. Michard, T. Tjiptahardja, A. Larue de Tournemine, and C. Laporte, *Development of a two-phase mechanically pumped loop (2ϕMPDL) for the thermal dissipation management of an active antenna,* in *40th International Conference on Environmental Systems, ICES 2010* (2010).

[65] G. Angelino and C. Invernizzi, *General method for the thermodynamic evaluation of heat pump working fluids,* International Journal of Refrigeration **11**, 16 (1988).

[66] A. Giuffre, P. Colonna, and M. Pini, *Design optimization of a high-speed twin-stage compressor for next-gen aircraft environmental control system,* (2022).

[67] F. Ascione, C. De Servi, O. Meijer, V. Pommé, and P. Colonna, *Assessment of an inverse organic rankine cycle system for the ecs of a large rotorcraft adopting a high-speed centrifugal compressor and a low gwp refrigerant,* in *Proceedings of the 6th International Seminar on ORC Power Systems* (Technical University of Munich, 2021).

[68] E. W. Lemmon, I. H. Bell, M. L. Huber, and M. O. McLinden, *NIST Standard Reference Database 23: Reference Fluid Thermodynamic and Transport Properties-REFPROP, Version 10.0, National Institute of Standards and Technology,* (2018).

[69] I. H. Bell, J. Wronski, S. Quoilin, and V. Lemort, *Pure and pseudo-pure fluid thermophysical property evaluation and the open-source thermophysical property library coolprop,* Industrial & Engineering Chemistry Research **53**, 2498 (2014), http://pubs.acs.org/doi/pdf/10.1021/ie4033999 .

[70] H. J. van Gerner, R. C. Van Benthem, J. Van Es, D. Schwaller, and S. Lapensee, *Fluid selection for space thermal control systems,* 44th International Conference on Environmental Systems (2014).

[71] S. G. Kandlikar and P. Balasubramanian, *An Extension of the Flow Boiling Correlation to Transition, Laminar, and Deep Laminar Flows in Minichannels and Microchannels,* Heat Transfer Engineering **25**, 86 (2004).

[72] S. G. Kandlikar, *Flow boiling in minichannels and microchannels,* in *Heat Transfer and Fluid Flow in Minichannels and Microchannels* (Elsevier, 2006) pp. 175–226.

[73] E. Afshari, M. Ziaei-Rad, and Z. Shariati, *A study on using metal foam as coolant fluid distributor in the polymer electrolyte membrane fuel cell,* International Journal of Hydrogen Energy **41**, 1902 (2016).

[74] M. H. Bargal, M. A. Abdelkareem, Q. Tao, J. Li, J. Shi, and Y. Wang, *Liquid cooling techniques in proton exchange membrane fuel cell stacks: A detailed survey,* Alexandria Engineering Journal **59**, 635 (2020).

[75] B. Petukhov, *Heat Transfer and Friction in Turbulent Pipe Flow with Variable Physical Properties,* in *Advances in Heat Transfer*, Vol. 6 (Elsevier, 1970) pp. 503–564.

[76] V. Gnielinski, *New equations for heat and mass transfer in turbulent pipe and channel flow,* Int. Chem. Eng. **16**, 359 (1976).

[77] R. Shah and A. London, *Rectangular Ducts,* in *Laminar Flow Forced Convection in Ducts* (Elsevier, 1978) pp. 196–222.

[78] E. Afshari, M. Ziaei-Rad, and M. M. Dehkordi, *Numerical investigation on a novel zigzag-shaped flow channel design for cooling plates of PEM fuel cells,* Journal of the Energy Institute **90**, 752 (2017).

[79] S. Mahabunphachai, O. N. Cora, and M. Koc, *Effect of manufacturing processes on formability and surface topography of proton exchange membrane fuel cell metallic bipolar plates,* Journal of Power Sources **195**, 5269 (2010).

[80] S. M. Kim and I. Mudawar, *Universal approach to predicting saturated flow boiling heat transfer in mini/micro-channels – Part I. Dryout incipience quality,* International Journal of Heat and Mass Transfer **64**, 1226 (2013).

[81] M. M. Mahmoud and T. G. Karayiannis, *Heat transfer correlation for flow boiling in small to micro tubes,* International Journal of Heat and Mass Transfer **66**, 553 (2013).

[82] J. B. Copetti, M. H. Macagnan, F. Zinani, and N. L. Kunsler, *Flow boiling heat transfer and pressure drop of R-134a in a mini tube: an experimental investigation,* Experimental Thermal and Fluid Science **35**, 636 (2011).

[83] B. Raja, D. Mohan Lal, and R. Saravanan, *Flow boiling heat transfer coefficient of R-134a/R-290/R-600a mixture in smooth horizontal tubes using varied heat flux method,* Applied Thermal Engineering **29**, 1778 (2009).

[84] Y. Y. Hsu, *On the Size Range of Active Nucleation Cavities on a Heating Surface,* Journal of Heat Transfer **84**, 207 (1962).

[85] S. G. Kandlikar, *Heat Transfer Characteristics in Partial Boiling, Fully Developed Boiling, and Significant Void Flow Regions of Subcooled Flow Boiling,* Journal of Heat Transfer **120**, 395 (1998).

[86] L. Friedel, *Improved friction pressure drop correlation for horizontal and vertical two-phase pipe flow,* (1979).

[87] R. W. Serth and T. G. Lestina, *Boiling Heat Transfer,* in *Process Heat Transfer* (Elsevier, 2014) pp. 317–360.

[88] H. N. Hoang, N. Agustiarini, and J. T. Oh, *Experimental Investigation of Two-Phase Flow Boiling Heat Transfer Coefficient and Pressure Drop of R448A inside Multiport Mini-Channel Tube,* Energies **15**, 4331 (2022).

[89] Y. Zong, B. Zhou, and A. Sobiesiak, *Water and thermal management in a single PEM fuel cell with non-uniform stack temperature,* Journal of Power Sources **161**, 143 (2006).

[90] F. P. Incropera and D. P. DeWitt, *Fundamentals of Heat and Mass Transfer*, 4th ed. (John Wiley and Sons, Inc., New York City, New York, 1996).

[91] N. A. Qasem and S. M. Zubair, *Compact and microchannel heat exchangers: A comprehensive review of air-side friction factor and heat transfer correlations,* Energy Conversion and Management **173**, 555 (2018).

[92] R. M. Manglik and A. E. Bergles, *Heat transfer and pressure drop correlations for the rectangular offset strip fin compact heat exchanger,* Experimental Thermal and Fluid Science **10**, 171 (1995).

[93] M. M. Shah, *A general correlation for heat transfer during film condensation inside pipes,* International Journal of Heat and Mass Transfer **22**, 547 (1979).

[94] R. Gilbey, *Drag and pressure recovery characteristics of auxiliary air inlets at subsonic speeds,* Tech. Rep. (Engineering Sciences Data Unit, London, 1986).

[95] G. Sovran and E. Klomp, *Experimentally determined optimum geometries for rectlinear diffusers with rectangular, conical or annular cross section,* Fluid Mechanics of Internal Flow (1967).

[96] L. R. Reneau, J. P. Johnston, and S. J. Kline, *Performance and Design of Straight, Two-Dimensional Diffusers,* Journal of Basic Engineering **89**, 141 (1967).

[97] *VDI Heat Atlas* (Springer Berlin Heidelberg, Berlin, Heidelberg, 2010).

[98] *PW100-150 - Pratt & Whitney,* .

[99] M. R. Nichols, *Investigation of flow through an intercooler set at various angles to the supply duct,* United States and Langley Aeronautical Laboratory (1942), http://pubs.acs.org/doi/pdf/10.1021/ie4033999 .

[100] L. Henriksson, E. Dahl, P. Gullberg, and L. Löfdah, *Experimental Investigation of Heat Transfer Rates and Pressure Drops through Compact Heat Exchangers - Where the Heat Exchanger is Angled Relative to the Incoming Airflow,* International Journal of Automotive Engineering **6**, 7 (2015).

[101] M. Hepperle, *Javaprop - design and analysis of propellers,* MH AeroTools.

[102] P. M. Sforza, *Propellers,* in *Theory of Aerospace Propulsion* (Elsevier, 2017) pp. 487–524.

[103] R. Babikian, S. P. Lukachko, and I. A. Waitz, *The historical fuel efficiency characteristics of regional aircraft from technological, operational, and cost perspectives,* Journal of Air Transport Management **8**, 389 (2002).

[104] S. E. Mattsson and H. Elmqvist, *Modelica - An International Effort to Design the Next Generation Modeling Language,* IFAC Proceedings Volumes **30**, 151 (1997).

[105] L. R. Petzold, *Description of dassl: a differential/algebraic system solver,* (1982).

[106] B. An, Y. Duan, L. Tan, and Z. Yang, *Vapor Pressure of HFE 7100,* Journal of Chemical and Engineering Data **60**, 1206 (2015).

[107] M. H. Rausch, L. Kretschmer, S. Will, A. Leipertz, and A. P. Fröba, *Density, surface tension, and kinematic viscosity of hydrofluoroethers HFE-7000, HFE-7100, HFE-7200, HFE-7300, and HFE-7500,* Journal of Chemical and Engineering Data **60**, 3759 (2015).

[108] J. H. Hao, Q. Chen, J. X. Ren, M. Q. Zhang, and J. Ai, *An experimental study on the offset-strip fin geometry optimization of a plate-fin heat exchanger based on the heat current model,* Applied Thermal Engineering **154**, 111 (2019).

[109] Y. J. Chang and C. C. Wang, *A generalized heat transfer correlation for louver fin geometry,* International Journal of Heat and Mass Transfer **40**, 533 (1997).

[110] M. H. Kim and C. W. Bullard, *Air-side thermal hydraulic performance of multi-louvered fin aluminum heat exchangers,* International Journal of Refrigeration **25**, 390 (2002).

[111] H. Lisa, D. Erik, G. Peter, and L. Lennart, *Experimental Investigation of Heat Transfer Rates and Pressure Drops through Compact Heat Exchangers,* International Journal of Automotive Engineering **6**, 20154053 (2015).

[112] *BOMBARDIER DASH 8 300/Q400,* .